Rochester Institute of Technology

RIT Digital Institutional Repository

Theses

4-1-2020

Nonlinear Optics in Photonic Ultrawide-Bandgap Circuits

Michael Larry Fanto
mlf9729@rit.edu

Follow this and additional works at: https://repository.rit.edu/theses

Recommended Citation
Fanto, Michael Larry, "Nonlinear Optics in Photonic Ultrawide-Bandgap Circuits" (2020). Thesis. Rochester Institute of Technology. Accessed from

This Dissertation is brought to you for free and open access by the RIT Libraries. For more information, please contact repository@rit.edu.

NONLINEAR OPTICS IN PHOTONIC ULTRAWIDE-BANDGAP CIRCUITS

A dissertation submitted in partial fulfillment of the

requirements for the degree of Doctor of Philosophy

in Microsystems Engineering

by

Michael Larry Fanto

KATE GLEASON SCHOOL OF ENGINEERING

Rochester Institute of Technology

Rochester, New York

April 01, 2020

MICROSYSTEMS ENGINEERING
KATE GLEASON SCHOOL OF ENGINEERING
ROCHESTER INSTITUTE OF TECHNOLOGY
ROCHESTER, NEW YORK

Ph.D. DISSERTATION DEFENSE

Candidate: Michael Larry Fanto . . . .

Dissertation Title: Nonlinear Optics in Photonic Ultrawide-bandgap Circuits . . . .

Adviser: Dr. Stefan F. Preble . . . .

Date of defense: April 01, 2020 . . . .

The candidate's Ph.D. Dissertation has been reviewed by the undersigned. The Dissertation

(a) is acceptable, as presented.

(b) is acceptable, subject to minor amendments.

(c) is not acceptable in its current form.

Written details of required amendments or improvements have been provided to the candidate.

Committee:

Dr. Mishkatul Bhattacharya, Committee Member

Dr. Edwin Hach, Committee Member

Dr. Parsian Mohseni, Committee Member

Dr. Paul M. Alsing, Committee Member

Dr. Thomas W. Smith, Committee Member

Dr. Stefan F. Preble, Thesis Advisor

Please submit form to MCSE Graduate Program Coordinator

MICROSYSTEMS ENGINEERING
KATE GLEASON SCHOOL OF ENGINEERING
ROCHESTER INSTITUTE OF TECHNOLOGY
ROCHESTER, NEW YORK

CERTIFICATE OF APPROVAL

Ph.D. DEGREE DISSERTATION

The Ph.D. Degree Dissertation of *Michael Larry Fanto* has been examined and approved by the dissertation committee as satisfactory for the dissertation requirement for the Ph.D. degree in Microsystems Engineering.

____
Dr. Mishkatul Bhattacharya, Committee Member

____
Dr. Edwin Hach, Committee Member

____
Dr. Parsian Mohseni, Committee Member

____
Dr. Paul M. Alsing, Committee Member

____
Dr. Thomas W. Smith, Committee Member

____
Dr. Stefan F. Preble, Thesis Advisor

Date ______________________________

NONLINEAR OPTICS IN PHOTONIC ULTRAWIDE-BANDGAP CIRCUITS

By

Michael Larry Fanto

A dissertation submitted in partial fulfillment of the requirements for the degree of Ph.D. in Microsystems Engineering, in the Kate Gleason School of Engineering, Rochester Institute of Technology.

April 01, 2020

Approved by

____________________________________ ____________

Dr. Bruce Smith Date

Director, Microsystems Engineering

Dedication

I would like to dedicate this thesis to my parents, Larry and Maria, for all the support and encouragement throughout my life. Without your support I would not be the person that I am today, I love you both.

As with most things in life, research is no different. It is not accomplished in a vacuum solely by an individual but by a team of people striving to answer those fundamental questions that keep us awake at night. The support from the entire team is invaluable and I cannot thank them enough for all the support over the years. That team for me has consisted of many different individuals, and whether mentioned or not please know that I am truly thankful for your help and support.

I would like to thank my advisor and friend, Professor Stefan Preble. Thank you for your support and friendship over the years, I truly appreciate everything you have done. Thank you in advance for a life long friendship, great research to come, many trips around the world, and a plethora of amusement parks.

I would like to thank my sister, Alana, for your love and support, and also being a sounding board for presentations and explanations. I love you.

I have always lived by the phrase,"Family does not end with blood," and have been very lucky in my life to have two other families that are my family. I want to thank the Muttillo and the Tison families for your support over the years. I can not even express how much it has meant to me, love all of you.

Acknowledgements

I want to thank my parents, Larry and Maria, and my sister Alana, for all the support and encouragement you have given over the years.

Thank you very much to all of family and friends for your support, you are all a big part of my life and I enjoy the time I get to spend with you.

Thank you to the RIT Integrated photonics team and the RIT Microsystems Engineering program. I have built so many great memories, friendships, and interactions over the years that I would not trade for anything.

Thank you to my advisor and friend, Professor Stefan Preble, for all you have done over the years. Words cannot express my appreciation.

Thank you to all my committee members for all your help and keeping me on track throughout my time at RIT.

Thank you very much to Lisa Zimmerman. I really appreciate all your help over the years, and for keeping us all on track.

I want to thank my fellow researchers at the Air Force Research Laboratory for their support over the years while I was at RIT and while I am back in Rome finishing up. I could not have done this without your help and I am eternally thankful.

Abstract

Ultrawide-bandgap semiconductors have an important role for many applications ranging from power electronics to photonics. The semiconductor material with the largest bandgap is aluminum nitride with a maximum bandgap of 6.28 eV, corresponding to a wavelength transparency extending to 197 nm. The large transparency window makes aluminum nitride a promising optical material for applications that span from the infrared to ultraviolet. Along with these properties, aluminum nitride is a non-centrosymmetric crystal allowing exploitation of the second order nonlinearity and the electro-optic effect. This thesis will cover the synthesis of the material, a number of characterization techniques that verify the quality of the material, and conclude with applications for the synthesized material.

To date we have demonstrated an ultrawide-bandgap semiconductor photonics platform based on nanocrystalline aluminum nitride (AlN) on sapphire. This photonics platform guides light at low loss from the ultraviolet (UV) to the visible spectrum, though is transparent from 200 -15,000 nm. We measured ring resonators with intrinsic quality factor (Q) exceeding 170,000 at 638 nm and Q >20,000 down to 369.5 nm, which shows a promising path for low-loss integrated photonics in UV and visible spectrum. The nonlinear, electro-optic, and piezo-electric properties of AlN make it a promising active material for controlling and connecting atomic and atom-like quantum memories, coherent qubit transduction, entangled photon generation, and frequency conversion.

Contents

Dedication **i**

Acknowledgements **ii**

Abstract **iii**

Contents **iv**

List of Figures **vii**

List of Tables **xv**

1 Introduction **1**

1.1 Introduction 1

1.2 Nonlinear Optics 4

1.3 Integrated Photonics 8

1.4 Materials 8

2 Prior State of the Art **13**

2.1 Characterization of Aluminum Nitride Films 13

2.1.1 Atomic Force Microscopy 18

2.1.2 Transmission electron microscopy & HR-TEM 20

2.1.3 X-Ray Photoelectron Spectroscopy 23

2.1.4 Scanning Electron Microscopy & Helium Ion Microscopy 26

2.2 State of the Art Devices 29

3 Characterization and Waveguide Fabrication **33**

3.1 Aluminum Nitride Film Characterization 33

3.2 Fabrication 35

4 Ion Milling **39**

4.1 Optical Interfaces 39

4.2 Design And Fabrication 41

4.3 Experimental Setup and Results 44

5 Experiments **49**

5.1 Experimental Testbed 49

5.1.1 Coupling Methods to the Photonic Circuits 52

5.1.2 Ring Resonators 54

6 Foundry Level Fabrication **63**

6.1 Transitioning from University to Foundry 63

6.2 Wide-bandgap Materials in a Foundry 64

6.3 Ultrawide-bandgap Materials in a Foundry 66

7 Broadband Photon Source **71**

7.1 Broadband Photon Source 71

7.1.1 Experimental Configuration 72

8 Discussion **77**

8.1 Discussion 77

8.1.1 Conclusions 77

8.1.2 Future Research 80

References **100**

List of Figures

1.1 The chart shows a subsection of the available quantum technologies with the corresponding wavelengths of interest. Whether these are used as single photon sources or quantum memories the interaction wavelengths are noteworthy when the various quantum technologies must coherently pass quantum information across the platform. 3

1.2 The cartoon illustrates a universal platform serving as a node in a quantum network containing the necessary components of memory, qubit sources, processing circuitry, and coherent state transduction. 4

1.3 Energy diagrams representing the pump and signal/idler structure for energy degeneracy in spontaneous parametric downconversion. 6

1.4 Energy diagrams representing the pump and signal/idler structure for energy degeneracy in spontaneous four wave mixing. 7

1.5 The chart shows a subsection of the available quantum technologies with the corresponding wavelengths of interest. Whether these are used as single photon sources or quantum memories the interaction wavelengths are noteworthy when the various quantum technologies must coherently pass quantum information across the platform. 9

2.1 Absorption coefficient vs photon energy plotted for two different substrates (a) normal, and (b) grown in an oxygen deficient atmosphere [48]. 14

2.2 Deconvolution of the absorption spectrum into the Gaussian contributions. The relate to the following sections of the wafer (a) colorless, (b) yellow, (c) brown, and (d) transparent region of the oxygen deficient atmosphere wafer [48]. 15

2.3 Visualization showing the different defect states in AlN, (a) aluminum vacancy and nitrogen vacancies, (b) aluminum vacancy and nitrogen vacancy complex, (c) aluminum vacancy and oxygen substitutional complex, and (d) aluminum vacancy and oxygen substitutional complex [49]. 16

2.4 Unit cell of AlN showcasing the c and m planes of the individual crystal [12]. . 17

2.5 Growth chamber for AlN bulk substrates through sublimation of AlN raw material which is heated and then condenses on a seed crystal located at the top of the chamber [53]. 17

2.6 AFM map of a 40 nm AlN thin film. The average variation across the film was approximately 250 pm [44]. 18

2.7 AFM map of the 100 nm AlN thin films grown by magnetron sputtering at various temperatures (a) 300 C, (b) 400 C, (c) 500 C, and (d) 600 C [59]. . . . 19

2.8 AFM map of the 100 nm AlN thin films grown by magnetron sputtering at various nitrogen concentrations(a) 60%, and (b) 30% [59]. 20

2.9 (a) Fabrication step of the waveguide, (b) TEM image of the optical waveguide showing the vertically oriented grains, EDX maps of (c) silicon, (d) aluminum, (e) oxygen, and (f) nitrogen [60]. 21

2.10 HR-TEM image of the interface between wurtzite AlN and silicon carbide. The lattice planes can be seen as well as the transition between the two materials [61]. 22

2.11 HR-TEM image of the inversion domain boundaries caused by oxygen defects forming during the growth of the AlN lattice [52]. 23

2.12 Rotated HR-TEM image which shows the corrugated nature of the inversion domain boundaries in the AlN film [52]. 24

2.13 Illustration of the characteristic related peaks and respective binding energies found in AlN films characterized by XPS [44, 62] 24

2.14 XPS collected plots (a) before etching, and (b) after 20 minutes of etching has occurred [63]. 25

2.15 SEM images of the grating coupler constructed in a 140 nm thick AlN film showing the (a) individual rib of the grating coupler, (b) array of ribs, and (c) entire grating coupler [64]. 27

2.16 SEM of a multi-mode optical waveguide clearly illustrating the residual detritus left in contact from the fabrication process [40]. 28

2.17 HIM image of a 200 nm thick AlN waveguide highlighting the low sidewall roughness [66]. 29

2.18 (a) 330 nm thick AlN waveguide structure with resonator enhancement cavity, (b) SEM of the optical waveguide/ring resonator coupling region, (c) resonance spectrum of the resonator, (d) resonator displaying 775 nm SHG light from a 1550 nm input, (e) log plot of the SHG conversion efficiency [68]. 30

2.19 Figure showing optical frequency comb generation in the ultraviolet from a tapered crystalline aluminum nitride waveguide.[69] 31

3.1 Properties of AlN-on-sapphire material. (a) Cross section illustrating each layer of the wafer, along with their respective thickness; top inset: atomic force microscopy scan of AlN film showing the nanocolumn size. Surface roughness is measured to be 0.9 nm RMS with 26.5 nm grain size (b) High resolution x-ray diffraction (002) and (015) ω scan of AlN. (c) (015) ϕ scan of AlN showing six-fold symmetry wurtzite structure. (d) Refractive index measurements using ellipsometry. (e) Background fluorescence from sapphire substrate (yellow), unpatterned AlN (blue), patterned AlN (orange), and stoichiometric silicon nitride (purple). (f) Background fluorescence from SiON top cladding, before (blue circles) and after (orange squares) bleaching. 35

3.2 (a) AlN on sapphire photonics fabrication process: (i) Start off with an unpatterned AlN-on-sapphire chip diced up from a whole wafer. (ii) Spin coat HSQ (2% XR-1541), pattern using electron beam lithography, and develop using an aqueous mixture of 1 wt % NaOH and 4 wt % NaCl for high contrast. (iii) Etch by ICP-RIE using chlorine chemistry. (iv) Strip HSQ. (v) Clad with silicon oxynitride using plasma-enhanced chemical vapor deposition (PECVD). (vi) Edge polish for making the inverse-tapered edge couplers. (b) Scanning electron microscope (SEM) image of a fabricated AlN waveguide (c) Transversal component of TE mode in AlN waveguide for PMMA and SiON cladding for 638 nm (top) and 400 nm (bottom) wavelengths. 36

4.1 AlN nitride optical microscope top view image of a worst case scenario where the cladding chipped during polishing but did not damage the waveguide. Consequently, the top cladding was removed and redeposited. During the second attempt at deposition, crystal regrowth of sapphire substrate appeared, and then the sample became unsalvageable. 40

4.2 Simulated ideal mode profile of the SM300 fiber (top left, bottom left), the untapered edge coupler (top right), and the tapered edge coupler (bottom right). Colormap represents intensity of electric field on log scale (dB). 43

4.3 Layout of the variety of waveguide structures and dimensions, drawn in Klayout, on chip with tapers aligned to edges for traditional edge polishing for direct fiber coupling. 44

4.4 (a) 2000X optical micrograph of chipped facet from traditional polishing. Notably the cladding and waveguide often delaminate together witch disallows direct and free space coupling. (b) 2000x micrograph of the same optical chip with an ion milled facet suitable for fiber or freespace coupling. 44

4.5 200X optical micrograph of ion milled facet. (Inset) Waveguides array along top edge. 45

4.6 (Top)Testbed, showing the vacuum chuck and fibers directly coupled to the AlN chip. The chip appears blue from the incident 369 nm light into the waveguide.(Bottom) Fiber edge coupled AlN microring on resonance. 46

4.7 Transmission plot from direct fiber-coupling to the AlN PIC after ion milling showing transmission of a scanning laser through the waveguide and ring resonator with the resonances apparent from 391 to 394 nm. 47

5.1 ((Left) Experimental for testing the AlN chips in the infrared. The laser beam enters from the right and is sent through beam shaping, polarization rotation, and attenuating optics before an aspheric objective lens and coupling into/out of the chip. (Top right) Wavelength tuned to off resonance for the microring. (Bottom right) Wavelength tuned to resonance of the microring, note the illumination of the microring and the drop in power on the exit waveguide . . . 50

5.2 Representative plot of the microresonator resonances detected on a power meter as the spectrum from a pulsed Ti:Sapphire laser is tuned from the visible to the infrared. 51

5.3 ((Top) Experimental for testing the AlN chips in the ultraviolet. The laser beam enters from the right and is sent through beam shaping, polarization rotation, and attenuating optics before entering an optical fiber. (Lower right) The optical fiber (Nufern SM300) is the routed to the chip and butt coupled with the flat cleaved fiber end. (Lower left) Fiber edge coupling to the waveguides at 369.5 nm using Nufern SM300 fiber. 52

5.4 (a) SEM images of the grating couplers. First gap of the grating coupler is 60 nm, and the gaps are linearly increasing. Curvatures are set to be matched with mode evolution so that there is no reflection. Top: green spectrum grating coupler. Bottom: red spectrum grating coupler (b) Coupling efficiency vs. wavelength plot of green-spectrum grating coupler optimized for 500 to 600 nm. Black line: measured data. Green line: simulation. (c) Coupling efficiency vs. wavelength plot of red-spectrum grating coupler optimized for 600 to 700 nm. Black line: measured data. Red line: simulation. (d) Fiber edge coupling to the waveguides at 369.5 nm using Nufern SM300 fiber. (e), (f) Single mode operation at 468 and 369.5 nm, respectively. 53

5.5 Transmission spectrum of the 369 nm resonance showing 3 peaks to confirm the microresonator FSR of 350 pm. 56

5.6 (a) SEM of the ring resonator. Inset shows a close up of the ring resonator. The gap between the waveguide and the ring is 300 nm for the undercoupling regime, which was used to verify the unloaded Q. (b) Frequency response at 369.5 nm of the ring resonator around resonance. The Lorentzian fitting shows a Q of $>$24,000. (c) Quality factors of 40 μm radius ring resonators measured using an optical spectrum analyzer (OSA) for wavelengths spanning from 380 nm to 480 nm, along with the quality factors at 369.5 nm wavelength using both frequency doubled pulsed and continuous-wave (CW) TI:Sapphire lasers. (d) Wavelength response of the ring resonator around resonance. The Lorentzian fitting shows a Q of $>$140,000. Inset shows a zoom-in of the wavelength response. 57

5.7 Characterization of the microresonators in the visible to infrared. (Top left) Free spectral range, (Top right) Quality factor, (Bottom left) Group index, and (Bottom right) Pink region is the range of index matched group indices that will result in photon generation. 58

5.8 Characterization of the microresonators in the ultraviolet to the visible. (Top left) Free spectral range, (Top right) Quality factor, (Bottom left) Group index, and (Bottom right) Pink region is the range of index matched group indices that will result in photon generation. 60

5.9 Q and Group index plots with the added data at 369 nm. The trend for the device held true down to 369 nm. 60

5.10 ((Left) Image showing the waveguide producing violet light from and input infrared pump laser. (Middle) Far field image of the output mode, showing the center mode which contains the fundamental and the SHG, and the higher order SHG modes that exist in the waveguide. (Right) Spectral plot of the fundamental pulsed pump (Coherent Mira) with the measured SHG output superimposed (Horriba spectrometer). 62

6.1 (a) and (b) Photons sources fabricated at CNF. (c) and (d) Photon sources fabricated at a small company. (e-g) Photon sources fabricated at the AIM Photonics foundry. 65

6.2 Photograph of the 300 mm quantum photonics wafer. (left inset) Designed reticle comprising of 12 chips, and 44 subcells. (righ inset) Photograph of one of the 65 fabricated reticles on the 300 mm wafer. 66

6.3 Designed AlN structures to be fabricated through both the typical and damascene fabrication methods at CNSE. 67

6.4 (Top) SEM image of atomic layer deposited (ALD) AlN on SiO_2 and then reactive ion etched to create the waveguides. (Bottom left) Damascene created optical waveguides. (Bottom right) Damascene optical waveguide with an etch stop of SiN to aid in trench fabrication. 68

7.1 (Top) Layout schematic of the entire source from laser to detectors. (Bottom) Photograph of the source with a full component description in the text. 73

7.2 (Clockwise from upper left) OSA spectral plot from a single PPKTP show that tuning the crystals oven temperature by 2° Celsius allows the spectral output to go from spectral non-degeneracy to spectral degeneracy. 75

List of Tables

3.1 SiON Process Conditions in Oxford 100 PECVD System 37

4.1 By varying widths, diameters, and gaps for the AlN microring resonators the authors should be able to extract n_{eff}, loss, and other values for this material. 42

7.1 Here, ϕ is approximately 0.335 and $\Delta n_g = |n_{g1} - n_{g2}|$. 72

Chapter 1

Introduction

1.1 Introduction

Photons are the ideal choice as the long distant carrier of quantum information due to their room temperature operation, resistance to decoherence, and the ability to travel only on the energy required for their generation. These same properties combined with the speed of light travel make photons ideally suited for fast processing of quantum information [1, 2], connections for quantum networks [1, 3–5], transmission to space [6] , and ultra-secure communications [7]. There are many different methods of photon generation ranging from atomic emissions [1], defect sites in lattices [8, 9], quantum dots [10], and nonlinear generation [11] each of which have their own strengths and weaknesses. Atomic, and defect sites in lattice systems produce truly single photons with extremely long coherence lengths but the emission angle encompasses an entire sphere making collection efficiency low. Quantum dots produce truly single photons, can be growth into optical waveguide structures, but are extremely hard to make spectrally identical reducing the scalability. For these reasons nonlinear optics provides some of the most prevalently used processes to create these photons, typically through the two main processes of spontaneous parametric downconversion (SPDC) and spontaneous four-wave mixing (SFWM). From either of these processes a pair of bi-photons (correlated) photons are created which obey momentum and energy conservation with respect to the excitation laser and the generating material. The photons are always produced in pairs allowing one of the

pair to be detected, heralding the arrival of a single photon. Though these photons are not on-demand they are a very reliable bright source of photon pairs. Any of the processes described above can be used for quantum information science applications to include sensing, communication, networking, and computation.

Compared with the traditional digital computing architectures prevalent today quantum architectures and processors rely on interference between the quantum bits (qubits). Where a qubit is any two level system that showcases the properties of superposition and entanglement. Superposition is the ability of a system to exist in multiple states at once, and entanglement is where two or more systems show perfect correlations (non-separable). Each of these properties make the qubit powerful but fragile. Therefore, phase and amplitude stability of the entire system is critical which quickly makes the scaling of bulk optics-based systems intractable. Though there have been many hero experiments performed in bulk optics to push the boundaries of just what can be demonstrated. These experiments include large single photon level entangled state generation, large photon number continuous variable systems, and and numerous solid state qubit experiments. Integrated photonics fills this requirement perfectly, allowing devices to be fabricated with 10's of nanometers of precision, repeatable between fabrication runs, and designed for packaging to remove environmental fluctuations from impacting the quantum state.

The final decision is the material choice in which to fabricate the photonic integrated circuits. There are general factors that are applicable for integrated photonics and even more critical for quantum applications. First and foremost the intended material must have low propagation loss so the photons make it through the device. Secondly the material needs some form of tunability, such as thermo-optic or electro-optic effects. Lastly, the material needs to be thermally and physically stable to hold the intended form after fabrication.

Which quantum technologies and wavelength regimes exist at present that the photonic materials need transparency over. Scanning the literature there are a number of technologies that stand out as candidates which could benefit from integrated photonics. A selected few from the literature are highlighted in Fig. 1.1. The highlighted technologies consist of the

three leading qubit technologies to date, trapped ions, photons, and superconducting circuits. These technologies require wavelength transparency in the ultraviolet/visible, visible/near infrared/infrared, and microwave respectively. Combining all these qubit technologies into a single platform will require a material transparent over many octaves.

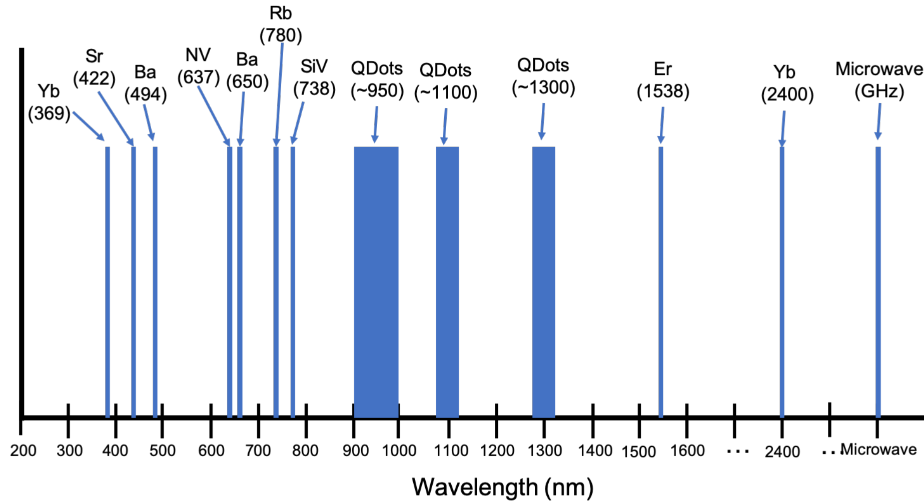

Figure 1.1: The chart shows a subsection of the available quantum technologies with the corresponding wavelengths of interest. Whether these are used as single photon sources or quantum memories the interaction wavelengths are noteworthy when the various quantum technologies must coherently pass quantum information across the platform.

Analyzing the situation from one higher level of abstraction, there are many factors that come into this decision on the intended device level. From a networking perspective, silicon is the obvious choice due to the transparency in the infrared (>1100 nm), and the telecommunications backbone was constructed for the infrared (1250-1650 nm). For free space communications one wants to transmit in the visible and near infrared (600-850 nm) since the apertures are smaller due to the shorter wavelength. Lastly for processing and computation quantum memory needs to be considered which occurs in the ultraviolet, visible, and microwave. With a vast array of wavelength regimes to consider the final system is heterogenous with components optimized for their respective tasks. Ideally an ultrawide-bandgap material would be chosen allowing for the fabrication of a monolithic platform allowing the future combination of these quantum technologies as in the cartoon in Fig. 1.2. Research into this platform and the generation of the photon-based qubits is the subject of this document.

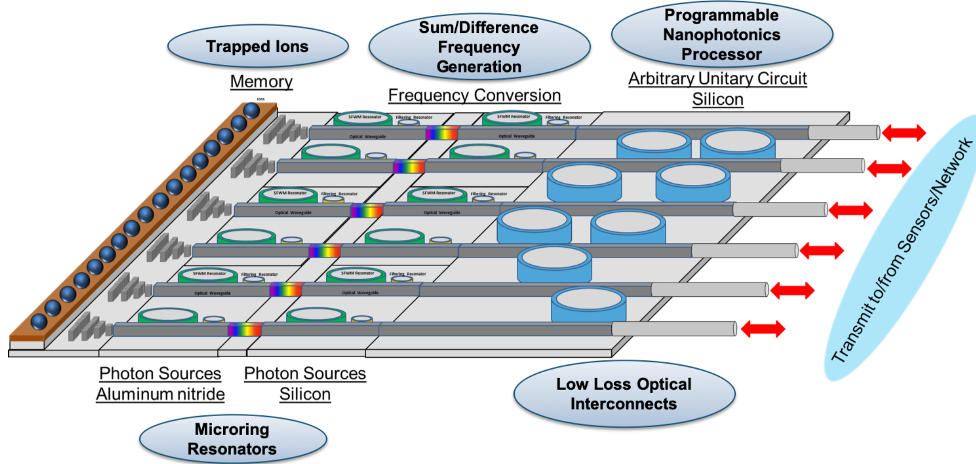

Figure 1.2: The cartoon illustrates a universal platform serving as a node in a quantum network containing the necessary components of memory, qubit sources, processing circuitry, and coherent state transduction.

In the rest of the section is a brief overview of nonlinear optics, integrated photonics, and material selection will be described. This will be followed by prior and current state of the art research in the area, our contributions to this research, conclusions, and concluded with future research.

1.2 Nonlinear Optics

In our day-to-day interactions with the world the photon flux, or intensity, is low enough that what we are use to is classified as linear optics. This means that as with any material, an incident time varying electric field will cause a change in the material which will cause a change in the electric field. This is apparent when looking at the final form of the wave equation (shown below) where the left side describes the change in the electric field and the right side describes the material response.

$$\nabla^2 \vec{E} - \mu_0 \varepsilon_0 \frac{\partial^2 \vec{E}}{\partial t^2} = \mu_0 \frac{\partial^2 \vec{P}}{\partial t^2} \tag{1.2.1}$$

The left side describes the polarization of the material, specifically how the material reacts to an applied electric field. In the low field flux regime, the material exhibits a linear

dependence with the applied field.

$$\vec{P}(t) = \varepsilon_0 \chi^{(1)} \vec{E}(t) \tag{1.2.2}$$

Where $\chi^{(1)}$ is the linear susceptibility of the material. As the applied field strength increases, this relationship does not hold true and the polarizability must be expressed in a more general form as a power series.

$$\vec{P}(t) = \varepsilon_0[\chi^{(1)} \vec{E}(t) + \chi^{(2)} \vec{E}^2(t) + \chi^{(3)} \vec{E}^3(t) + \chi^{(4)} \vec{E}^4(t) + ...] \tag{1.2.3}$$

This regime of high field strength is easily achieved with the output light from a laser. This is when the higher order susceptibilities, such as the second $\chi^{(2)}$ and $\chi^{(3)}$ third order effects become significant. When using these susceptibilities this description assumes that the tensors are diagonal, and that the tensor corresponds to a specific crystal plane [12, 13].

In practice this material response is extremely useful and allows for the modification of an applied input field into a desired output field. This commonly witnessed to produce wavelengths of light that are not available directly from a laser. An example of this is green laser pointers which contain a nonlinear material which converts infrared light into green light. This process is called second harmonic generation (SHG) and is enabled by the $\chi^{(2)}$ present in non-centrosymetric materials. The process is the effect of three interacting waves, sometimes referred to as three-wave mixing, where two photons of a lower energy combine to a single photon of higher energy, while always obeying energy and momentum conservation of the system. In this specific case the two lower energy photons are spectrally degenerate but that is not a fundamental constraint, as the general process where the photons are spectrally non-degenerate is called sum frequency generation.

$$\vec{P}(t) = \varepsilon_0[\chi^{(1)} \vec{E}(t) + \chi^{(2)} \vec{E}^2(t) + \chi^{(3)} \vec{E}^3(t) + \chi^{(4)} \vec{E}^4(t) + ...] \tag{1.2.4}$$

Input the field:

$$\vec{E}(t) = \vec{E} e^{-i\omega t} + c.c. \tag{1.2.5}$$

Analyzing the second term of the polarizability:

$$\vec{P}^2(t) = \varepsilon_0 \chi^{(2)}[\vec{E}e^{-i\omega t} + c.c.\vec{E}e^{-i\omega t} + c.c.] \tag{1.2.6}$$

$$\vec{P}^2(t) = \varepsilon_0 \chi^{(2)}[2\vec{E}\vec{E}^* + \vec{E}^2 e^{-i2\omega t} + c.c.] \tag{1.2.7}$$

$$\vec{P}^2(t) = 2\varepsilon_0 \chi^{(2)}\vec{E}\vec{E}^* + \varepsilon_0 \chi^{(2)}\vec{E}^2 e^{-i2\omega t} + c.c. \tag{1.2.8}$$

The last equation shows that there is now the generation of a wave at twice the frequency, consequently twice the energy. This is the process of second harmonic generation, a special case of sum frequency generation. The sister process of this is, difference frequency generation is often used to convert photon from the visible to the infrared.

It is interesting to note that all these processes are reversible, such that a single photon of higher energy can be converted to two photons of lower energy. The reverse process is called spontaneous parametric downconversion (SPDC) and crucial since it is one of the fundamental techniques for the generation of photon pairs used in quantum photonics shown in Fig. 1.3.

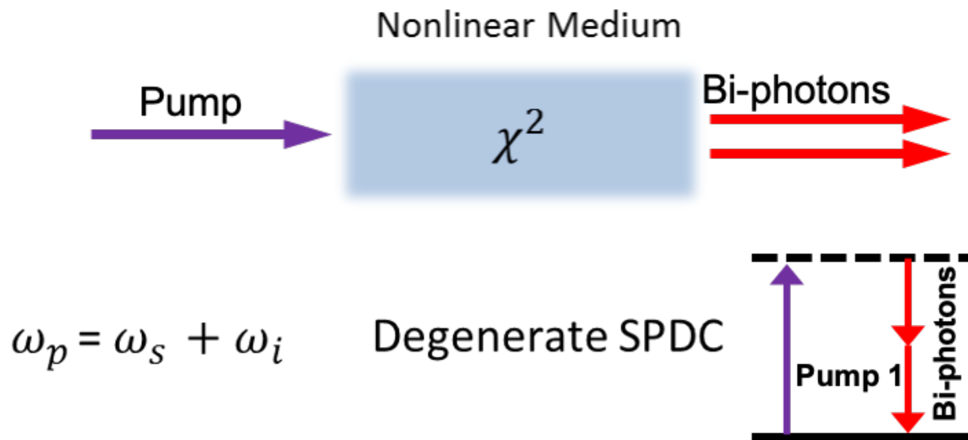

Figure 1.3: Energy diagrams representing the pump and signal/idler structure for energy degeneracy in spontaneous parametric downconversion.

If the material of interest is centrosymmetric there is no access to the second order susceptibility and one must move to the next higher order term, the third order susceptibility. This process is called four wave mixing where two input pump photons create two new photons

from the interaction. These photons that are produced are a bi-photon pair just as in SPDC and useable as such. In the diagram below it can be seen that two photons, either spectrally degenerate or non-degenerate, enter a material (silicon for example). Interaction between the pump photons and the material will produce two new photons that must preserve energy and momentum conservation, hence meeting the phase matching conditions. This process has applications beyond the scope described here such as for the generation of pulsed lasers, comb generation, and supercontinuums. This is due to the fact that initially in a material with a single pump wavelength, two spectrally degenerate photons will interfere with themselves producing two new wavelengths. These new wavelengths though can now interfere as well producing new wavelengths, thus the process self-perpetuates adding new wavelengths and spectrally broadening the bandwidth of the original source.

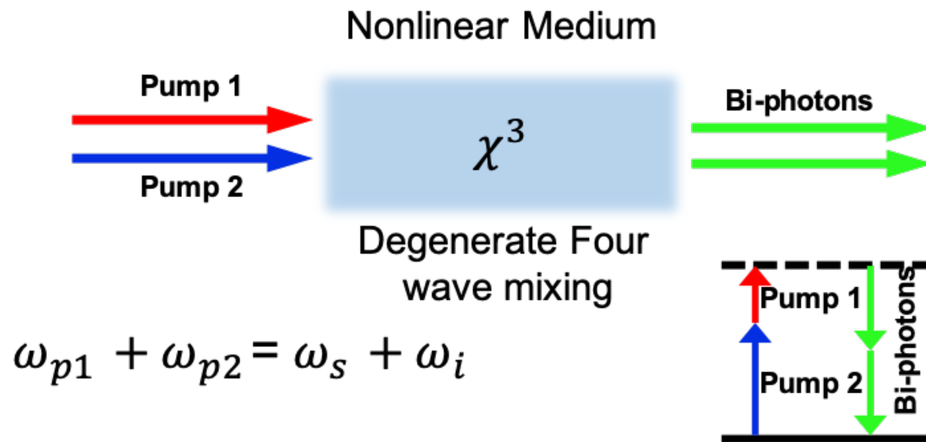

Figure 1.4: Energy diagrams representing the pump and signal/idler structure for energy degeneracy in spontaneous four wave mixing.

The last quality of the third order susceptibility that becomes relevant for photons, especially where loss is of concern is two photon absorption (TPA). Two photon absorption stems from the imaginary component of the third order susceptibility, just like linear absorption comes from the imaginary portion of the first order term. The manifestation of TPA comes when the sum of two photons is greater than the material bandgap and then they can be absorbed, causing added loss to the system. This is a case where ultrawide-bandgap materials shine as the required single photon energy is very large for this process to occur.

1.3 Integrated Photonics

Bulk optics are the conventional platform for the demonstration of these experiments over the years but the platforms scalability become quickly intractable. Combining the scalability requirement with the need for phase stability, and increased electric field intensity for the generation of photon pairs, integrated photonics is the logical path to follow. Integrated photonics is just the process of confining light (photons) to structures on an integrated chip, such as a silicon waveguide. The waveguides follow the same constraints as optical fibers where total internal reflection past the critical angle due to the index of refraction difference between the higher index core, and lower index cladding confine the light to the core. The higher the difference in the indices of refraction, the stronger the confinement, and the higher the electric field intensity.

$$\theta_c = \arcsin\left(\frac{n_2}{n_1}\right) \tag{1.3.9}$$

Integrated photonics has the added benefit that structures are not limited to the constraints imposed by that of optical fiber. The only limit now is the quality and resolution of the fabrication equipment at a university or industrial partner. This allows for the creation of integrated analogs of conventional fundamental bulk optic components such as cavities (ring resonators), beamsplitters (evanescent couplers), filters (Bragg gratings) to name a few. The final question comes as to the material of choice for the integrated waveguides.

1.4 Materials

A number of materials exist that make excellent candidates for integrated photonic platforms. In this section a number of these materials will be described with their strengths and weaknesses. One overall constraint is that eventually the material selected should be able to be inserted into a foundry process, advancing quantum technologies from the research stage to commercial viability [14].

Capitalizing on the tremendous investment from the CMOS industry integrated photonics

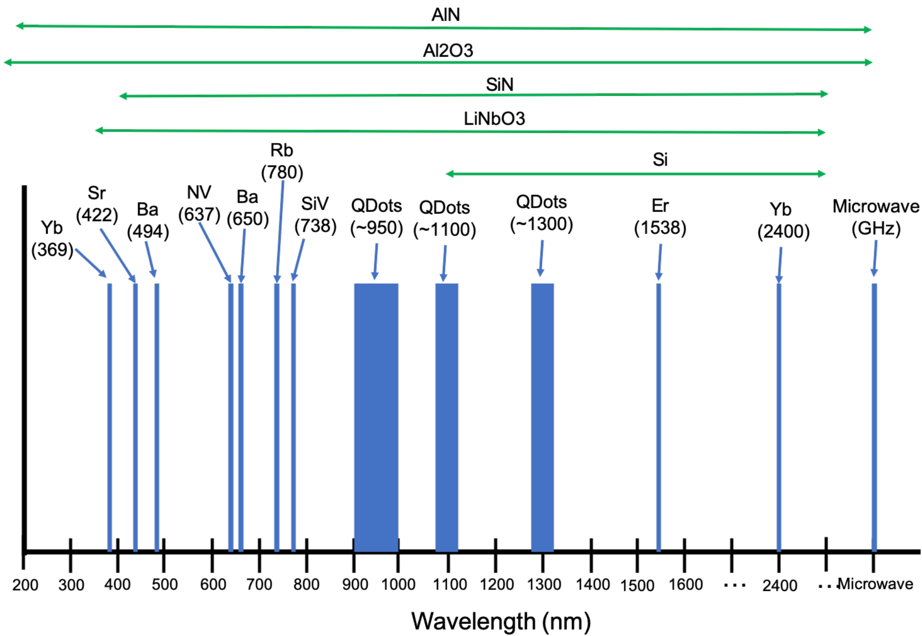

Figure 1.5: The chart shows a subsection of the available quantum technologies with the corresponding wavelengths of interest. Whether these are used as single photon sources or quantum memories the interaction wavelengths are noteworthy when the various quantum technologies must coherently pass quantum information across the platform.

in silicon has had the largest growth of any of the available materials. Constructing silicon photonic devices in a commercial fabrication facility is almost commonplace now for commercial telecommunication components (1250 - 1650 nm) [14]. With a bandgap of 1.1 eV, silicon has a transparency down to 1100 nm for optical components, and functions as a photodetector below that range. This makes silicon an ideal material for quantum photonics in the infrared but rules out the integration of most quantum memories.

The second most common material in commercial foundries is silicon nitride. With a much larger bandgap of 5 eV, thus transparency down to 250 nm, silicon nitride looks to be an ideal candidate for a multi-octave spanning photonic platform. It is worth noting that silicon nitride is polycrystalline when deposited and depending on grain size will act as a scattering site for short wavelength photonic applications (<400 nm). Above 400 nm silicon nitride is a great material for quantum photonics for example in comb generation [15], laser radar [16] , and biosensing [17].

Sapphire is transitioning from a bulk optics material to an integrated photonics material as well. With a tremendously large bandgap of 8.8 eV, sapphire is low loss from 200 nm to 5000 nm. Sapphire has been used to show multiple wavelength photonic circuits for the ion trapping community [18] and as a doped medium for lasers. The drawbacks of sapphire are the material hardness making processing difficult, and the lower index contrast between it and cladding materials requiring larger structures.

Another very promising material which has been in use for a couple decades is lithium niobate. The material is a staple material in which to make high speed modulators from since the material exhibits the electro-optic effect (index of refraction change with applied voltage) due to the crystals non-centrosymmetry. A strong second order nonlinear susceptibility is a consequence of the non-centrosymmetry with lithium niobate having one of the largest at 27 $\frac{pm}{V}$ [19]. With a bandgap of 4 eV, thus transparency to 310 nm, lithium niobate covers the visible to the infrared. Though like silicon nitride below 400 nm the material has absorption which can lead to catastrophic optical damage. The material though is being used for optical waveguides, and very notably as a source of entangled photons for quantum applications.

Lastly, aluminum nitride (AlN) has one of the widest bandgaps at 6.2 eV of any semiconductor, and transparency to $\sim$197 nm, with attractive electronic and photonic properties. This broad transparency from 200 nm to 15,000 nm makes it one of the largest optical windows in existence next to sapphire. This broad spectrum makes it attractive for applications including UV spectroscopy [20, 21], optical waveguides for modular quantum computing with atomic memories [22–26], nonlinear photonics throughout the UV to infrared [27], and solar-blind communications [21]. Many atomic transitions are in the UV or visible (VIS) spectrum, including Ytterbium ions ($^{171}Yb^{+}$), Strontium ions ($^{88}Sr^{+}$), Barium ions ($^{138}Ba^{+}$), and nitrogen vacancy (NV) centers in diamond, which have important optical transitions at 369.5 nm, 422 nm, 650 nm, and 637 nm, respectively. Recent work demonstrates the utility of integrated optics to perform quantum coherent operations on the optical qubit transition of $^{88}Sr^{+}$ at 647 nm [28]; the UV transmission of AlN-on-sapphire would also enable $^{88}Sr^{+}$ initialization at 422 nm or driving the 369.5 nm wavelength of $^{171}Yb^{+}$. Autofluorescence of silicon nitride (SiN)

presents a challenge for pumping the diamond NV center at 532 nm [29]; this fluorescence is greatly reduced in AlN-on-sapphire, opening the path to large-scale photonic integrated circuits for atom-like qubits in diamond.

Electro-optic modulation presents an important capability in many applications, such as architectures for modular quantum computing. AlN has a relatively large electro-optic coefficient, and fast electro-optic modulation (∼4.5 Gb/s) has been demonstrated with AlN's high c-axis electro-optic coefficient (r_{33} = 1 pm/V) using sputtered AlN [30, 31]. Piezo-electric actuation of photonic devices has also been shown with optomechanical resonators [32] and can potentially achieve very high modulation depth [33] and can potentially be used to frequency transduce from the optical to the microwave for superconducting qubits. Lastly, AlN has a high second order nonlinear susceptibility $\chi^{(2)}$ (4.7 pm/V) [34, 35], as well as a third order nonlinear susceptibility with Kerr coefficient comparable to that of SiN (the n_2 for TE-like mode in the (001) plane is estimated to be $(2.3 \pm 1.5) \times 10^{-15}$ cm^2/W) [36]. These nonlinear properties allow for a number of nonlinear optical processes [37–39], including second harmonic generation [34, 40], sum/difference frequency generation [41], photon pair generation by spontaneous parametric down conversion [42], and four-wave mixing [36, 43]. The combination of the ultrawide-bandgap with these nonlinear and electro-optic properties make AlN a promising platform we have chosen for quantum devices and for other high-performance optics applications.

Chapter 2

Prior State of the Art

2.1 Characterization of Aluminum Nitride Films

This section will cover an array of different characterization techniques from the literature that can be used to characterize aluminum nitride and its alloys. The characterization of nanomaterials is a vastly growing research area as these materials become prevalent and as the structures continue to reduce in physical size. For example, the general rule of thumb is that the resolution limit of an imaging system is half the wavelength of the system. Thus, a microscope using violet light, 400 nm, would have a resolution of 200 nm. This resolution limit is too coarse for materials one hundred nanometers or less in their dimensions. To characterize these materials and structures one must utilize different techniques than those often used for bulk samples. That being said, bulk sample characterization techniques can give indications of what to expect with the nanomaterials. This can often be the case with materials that are optically transparent in the visible wavelength regime such as aluminum nitride (AlN). Aluminum nitride, having a bandgap of approximately 6.2 eV, is optically transparent from 200 to 15,000 nm. Consequently, in the visible wavelength regime one can visually inspect the film for transparency, giving an indication of the film quality [44, 45]. Defects or other impurities will cause the material to become optically opaque, increasing from yellow to eventually brown as the defect concentration increases [46, 47] . As shown in Fig. 2.1, different areas of the bulk sample of AlN were exposed with a tungsten and deuterium lamp and the output was

collected with an ultraviolet/visible spectrometer. Collecting the input, T_0, and transmitted light, T, with a spectrometer allowed for a broad bandwidth wavelength scan to be completed for the sample. Knowing the thickness of the sample, d, allowed for the calculation of the absorption coefficient, α, from the following equation which is then plotted in Fig. 2.1.

$$\alpha = -\frac{1}{d}\ln\frac{T}{T_0} \tag{2.1.1}$$

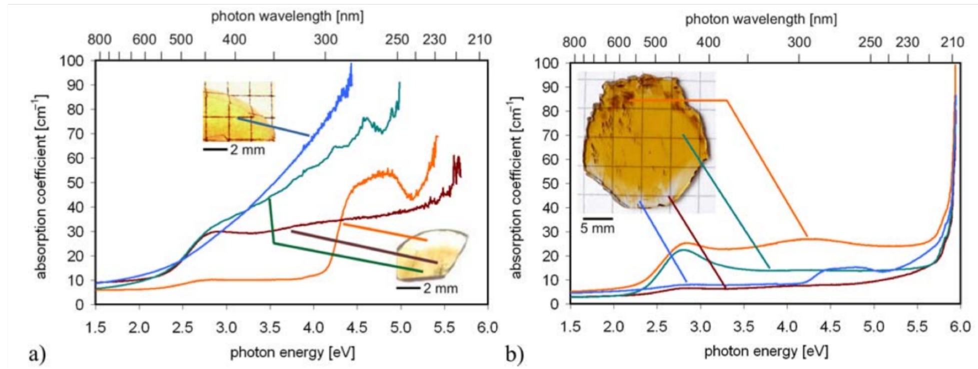

Figure 2.1: Absorption coefficient vs photon energy plotted for two different substrates (a) normal, and (b) grown in an oxygen deficient atmosphere [48].

In both plots it is obvious that the more opaque the region the higher the absorption coefficient red shifts shifts. With the removal of oxygen from the growth atmosphere the absorption coefficient significantly drops. Deconvolving these curves with Gaussian fits allowed for the regions contributing to the features to be identified.

Analysis of these different Gaussian curves correlated to distinct absorption bands for the aluminum vacancy at 3.59 eV, substitutional oxygen at 5 eV, and oxygen-vacancy complexes at the 4-4.55 eV range and these different defects are visualized in Fig. 2.3. Thus, correlating to a large oxygen concentration rendering the sample opaque due to the absorption bands in the 2.5-5 eV range. The yellowish coloration is caused from absorption in the blue spectral region, giving a peak around 2.78 eV. This coloration does not always correlate to ultraviolet absorption when the peak is still in the blue regime.

Obtaining defect free AlN, allows one to possess a material with multi-octave spanning wavelength transparency, along with a material that is non-centrosymmetric in the crystalline

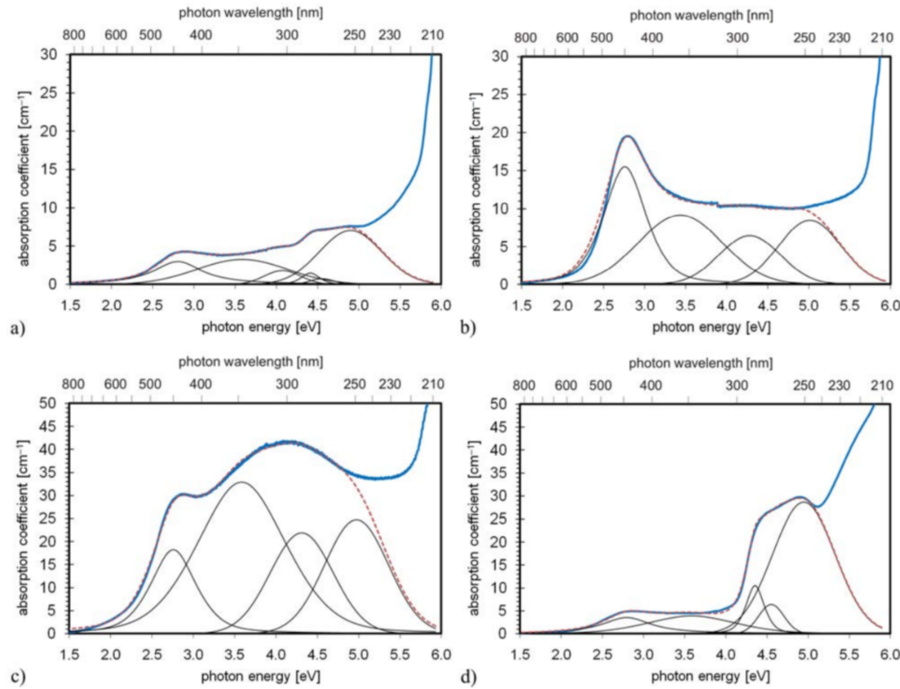

Figure 2 Sample absorption spectra (thick blue line) and their deconvolution into Gaussian functions (thin black lines). The red dotted line represents the summary curve of all Gaussians. The spectra are taken from: a–c) colorless, yellowish, and brownish areas of the sample shown in the inset of Fig. 1b; d) the transparent area of the sample shown in the right inset of Fig. 1a.

Figure 2.2: Deconvolution of the absorption spectrum into the Gaussian contributions. The relate to the following sections of the wafer (a) colorless, (b) yellow, (c) brown, and (d) transparent region of the oxygen deficient atmosphere wafer [48].

structure allowing access to the second order nonlinearity and the electro-optic effect. This makes AlN an ideal material for use in optical waveguides for the infrared, visible, and the ultraviolet. The next section will cover a short introduction to the fabrication of AlN thin films.

Aluminum nitride is grown in by several different methods depending on the intended application. First, the material is most stable in the wurtzite phase and thus the best substrates are those which have a hexagonal structure closely matching the lattice constant of the material. The crystalline structure is shown in Fig. 2.4, which indicates the c and m planes of the crystal [50–52].

The ideal substrate to grow AlN as with any crystal is a native bulk substrate, and this is typically grown by sublimation and condensation from a small seed crystal as shown in Fig.2.5.

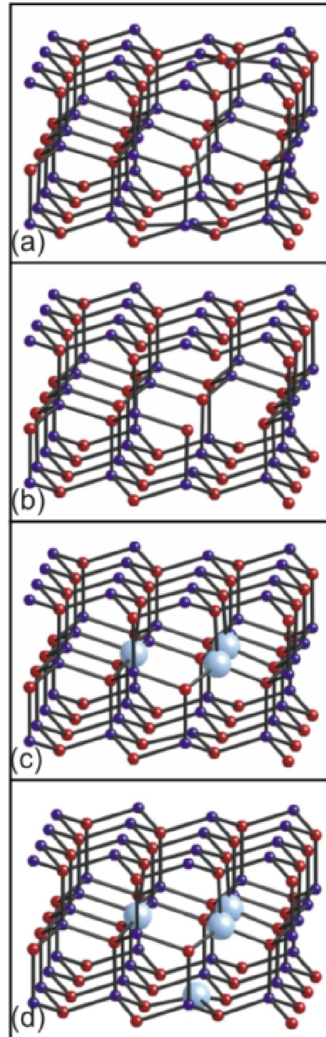

Figure 2.3: Visualization showing the different defect states in AlN, (a) aluminum vacancy and nitrogen vacancies, (b) aluminum vacancy and nitrogen vacancy complex, (c) aluminum vacancy and oxygen substitutional complex, and (d) aluminum vacancy and oxygen substitutional complex [49].

To minimize defect concentration to the substrate these chambers are purged of oxygen and other contaminants.

The bulk substrates can be diced and cleaved to produce thinner wafers for the growth of films [53]. There is research as well on utilizing smart cut technology and selective growth of two dimensional materials to directly produce high quality thin films from these wafers that can be transferred to a non-native-based substrate. If AlN native substrates are not used the

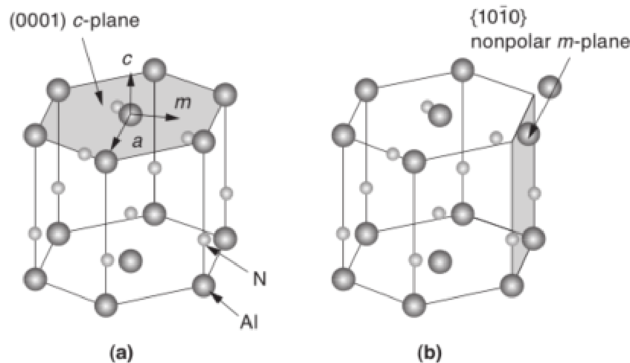

Figure 2.4: Unit cell of AlN showcasing the c and m planes of the individual crystal [12].

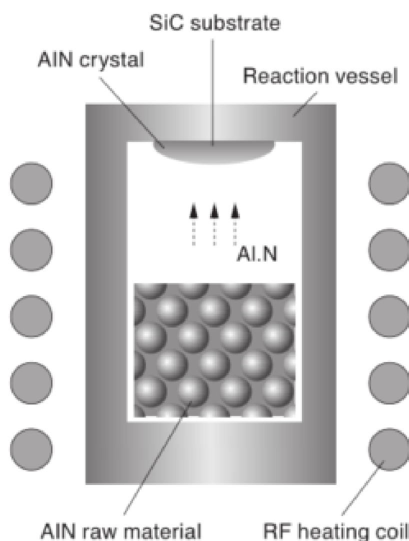

Figure 2.5: Growth chamber for AlN bulk substrates through sublimation of AlN raw material which is heated and then condenses on a seed crystal located at the top of the chamber [53].

typical growth substrates are sapphire (13% lattice mismatch for c-plane) and silicon carbide (6H $<$1% lattice mismatch for c-plane) [54–59]. The growth of the film can occur by a number of different techniques producing different quality films. Polycrystalline films are produced from DC sputtering, magnetron sputtering, and laser pulse deposition whereas increased crystallinity films are produced from molecular beam epitaxy, chemical vapor deposition, and atomic layer deposition. By whatever way the films deposited they require characterization

which is what will be described in the next section.

2.1.1 Atomic Force Microscopy

Atomic force microscopy (AFM) is the process of using an ultra-fine probe tip to measure the profile of a surface structure. The force between the tip and the surface is measured by the deflection of a laser beam on a quadrant detector correlating to changes in surface features. Whether the force is produced from direct contact between the probe tip and the film or by the field interaction from the tip above the surface, the surface can be mapped to give detail on the surface structure. This is shown in Fig. 2.6, where the average height across the 40 nm thick film had an average variation of approximately 250 pm.

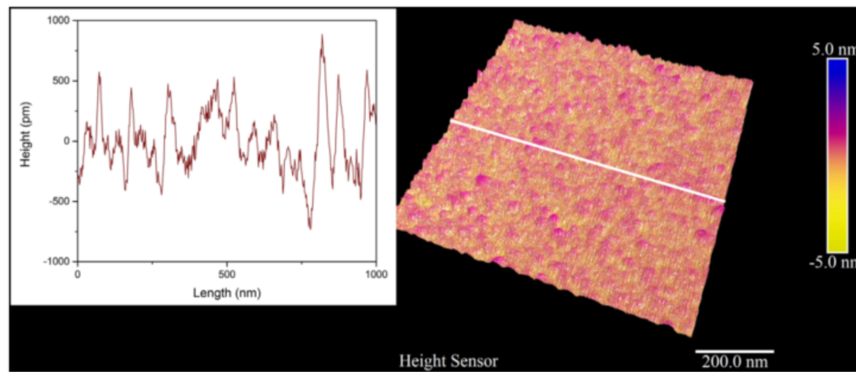

Figure 2.6: AFM map of a 40 nm AlN thin film. The average variation across the film was approximately 250 pm [44].

A second group of researchers produced a 100 nm AlN film and utilized the AFM characterization beyond the surface mapping features. The authors certainly characterized the film thickness and uniformity across the sample and found variation on the order of less than 10 nms. Beyond this single sample, the samples were grown at a number of different temperatures to see the effect on the crystallinity and crystal structure. When the samples were grown at temperatures below 500 C, the film was found to be relatively flat and free of peaks. This was correlated to the branching of the hexagonal crystals in all directions. When the samples were grown at temperatures of 500 C and above, uniform height bumps covered the film surface.

These surface features correlated to highly oriented (vertical) pillars in the crystal structure and little to no crystal branching. This is clearly shown in the AFM's in Fig. 2.7.

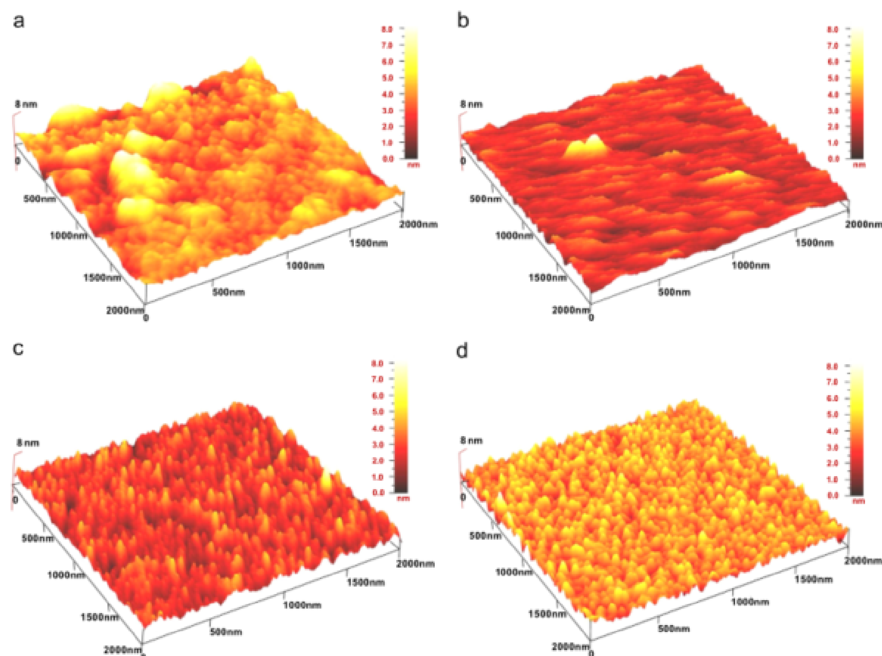

Figure 2.7: AFM map of the 100 nm AlN thin films grown by magnetron sputtering at various temperatures (a) 300 C, (b) 400 C, (c) 500 C, and (d) 600 C [59].

The authors continued the study by selecting a set growth temperature of 500 C which gave very nice highly oriented crystalline films and varied the ambient nitrogen concentration in the growth chamber. The growth was continued at two different nitrogen concentrations, 60% and 30%, and found that the branching occurred with low nitrogen concentrations as well shown in Fig. 2.8.

Now there was a known growth temperature and nitrogen concentration to produce high quality AlN films in which one could fabricate optical waveguides. The surface roughness of 10 nm could be a problem as a scattering site for transverse magnetic (TM) oriented modes in an optical waveguide but perfectly fine for transverse electric (TE) mode waveguides. This is because the mode will be confined below the surface, only weakly interacting with the film surface and therefore the roughness will not serve as a significant loss mechanism. Secondly,

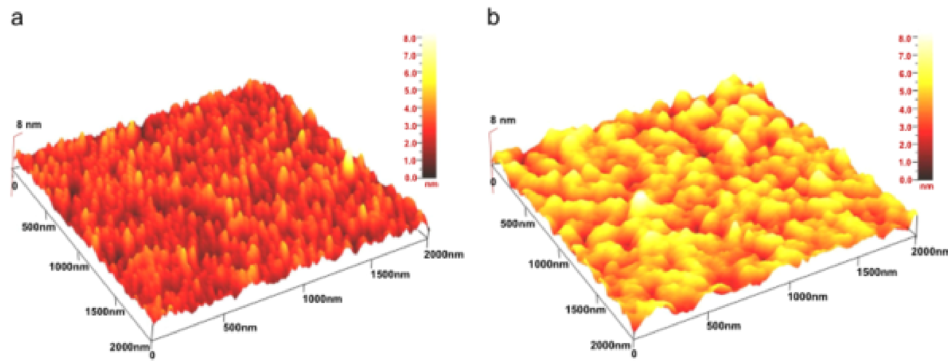

Figure 2.8: AFM map of the 100 nm AlN thin films grown by magnetron sputtering at various nitrogen concentrations(a) 60%, and (b) 30% [59].

the branching structure of the crystals with obvious grain boundaries traversing the optical waveguides, would add scattering sites and increased optical loss. These highly vertically oriented films are very similar to the commercially available films from Kyma. The next question that arises is how does the inner structure of the sample correlate to the external. This can be understood with transmission electron Microscopy (TEM) and high resolution transmission electron microscopy (HR-TEM) which will be discussed in the next section.

2.1.2 Transmission electron microscopy & HR-TEM

Utilizing focused ion beam milling one can prepare very thin samples of the produced films for characterization of the inner dynamics of the sample. This includes analysis of the atomic arrangement, defects, and lattice matching to the substrate. In a very relevant study the authors prepared TEM ready samples of AlN films grown by sputtering on silica films after the material was etched for an optical waveguide. The TEM was used to analyze the orientation of the crystal structure. The sputtered film was found to be highly vertically oriented with minimal branching of the crystals. This was crucial to know as it was confirmation that the crystals were aligned correctly to minimize scattering along the propagation direction of the waveguide. While the sample was inside the TEM, an energy dispersive X-ray (EDX) analysis study was conducted to verify the material content of the components. The EDX

confirmed that the silicon and oxygen remained in the cladding layers of the waveguide, while the aluminum and nitrogen remained in the core. There was not a noticeable diffusion of the materials into/out of the optical waveguide as shown in Fig. 2.9. This confirmed that the waveguide would have only minimal contribution from defect site induced absorption.

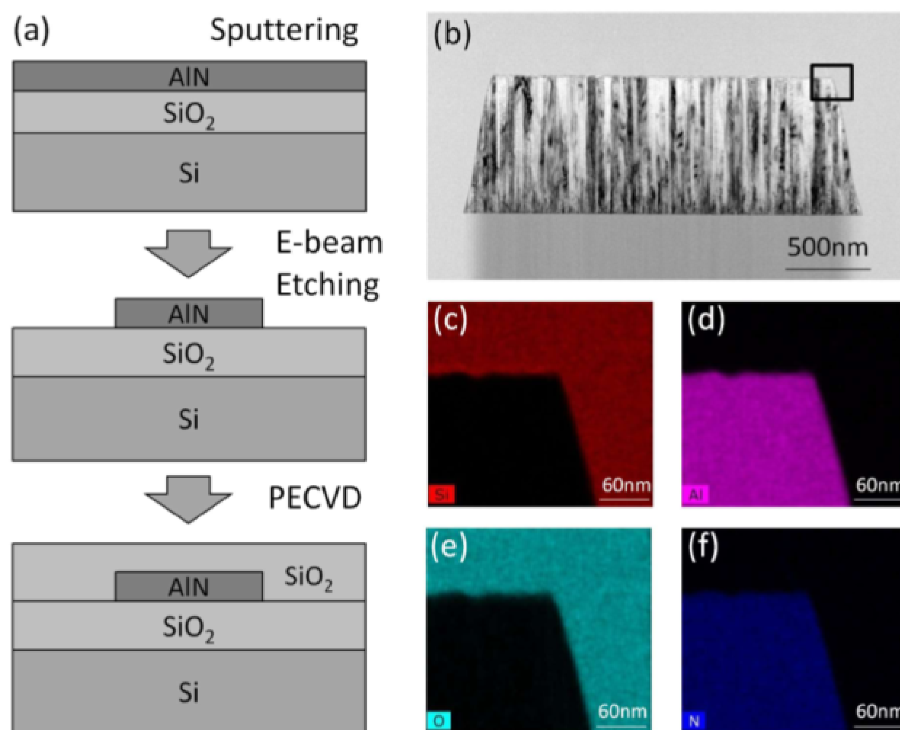

Figure 2.9: (a) Fabrication step of the waveguide, (b) TEM image of the optical waveguide showing the vertically oriented grains, EDX maps of (c) silicon, (d) aluminum, (e) oxygen, and (f) nitrogen [60].

Further study of the material can be collected in a TEM while utilizing phase contrast to image the individual crystalline layers in high resolution mode. This method allows characterization of the zone axis and crystal planes associated with the film and any defect boundaries that are present. In a separate study, researchers characterized aluminum nitride thin films utilizing HR-TEM to find defect and growth condition associated with the grown films. The first area of interest is the boundary between the silicon carbide substrate and the AlN film as shown in Fig. 2.9. Though silicon carbide has a higher optical index of refraction than AlN,

thus it cannot be used as a cladding material to maintain total internal reflection for waveguide, it provides very well aligned films. The authors in this study grew wurtzite phase AlN on wurtzite silicon carbide and viewed the boundary under HR-TEM. Aided by the increased magnification, the lattice boundary of the silicon carbide and AlN is clearly visible and shows a well-defined AlN film above shown in Fig.2.10.

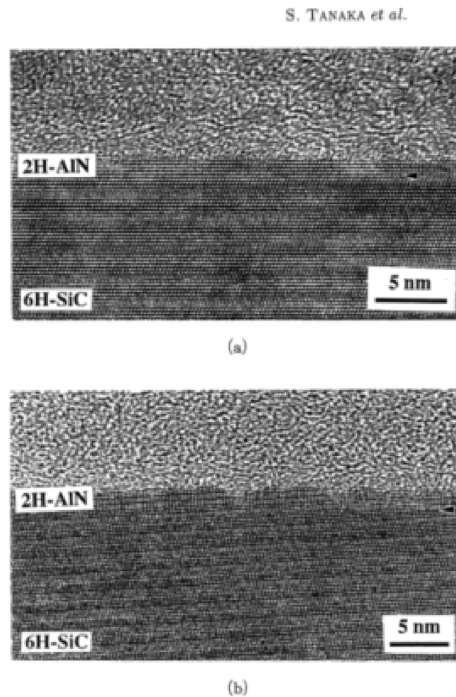

Fig. 1. Cross sectional views of a 2H(wurtzite)–AlN(0001) film deposited simultaneously on both (a) on-axis and (b) vicinal 6H-SiC(0001) substrates. Arrows indicate the AlN/SiC interface.

Figure 2.10: HR-TEM image of the interface between wurtzite AlN and silicon carbide. The lattice planes can be seen as well as the transition between the two materials [61].

In Fig. 2.10 the films were grown in oxygen deprived environments. If care is not taken to isolate the deposition chamber from stray oxygen, the oxygen will assume new lattice sites in the AlN crystalline matrix. In situations, such as this shown in Fig. 2.11, oxygen has replaced lattice sites and formed aluminum oxide compounds in the stable AlN lattice. These new AlN-Al2O3 sites cause an inversion domain boundary. The inversion domain boundary appears as a flipped stripe in the HR-TEM image and shows a periodicity of about 1 nm, to

the defect as it propagates in the growth direction.

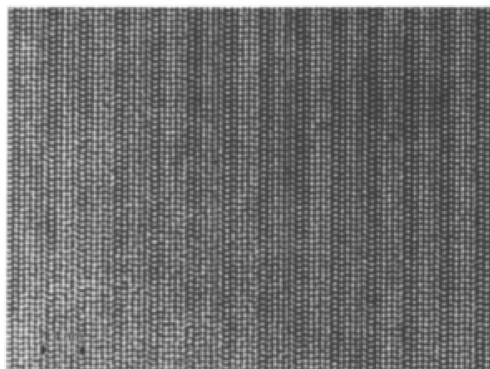

Figure 2.11: HR-TEM image of the inversion domain boundaries caused by oxygen defects forming during the growth of the AlN lattice [52].

Rotation of the sample shown in Fig. 2.12, reveals the corrugation of the inversion domain boundaries that occur in the AlN film. These boundaries reveal changes in crystal structure and unfortunately can serve as scattering and absorption sites in an optical waveguide. The benefit of the generation of the bound Al-O is that sapphire has a higher bandgap than pure AlN and will not affect the optical absorption of the material but it will affect the effective nonlinear susceptibility due to the reduction of pure AlN. If there were free oxygen (substitutional or vacancy sites), this would affect the absorption of the resulting film.

A final prevalent technique utilized to qualify the elemental composition of the film is x-ray photoelectron spectroscopy (XPS) which will be discussed below.

2.1.3 X-Ray Photoelectron Spectroscopy

In x-ray photoelectron spectroscopy, an incident x-ray beam is focused on a sample surface. The focused x-rays free electrons from the material in the first 10 nm and the kinetic energy of those emitted electrons is measured. The measured kinetic energy of the emitted electrons gives information about the binding energy as in Fig. 2.13, elemental composition, and even the electronic state of the material. These qualities are very useful to know as they will verify if the surface has developed an oxide, which is common in AlN films. The formation of an

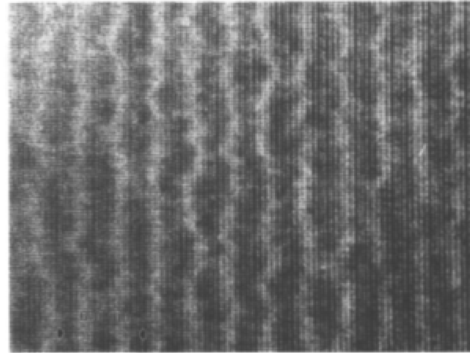

Figure 2.12: Rotated HR-TEM image which shows the corrugated nature of the inversion domain boundaries in the AlN film [52].

oxide is not necessarily detrimental to the waveguide as it will seal the structure. The question that needs to be answered is if the oxygen has penetrated deeper than the oxide coating.

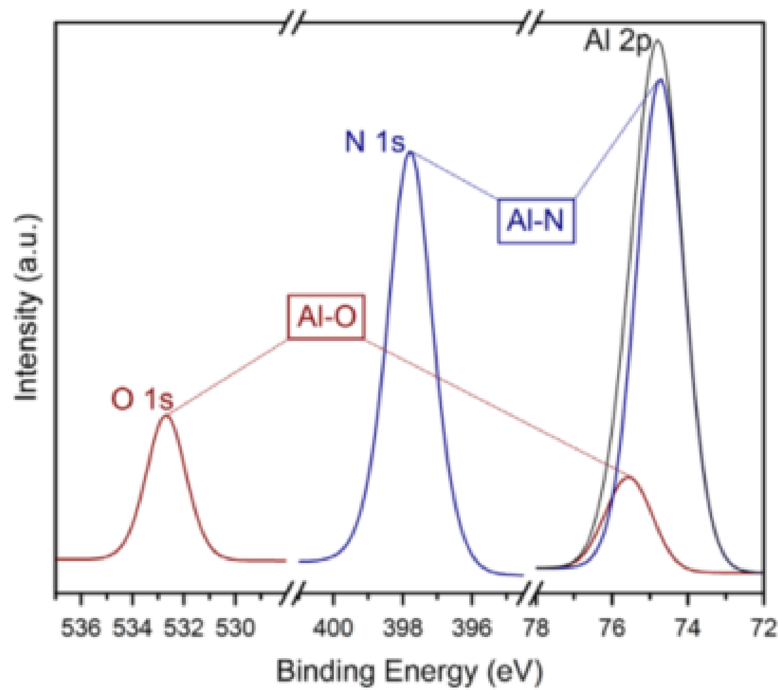

Figure 2.13: Illustration of the characteristic related peaks and respective binding energies found in AlN films characterized by XPS [44, 62] .

The authors prepared a 40 nm film of AlN grown by plasma enhanced atomic layer deposition grown on silicon 111 for XPS analysis. The sample was measured before and after a 20 minute etch to characterize the effect the etchant was having on the sample and expose subsurface features. The results are shown in Fig. 2.14.

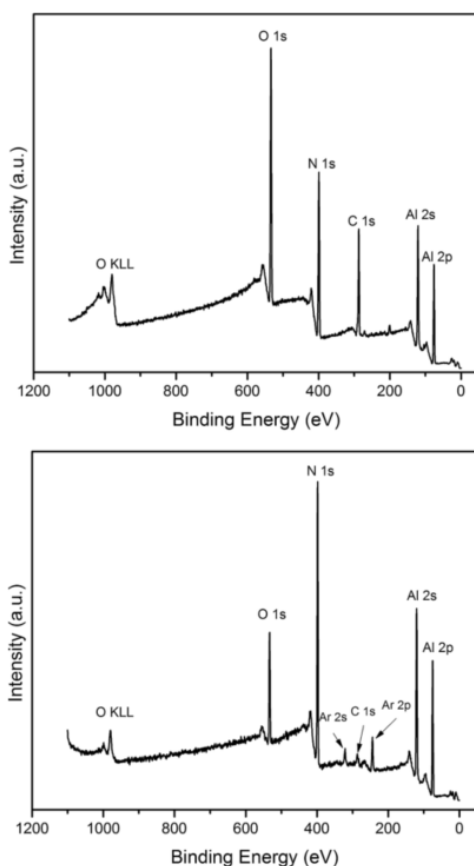

Figure 2.14: XPS collected plots (a) before etching, and (b) after 20 minutes of etching has occurred [63].

The XPS plot before the etching exhibits a large oxygen 1s peak, aluminum, nitrogen, and carbon peaks. After the etching, has occurred, the oxygen, and carbon peaks are reduced, whereas the nitrogen and aluminum peaks have increased in intensity. This confirms that there was a thin native oxide layer on the AlN film as well as a layer of carbon contamination. Once the material was etched, the oxide and contamination were removed, revealing the AlN film with a minor amount of oxygen impurities. These results revealed a very pure film

with a large bandgap, capable of producing photonic devices well into the ultraviolet. Once the material has been characterized and deemed worthy of proceeding on with fabrication photolithography is performed and photonic devices are created. These designed devices must in themselves be characterized by scanning electron microscopy or helium ion microscopy since AlN has a tendency to charge during imaging. The following section on prior state of the art will describe devices already fabricated.

2.1.4 Scanning Electron Microscopy & Helium Ion Microscopy

Optical loss is tremendous concern when fabricating photonic structures and can arise from a number of different variables, scattering/roughness, absorption, poor feature definition/fabrication errors, and grain boundaries to name a few. The absorption and grain boundaries have already been discussed above, so in this section the physically defined features are addressed. The scale of these photonic structures is on the order of ten to a couple hundred nanometers, well below the capability of an optical microscope. Larger features certainly can be seen in a higher resolution optical microscope when available. For fine detail though, researchers turn to a particle that has a higher resolution due the inherit wavelength, the electron. Electron microscopy is essential for observing small nanometers sized features as shown in Fig. 2.15. Regions of particular interest for optical structures is the sidewall roughness of an optical waveguide, the spacing of elements of a grating coupler, the amount of residual resist on a surface, and the reproducibility of the intended design across a wafer.

Many times to reduce errors from fabrication, researchers will build a safety net into their devices. Here the grating coupler was designed by the authors to have a 14° slope on each side of their waveguide to compensate for etching variations and minimize sidewall roughness that the waveguide mode will interact with. Visible in Fig. 14, the trapezoidal nature of the waveguide is apparent, and the SEM measurement confirmed the designed 14° slope. Secondly, the sidewalls roughness is visible in the ribs of the grating coupler, thus verifying the need for the trapezoidal shape of the optical waveguide to reduce field interaction with the sidewalls. The need for high quality imaging of the optical waveguides was further shown in

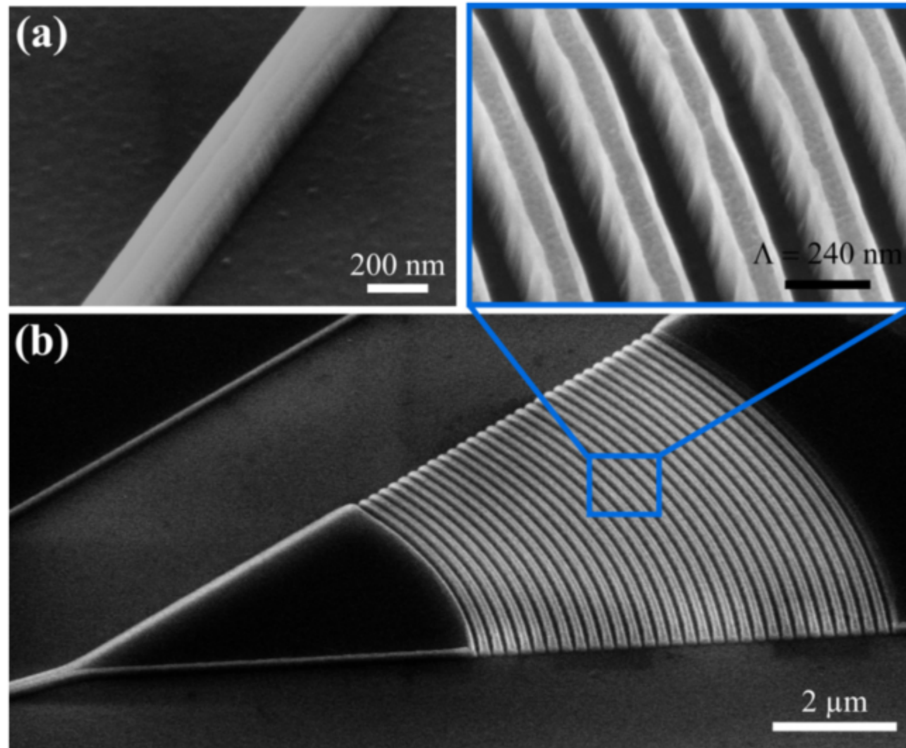

Figure 2.15: SEM images of the grating coupler constructed in a 140 nm thick AlN film showing the (a) individual rib of the grating coupler, (b) array of ribs, and (c) entire grating coupler [64].

a second paper with 500 nm AlN. In this article, the authors were fabricating waveguides for the generation of a second harmonic signal from an injected fundamental laser beam. These waveguides are constructed in a very linear dimension since they need to support the optical modes of the fundamental and the harmonic. Therefore, the wide nature allows the higher energy wavelength to be multimode, but have tight overlap with the generated lower energy mode which is single mode. Optical loss in the waveguides was larger than expected and can be attributed to contamination on the waveguide from residual organics and photoresist shown in Fig.2.16. One last point on imaging to express is that charging is a problem with insulating materials, such as ultrawide-bandgap semiconductors like AlN. Charging will manifest itself in an SEM image as a dark region with reduced contrast in the features.

Helium ion microscopy (HIM) utilizes a helium ion gun instead of an electron gun to excite

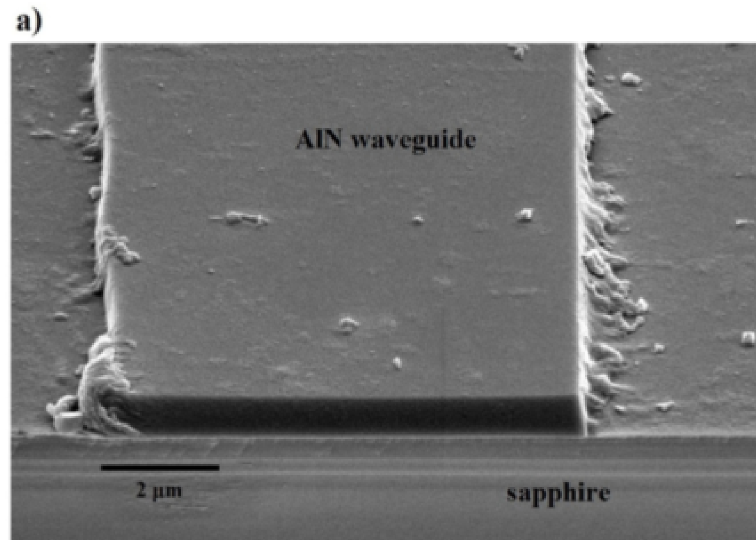

Figure 2.16: SEM of a multi-mode optical waveguide clearly illustrating the residual detritus left in contact from the fabrication process [40].

the sample to produce secondary electrons [65]. In an SEM, the surface collection of negative charges would reduce the resolution of the image. In a HIM system, there is an electron flood gun, which is used to counter the deposited charge from the ions and therefore eliminate sample charging. This added benefit vastly increases the variety of samples that can be imaged in the system.

Due the ease of charging materials such as AlN, HIM systems are the perfect candidate to use to image the material. Shown in Fig. 2.17 is an AlN constructed from a 200 nm film on a sapphire substrate. The waveguide sidewalls are shown with the minimal roughness from the fabrication process. The roughness from the vertical nanocolumn crystals of AlN are visible as well on the top surface of the optical waveguide.

The minimal sidewall roughness, smooth top surface, and lack of residual detritus showcase that the waveguide is well constructed and suitable to propagate an optical mode with minimal loss (scattering). Once the waveguide is successfully characterized, the device is ready to accept light. In the next section, a brief overview of prior state of the art in the field will be discussed.

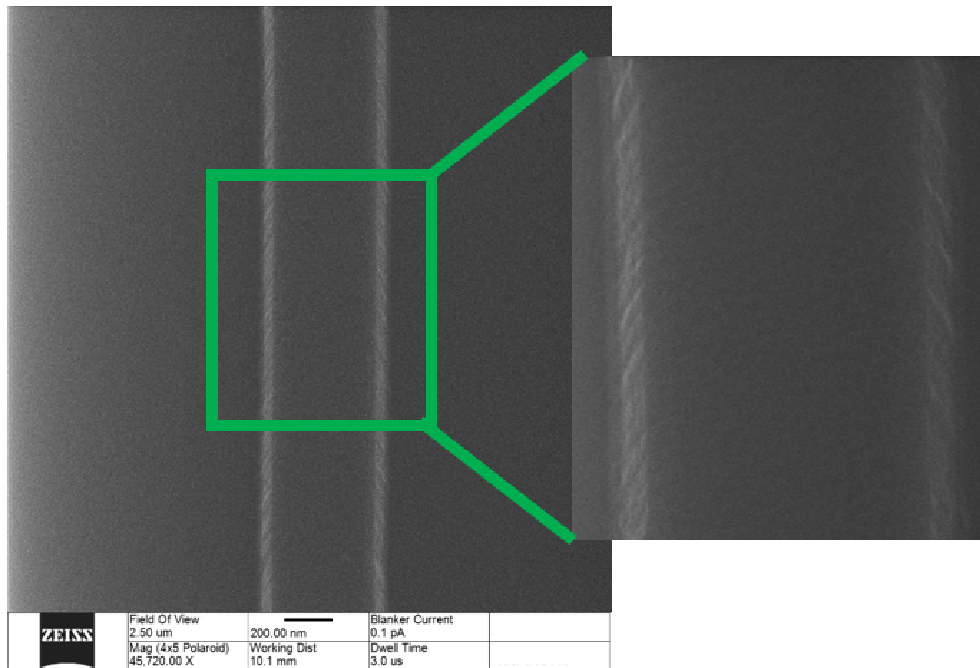

Figure 2.17: HIM image of a 200 nm thick AlN waveguide highlighting the low sidewall roughness [66].

2.2 State of the Art Devices

There has been an increasing interest in the aluminum nitride material platform in the last couple years with impressive results demonstrated by researchers around the world. This section will give a brief overview of some of the device research present in the field.

The second order nonlinearity in materials is very important as it allows for the use of the electro-optic effect (index change of a material with an applied electric field), and optical mixing in systems of three interacting waves. Examples of the optical mixing include second harmonic generation (ω to 2ω) and more general combinations such as sum and difference frequency generation (where two signals add or subtract to create a third). Not all materials can exhibit this second order nonlinearity and it is limited to those which are non-centrosymmetric as stated earlier in this section. Typically these devices consist of optical waveguides coupled to an optical microring resonator which will serve as a field enhancement cavity shown in Fig. 2.18. [67]

This paper is important as the authors were able to accurately measure the second order

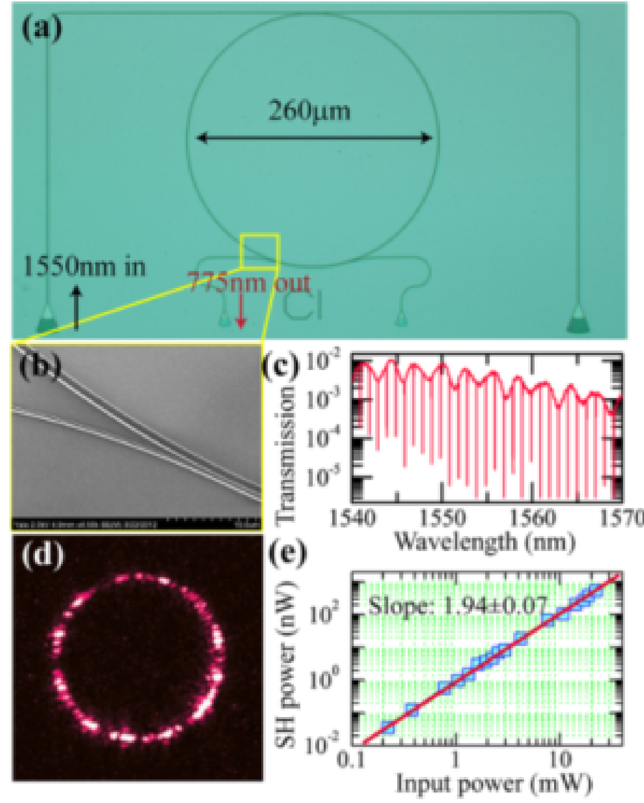

Figure 2.18: (a) 330 nm thick AlN waveguide structure with resonator enhancement cavity, (b) SEM of the optical waveguide/ring resonator coupling region, (c) resonance spectrum of the resonator, (d) resonator displaying 775 nm SHG light from a 1550 nm input, (e) log plot of the SHG conversion efficiency [68].

nonlinearity of the material which correlated with prior data. First step is the simulation of the device using a three-dimensional mode solver such as COMSOL to obtain the modal profiles of the two wavelengths of interest and their modal overlap, Γ. The model is used to determine the transmission spectrum of the ring, to determine the field enhancement factors, F_i(approximately maximum field strength divided by average field strength). Next, the input power into the waveguide and the converted power out of the waveguide are measured. These values are the plotted on a log plot which produce a straight line due to the quadratic dependence. The best fit of this line will give a coefficient which is the conversion efficiency, η. The other variables are the pump frequency, ω_p, the permittivity of free space, ϵ_0, the speed of light, c, the refractive indices for the wavelengths, n_i, the mode area, A_i, the ring circum-

ference, L, and the pump power in the waveguide, P_p. Inserting the modeled and measured values for this specific system, the author obtained a measured result of 4.7 ± 3 pmV proving that a useable level of second harmonic light can be created in AlN optical waveguides.

$$\chi^2 = \sqrt{\eta\Gamma \frac{8n_p^2 n_{sh} c^3 \epsilon_0 A_p^2}{F_p^2 F_{sh} \omega_p^2 L^2 P_p A_{sh}}} \tag{2.2.2}$$

Generation in a microring resonator does not have to be the only method and conversion can occur in straight, tapered, and periodically poled (quasi-phase matched, domain inversion to momentum match) waveguides. A very recent publication by Liu et al. has shown a new record for the material with a greater than 100 terahertz frequency comb in the ultraviolet down to 380nm shown in Fig. 2.19[69].

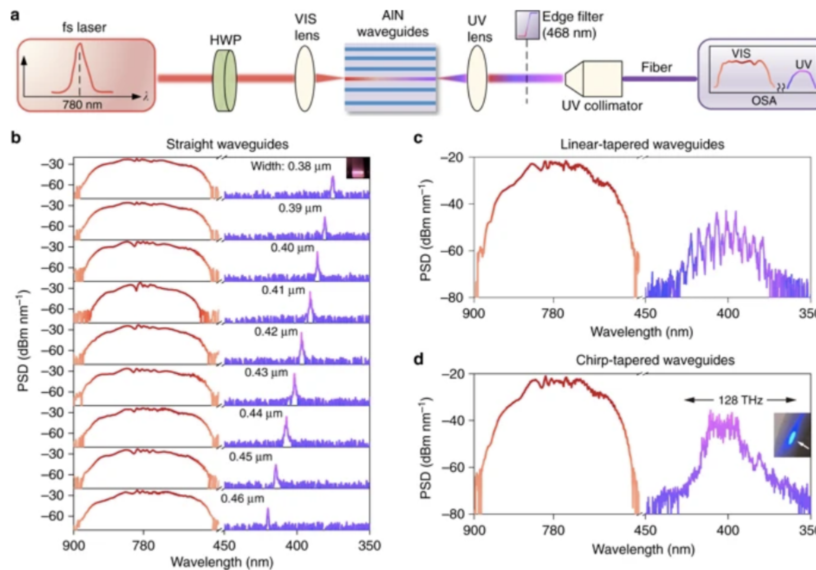

Figure 2.19: Figure showing optical frequency comb generation in the ultraviolet from a tapered crystalline aluminum nitride waveguide.[69]

The second order nonlinearity in aluminum nitride has been used to generate photon pairs [70], second harmonic signals [40, 68, 71, 72], optical frequency combs [60, 69, 73], and electro-optic modulators [74]. These are just a select few relevant recent publications I wanted to point out in the research field. In the next section I will discuss the research we have conducted to date [66].

Chapter 3

Characterization and Waveguide Fabrication

3.1 Aluminum Nitride Film Characterization

The requirements for low loss, relatively high optical nonlinearity, and access to the electro-optic effect drove the research to the selection of aluminum nitride as the material of choice. Since the intended operation of this material was as a platform on which to fabricate optical waveguides, that dictated that the substrate have a lower index of refraction than the AlN film. The commercially available option fitting this requirement is AlN ($n_i = 2.2$) on sapphire ($n_i = 1.77$), which is available from companies such as Kyma. Though Kyma's material was initially constructed for use in electronics fabrication the material has the proper specifications for our research. As highlighted in chapter 2, the AlN material that exists whether commercial or not varies in its quality depending on the growth parameters. This meant that for any obtained material, characterization was required before fabrication to set a valid reference baseline.

The research on the material platform is a joint effort between researchers at Massachusetts Institute of Technology (MIT), Rochester Institute of Technology (RIT), and the Air Force Research Laboratory (AFRL), where the fabrication was accomplished at MIT along with the

visible light testing, the device design and ultraviolet and infrared testing at RIT and AFRL. Once the initial samples were obtained, a number of characterizations were conducted. Fig. 3.1(a) illustrates the commercially available AlN-on-Sapphire wafers from Kyma Technologies, Inc., consisting of 430 μm sapphire (Al_2O_3) with a 200 $\pm$ 5% nm c-plane AlN film on the top layer. The c-plane AlN is grown on top of the sapphire substrate by pulsed DC magnetron sputtering, using a process called plasma vapor deposition of nanocolumns ($PVDNC^{TM}$). This method produces an AlN thin film that is crystalline with the [0001] direction parallel to the growth direction. Atomic force microscopy of the AlN thin film shown in the inset of Fig. 3.1(a) indicates a flat surface with 0.9 nm RMS roughness. High-resolution X-ray diffraction (HRXRD) measurements in Fig. 3.1(b) indicate the high structural quality of the AlN thin film. The ω scan of (002) and (015) AlN peaks shows full-width-half-maximum (FWHM) of 0.12 degree and 0.20 degree respectively, which is 10 to 20 times smaller than the previous results of AlN thin films deposited on amorphous silica [75]. The single crystalline wurtzite structure across the wafer is evidenced by the (015) ϕ scan showing six-fold symmetry (Fig. 3.1(c)). This flat surface and improved structural quality likely contribute to the low waveguide loss described in the next chapter. Fig. 3.1(d) plots the measured refractive index of the AlN film spanning from UV to VIS to near infrared wavelengths.

When operating the waveguides in the regime for single photon generation of light any background fluorescence can be detrimental to the system. Fig. 3.1(e) shows the power dependence of this platform's background autofluorescence using $\lambda = 532$ nm excitation pump. For comparison, Fig. 3.1(e) also shows the autofluorescence results of a SiN sample under the same excitation and collection conditions. The SiN sample has close to four times the amount of fluorescence intensity as AlN; however, the amount of autofluorescence is dependent on the SiN composition and method of deposition [76]. Furthermore, the photoluminescence (PL) from pumping the AlN is mainly from the underlying sapphire substrate [77]. Spectrally, this sapphire fluorescence is concentrated in a narrow band sapphire Cr line at around 690 nm, which can be easily filtered out by a notch filter and is not of relevance for the ultraviolet regime. This is more favorable for quantum applications compared to the broadband SiN

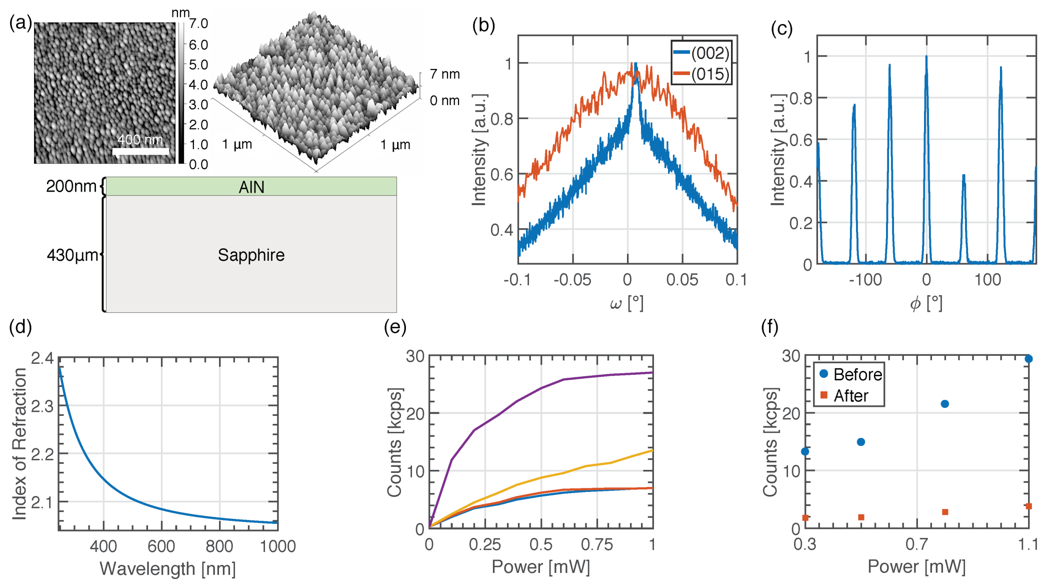

Figure 3.1: Properties of AlN-on-sapphire material. (a) Cross section illustrating each layer of the wafer, along with their respective thickness; top inset: atomic force microscopy scan of AlN film showing the nanocolumn size. Surface roughness is measured to be 0.9 nm RMS with 26.5 nm grain size (b) High resolution x-ray diffraction (002) and (015) ω scan of AlN. (c) (015) ϕ scan of AlN showing six-fold symmetry wurtzite structure. (d) Refractive index measurements using ellipsometry. (e) Background fluorescence from sapphire substrate (yellow), unpatterned AlN (blue), patterned AlN (orange), and stoichiometric silicon nitride (purple). (f) Background fluorescence from SiON top cladding, before (blue circles) and after (orange squares) bleaching.

PL from 620 nm to 800 nm, which overlaps spectrally to NV in diamond spectrum [29] and the pumping wavelength of 775 nm for SPDC at 1550 nm. A low autofluorescence makes AlN promising for interfacing with atomic transitions of ions [78], neutral atoms [79], and atom-like defects in diamond [29]. Initially after deposition, the SiON cladding exhibits some fluorescence comparable to SiN, but the fluorescence can be bleached away by optically pumping the material with the excitation laser, as shown in Fig. 3.1(f). Once the films are characterized, the next step is fabrication of the devices.

3.2 Fabrication

The fabrication of the devices designed at RIT was carried out at MIT with the complete fabrication process detailed in Fig. 3.2(a) . The process starts off with an unpatterned 1 cm

× 1 cm AlN-on-sapphire chip diced from a whole wafer. Next, a 5 nm thick Cr discharge layer is deposited via electron beam evaporation on the diced samples. Then, after oxygen plasma treatment under 100 W for 3 minutes to improve electron beam resist adhesion, hydrogen silsesquioxane (2% XR-1541) is spun on. The hydrogen silsesquioxane (HSQ) film thickness is measured to be ∼70 nm by using an AFM to measure the step feature profile after patterning. The patterns are written with an Elionix ELS-F125 electron beam lithography system at 125 keV using a dose of 10,000 μC/cm^2. The patterns are developed using a salty developer, which is an aqueous mixture of 1 wt % NaOH and 4 wt % NaCl, for high contrast [80].

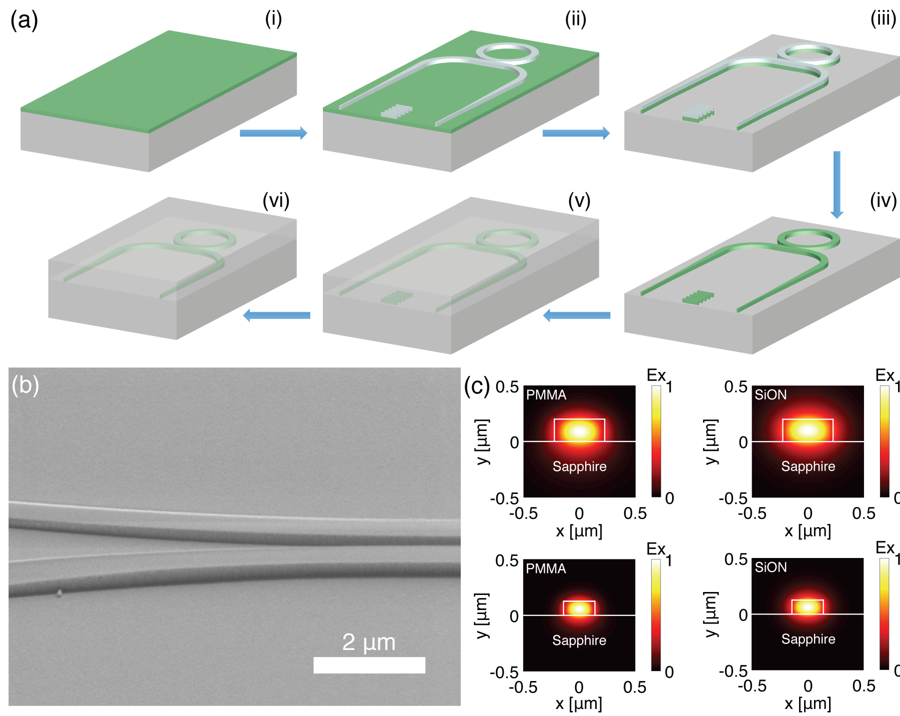

Figure 3.2: (a) AlN on sapphire photonics fabrication process: (i) Start off with an unpatterned AlN-on-sapphire chip diced up from a whole wafer. (ii) Spin coat HSQ (2% XR-1541), pattern using electron beam lithography, and develop using an aqueous mixture of 1 wt % NaOH and 4 wt % NaCl for high contrast. (iii) Etch by ICP-RIE using chlorine chemistry. (iv) Strip HSQ. (v) Clad with silicon oxynitride using plasma-enhanced chemical vapor deposition (PECVD). (vi) Edge polish for making the inverse-tapered edge couplers. (b) Scanning electron microscope (SEM) image of a fabricated AlN waveguide (c) Transversal component of TE mode in AlN waveguide for PMMA and SiON cladding for 638 nm (top) and 400 nm (bottom) wavelengths.

After HSQ mask patterning, the pattern is first transferred to the Cr layer at an etch rate

of 55 nm/min by electron cyclotron resonance reactive-ion etching (ECR-RIE) using a gas mixture of Cl_2/O_2 (3:1 ratio) at 300 W ECR power, 30 W RF Bias power, 10 mTorr pressure, and 25°C. Then, the AlN waveguides and photonic components are etched by inductively coupled plasma reactive-ion etching (ICP-RIE) using a gas mixture of $BCl_3/Cl_2/Ar$ in two steps. The first step is for etching the native aluminum oxide at an etch rate of 5 nm/min using BCl_3/Ar (2:1 ratio) at 120 W ICP power, 40 W RF Bias power, 7.5 mTorr pressure, and 40°C. The second step is for etching the AlN at an etch rate of 200 nm/min using Cl_2/Ar (4:1 ratio) at 360 W ICP power, 100 W RF Bias power, 5 mTorr pressure, and 40°C. We do not observe a significant change in the surface roughness from the etching, and a sidewall angle close to 90 degrees is achieved due to the combination of physical sputtering and plasma chemical etching. The Cr and HSQ are lastly removed with Cr etchant and buffered oxide etch (BOE), respectively. Fig. 3.2(b) shows a scanning electron microscope (SEM) image of the fabricated AlN waveguide.

Table 3.1: SiON Process Conditions in Oxford 100 PECVD System

LF Power (W)	Pulse Time (s)	HF Power (W)	Pulse Time (s)	Chamb. Press. (mTorr)	Chamb. Temp. (°C)	SiH_4 0 (sccm)	NH_3 0 (sccm)	N_2O 0 (sccm)	N_2 0 (sccm)
160	12	200	8	1900	350	20	70	50	1425

Finally, the waveguides are clad with approximately 3 microns of SION using plasma-enhanced chemical vapor deposition (PECVD) by the parameters shown in Table 3.1, or spin coated with approximately 2 microns of PMMA. The patterned devices designed for grating coupling are top-cladd with either (i) Poly(methyl methacrylate) (PMMA), which has a refractive index of $n_{\text{PMMA}} \approx 1.5$ in the UV to visible wavelengths, or (ii) silicon oxynitride SiO_xN_y (SiON), with a refractive index matched to the underlying sapphire $n_{\text{sapphire}} = 1.76$ by adjusting the composition of oxygen and nitrogen to achieve a refractive index between that of silica (1.45) and silicon nitride (2.1). In the case where the chip is designed for edge coupling SiON cladding is used, and the edges of the chip are mechanically polished back

to the inverse-tapered waveguides. After which any residual resist is stripped, the chips are sonicated, and are then ready for testing.

Chapter 4

Ion Milling

4.1 Optical Interfaces

Repeatable low loss optical coupling into integrated photonics circuits is an essential and ongoing area of research. The coupling into a photonic integrated circuit follows two typical paths, grating or edge coupling, both of which have been mentioned earlier and will be discussed in greater depth later. Just to reiterate, grating couplers suffer from higher insertion loss and spectral selectivity corresponding to the grating design, yet allow for ease of coupling light into waveguides and can be placed anywhere on a photonic chip. The grating dimensions are proportional to the operating wavelength and waveguide/cladding material properties which may lead to additional fabrication challenges for UV and visible regimes [81]. Edge couplers require individual alignment of each fiber connection, and can only be placed along the periphery of the chip, but can have extremely high coupling efficiency without the spectral selectivity. However, the tapered edge couplers require a facet processing step to reduce loss at the taper/edge interface [82–84]. In instances where an etched or polished facet can easily be created, the consideration is cost and time. Certain materials do not easily lend themselves to neither plasma nor traditional facet preparation processes and an alternative procedure is necessary [85, 86]. Lack of a reliable facet preparation method for stressed or easily delaminated films is limiting research into novel waveguide material systems. This research demonstrates a technique to allow for a wide variety of optical interfaces to include stressed or etch resistant

interfaces to be prepared for direct coupling through an ion milled facet.

The research described in this chapter demonstrates direct edge coupling to an AlN waveguide with a highly stressed upper cladding. The stressed cladding is silicon oxynitride (SiON), but could be any deposited film. Traditional facet polishing methods may delaminate the cladding, the waveguide, or both, thus removing the possibility of direct or free space coupling due to scattering losses at the facet/waveguide interface. The worst case scenario is shown in Fig. 4.1, where the top cladding was chipped during the initial polishing step, stripped off and redeposited. During the deposition, the aluminum substrate reacted with the oxygen in the chamber and formed small sapphire crystals, thus making the sample unsalvageable.

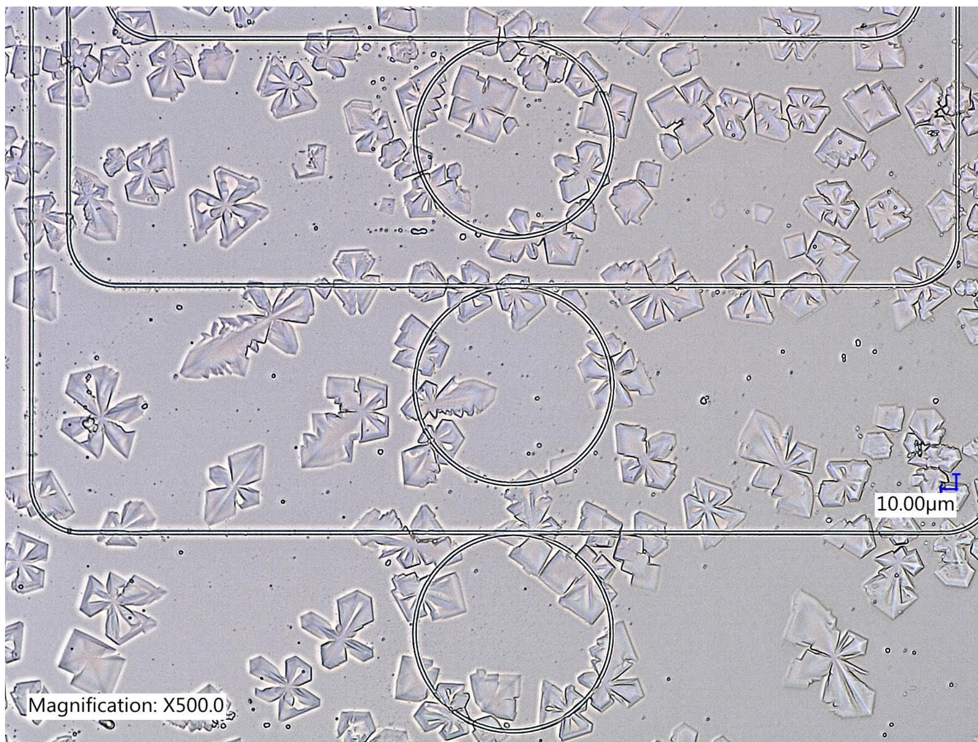

Figure 4.1: AlN nitride optical microscope top view image of a worst case scenario where the cladding chipped during polishing but did not damage the waveguide. Consequently, the top cladding was removed and redeposited. During the second attempt at deposition, crystal regrowth of sapphire substrate appeared, and then the sample became unsalvageable.

These sample preparation problems required the need for another method of preparing the edge facets on these samples so recladding of the devices was not required. Plasma etched facets were unavailable due to the difference in required etch chemistries for the cladding and

host substrate. With these constraints ion milling was considered to produce an optical quality facet in this material platform.

Ion milling is commonly used to create flat surfaces for a variety of metrology applications when traditional polishing techniques would damage the target surface. Ion milling has proved useful in the formation of photonic crystal and nonlinear material waveguides [87–89], but to the best of my knowledge has not been used for polishing edge facets for direct coupling to PICs. This method opens up a whole new realm of possibilities when traditional polishing or facet preparation methods are prohibited.

4.2 Design And Fabrication

The optical circuits to be used for these tests were designed in the program, Klayout, and included multiple resonator dimensions, coupling gaps, and waveguide widths (listed in Table 4.1) with tapered edge couplers terminating in a long uniform width section going to the edge of the chip. This allowed greater coupling tolerance when polishing the last 100 microns of the edge facet. Secondly, this allowed for multiple attempts per sample for ion milling, as the milling was the least time consuming portion of the fabrication. Prior to fabrication simulations were performed to optimize the mode matching of the tapered edge couplers and the UV optical fiber (Nufern SM300) connecting to the facet, see Fig. 4.2, indicating a best case coupling scenario of 60%. More complicated designs could be used in the future to optimally match the edge coupler to the fiber but it was not necessary for the proof of concept demonstration.

These designs were then fabricated (see [66] for specific waveguide fabrication details) in 200 nm of AlN grown on Al_2O_3 substrates. After waveguide fabrication the samples were coated in photoresist for shipping, upon arrival stripped of the photoresist, cleaned, and the low stress SiON upper cladding was deposited using the Oxford 100 at the cornell nanofabrication facility (CNF). Following the deposition of the SiON upper cladding, the samples were mounted and prepared for standard polishing of the edge facets. The standard polishing was performed on an Allied multiprep polisher by sequentially reducing the grit sizes (30 μm to 0.1 μm)

Table 4.1: By varying widths, diameters, and gaps for the AlN microring resonators the authors should be able to extract n_{eff}, loss, and other values for this material.

Waveguide Width	Ring Diameter	Resonator Gap
250 nm	10 μm	50μm
250 nm	10 μm	75μm
250 nm	10 μm	100μm
250 nm	20 μm	50μm
250 nm	20 μm	75μm
250 nm	20 μm	100μm
250 nm	40 μm	50μm
250 nm	40 μm	75μm
250 nm	40 μm	100μm

until the polished facet was within the edge coupler taper region (the taper was left long to allow for uncertainty in polishing), a process that has been successful in prior reports of Si photonics [90]. The quality of the polish is periodically inspected during each step to address delamination, uneven polishing, and progress. The polishing process left a residue of ground material on the PIC surface that was cleaned off by a 1-2 minute soak in Acetone, followed by a rinse of Methanol or Iso-propanol. The AlN on Sapphire chip was expected to show a polished face without facet defects. However, stress in the SiON cladding film lead to facet and waveguide damage during polishing as seen in Fig. 4.4. The result of the standard polishing technique was that neither free space nor fiber coupling solutions were viable to couple with this interface as too much light was scattered away from the waveguide. The damage to the either the facet, waveguide, or cladding could not produce an optical quality facet. In an effort to gather information from the damaged PICs and salvage the samples it was decided to ion mill the damaged facet to produce an acceptable interface between the fiber and chip.

The chips were cleaned in acetone followed by methanol and then mounted with wax on metal chucks for the ion mill. Once mounted the facets were prepared using a JEOL IB-09010CP cross-section polisher and aligned such that 40 μm to 60 μm of the chip edge containing the edge tapers was exposed beyond the beam block for milling. An accelerating bias of 6.5 keV, with 6 to 7 sccm of Ar gas, for 3 hours was sufficient to polish a facet region 1 mm wide to at least 70 μm deep to accommodate a bare Nufern SM300 fiber (125 μm

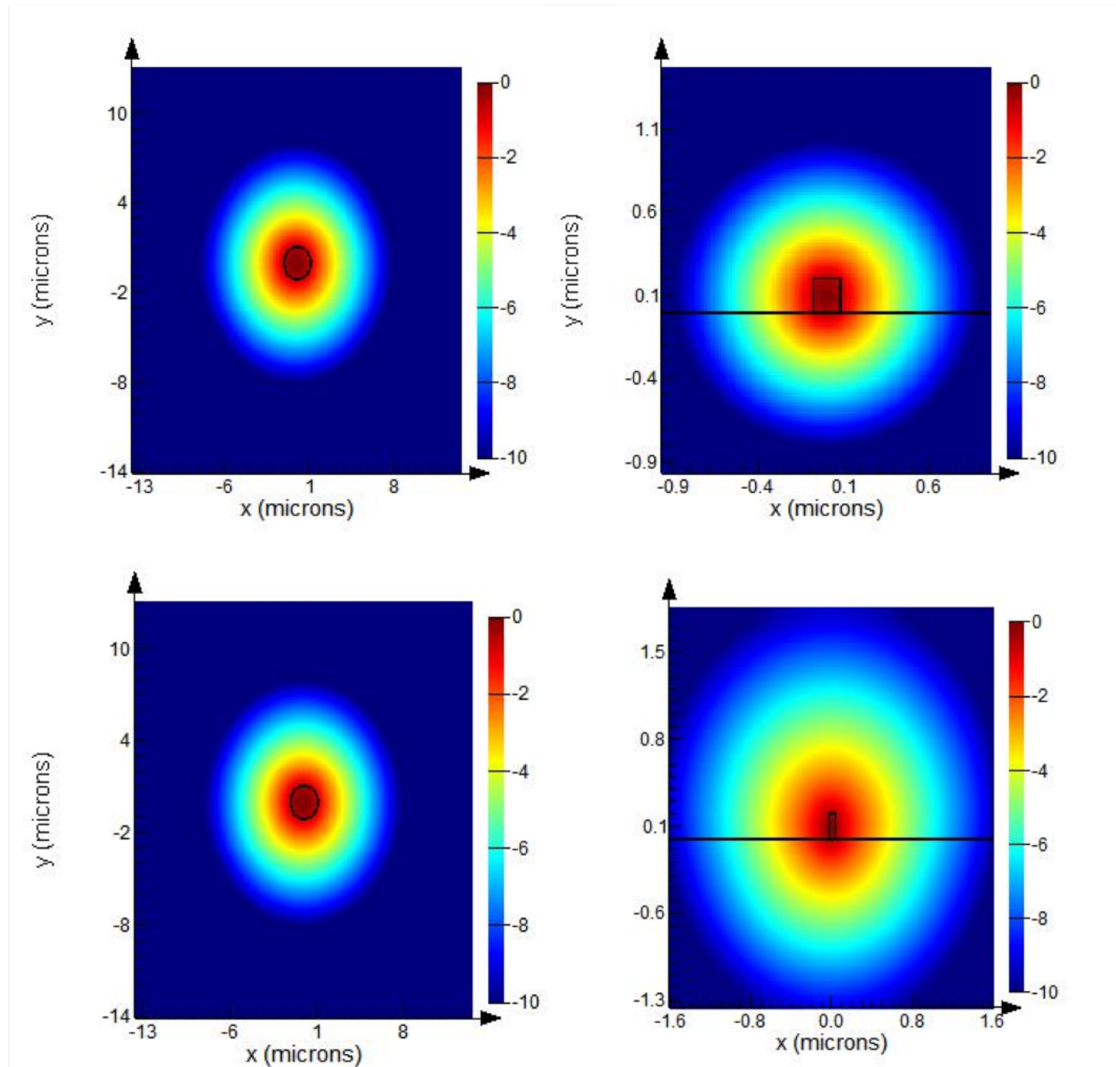

Figure 4.2: Simulated ideal mode profile of the SM300 fiber (top left, bottom left), the untapered edge coupler (top right), and the tapered edge coupler (bottom right). Colormap represents intensity of electric field on log scale (dB).

diameter). After ion milling the chips were removed, soaked in acetone of 1 - 2 minutes to remove mounting wax, cleaned with methanol and iso-propanol, and then inspected on a Keyence microscopy system at 20X to 2000X optical zoom.

When compared to Fig. 4.4 left, Fig. 4.4 right exhibits minimal defects at the waveguide/-facet interface since the ion milling does not place additional pressures on the film/surface interface that may cause delamination, chipping, and cracking. This was a very positive initial result as it gave a reliable path to create optical facets in stressed materials. The real test

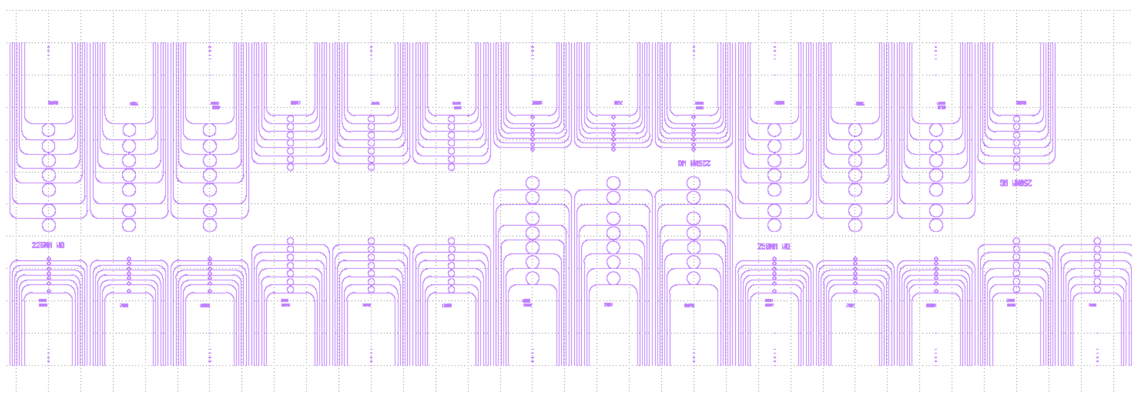

Figure 4.3: Layout of the variety of waveguide structures and dimensions, drawn in Klayout, on chip with tapers aligned to edges for traditional edge polishing for direct fiber coupling.

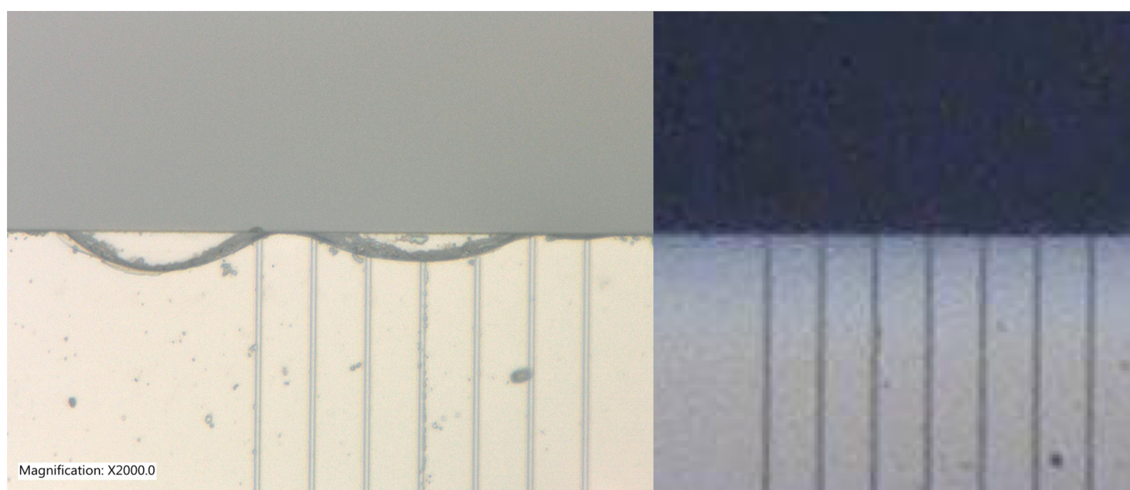

Figure 4.4: (a) 2000X optical micrograph of chipped facet from traditional polishing. Notably the cladding and waveguide often delaminate together witch disallows direct and free space coupling. (b) 2000x micrograph of the same optical chip with an ion milled facet suitable for fiber or freespace coupling.

was to mount the chips to a vacuum chuck to test for optical coupling.

4.3 Experimental Setup and Results

To perform the optical coupling a testbed was constructed which consisted of a frequency doubled continuous wave (CW) Ti:Sapphire (M2 Solstice w ECD-X) for generating 369nm and 390nm. Each respective second harmonic generation (SHG) crystal (369 and 390) in the ECD-X had a tuning of 2nm but needed to be changed and realigned for each of the

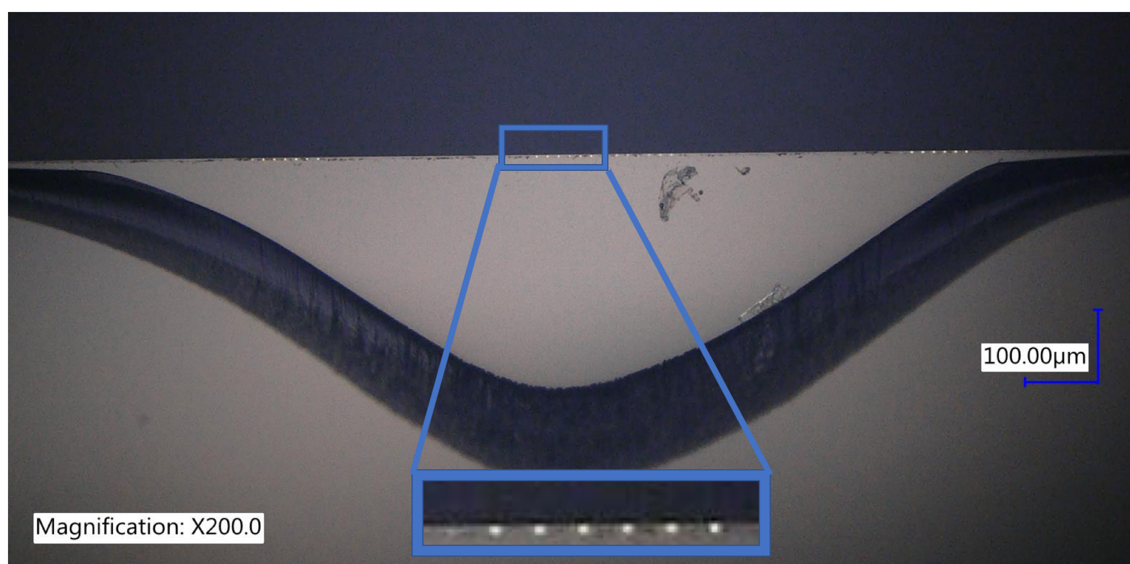

Figure 4.5: 200X optical micrograph of ion milled facet. (Inset) Waveguides array along top edge.

two wavelength regimes. The output of the SHG unit (commonly referred to as a frequency doubling, or doubling unit) was free space coupled into an SM300 optical fiber to allow for ease of monitoring the system. The SM300 fiber connected to a second SM300 fiber which was routed to a 3-axis fiber stage terminating in a cleaved fiber end to couple to the input waveguide of the chip, see Fig 4.6. The exit waveguide was fiber coupled as the input waveguide was and terminated in power meter (Thorlabs S120VC) to monitor coupling. A secondary confirmation of the chips functionality came from a microscope mounted UV sensitive camera (pco Pixelfly USB) above the chip.

The ion milled facet showed very little surface roughness with no chipping and scattering was minimal compared to a the scattering observed in the UV regime from a traditionally polished edge. After coupling was achieved, the first qualification was to measure coupling efficiency to the waveguide. Maximum theoretical coupling efficiency of the AlN waveguide to fiber interface was found to be 0.1% based on the comparisons of the mode field dimensions between the waveguide and fiber, see Fig. 4.2. This low coupling efficiency was not intentional but resulted from the initial standard polishing of the chip where the large amount of damage from the chipping/delamination that the tapered edge couplers were completely damaged/re-

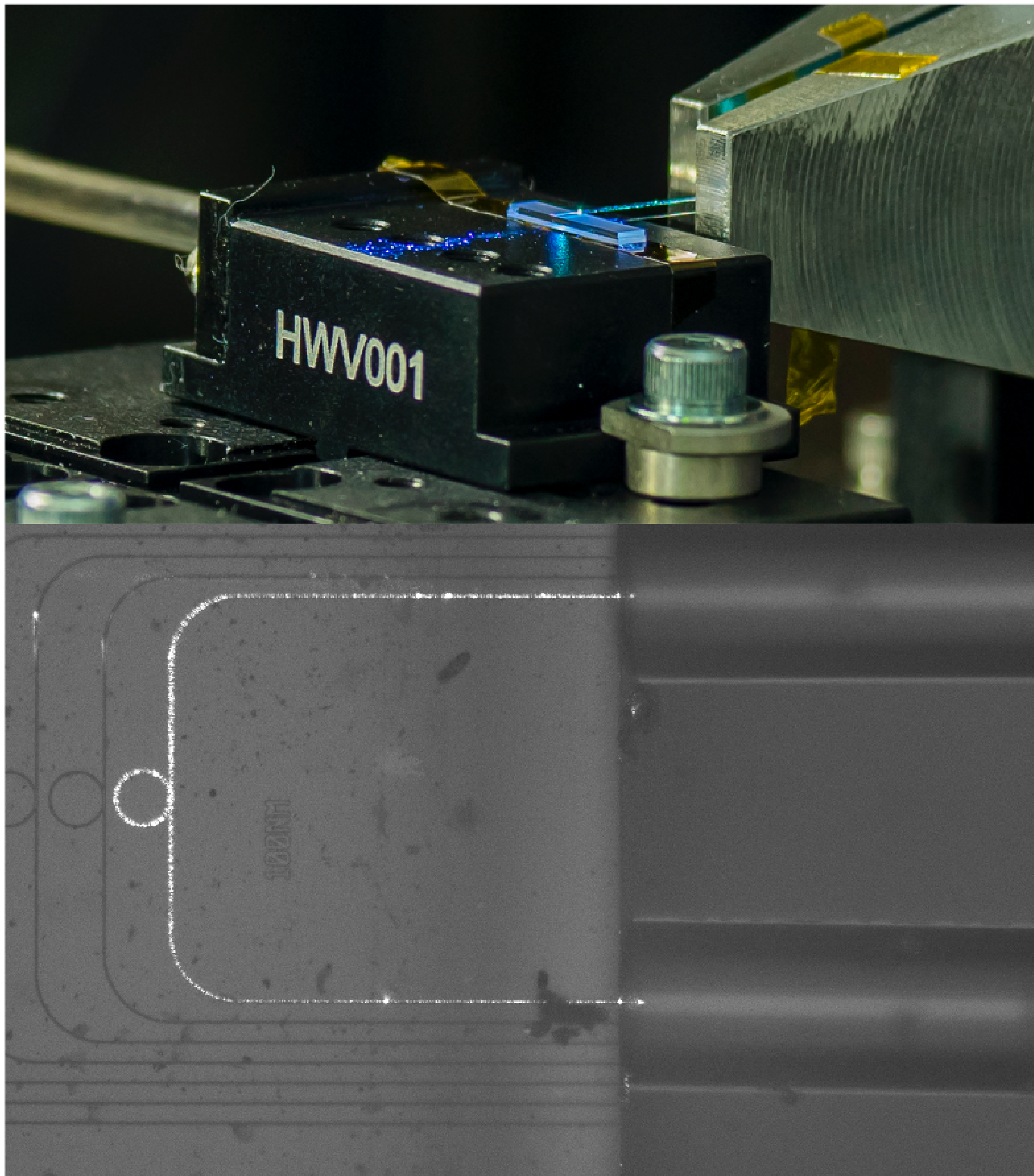

Figure 4.6: (Top)Testbed, showing the vacuum chuck and fibers directly coupled to the AlN chip. The chip appears blue from the incident 369 nm light into the waveguide.(Bottom) Fiber edge coupled AlN microring on resonance.

moved. This meant that the designed adiabatic mode transition region from the mode field of the optical fiber to the waveguide was missing, thus the resulting in low coupling efficiency. This is an easily fixed hurdle though as the initial intent was always to have the adiabatic

edge couplers at the termination points of the waveguides to the chip facets. These couplers exist in the designs and the next set of waveguides will be fabricated with them and polished with the ion mill over the standard technique. Accepting the lower coupling efficiency into the waveguides, the waveguide and ring resonator were easily excited by the input optical mode and Fig. 4.7 clearly demonstrates the coupling between the SM300 fiber and the AlN waveguide.

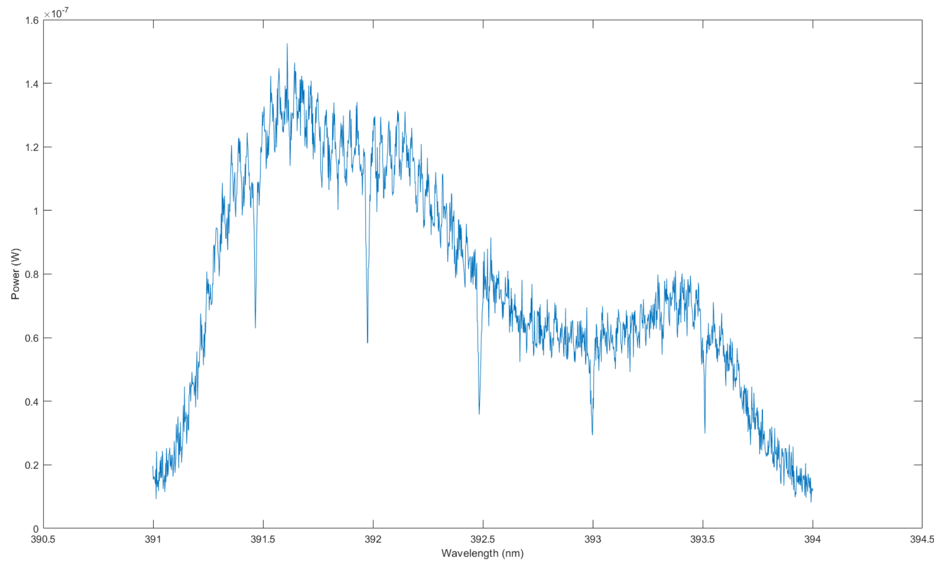

Figure 4.7: Transmission plot from direct fiber-coupling to the AlN PIC after ion milling showing transmission of a scanning laser through the waveguide and ring resonator with the resonances apparent from 391 to 394 nm.

This result was more than optimal since prior to ion milling the coupling to the waveguide could not be achieved and the samples which were normally not salvageable became useful [91]. Additionally, this technique could be used to reclaim any samples that are otherwise lost like Fig.4.5. With proper alignment and masking this process can be used to correct singular defect regions in fabricated devices.

Overall, ion milling provides an additional method for preparing edge facets for edge coupling to PICs beyond the traditional polishing and plasma processes. In situations where the cladding or waveguide may readily delaminate, due to high stress, brittleness, or chemical

sensitivity, ion milling provides a method for direct coupling to a PIC that would otherwise not survive the polishing process. This research has demonstrated the collection of meaningful data from devices that were otherwise deemed unusable due to damage from other polishing means. Ion milling is a consistent and viable processing solution for preparing chip facets for direct coupling, producing facets that rival traditional polishing processes. This method should be expanded to other material systems that are difficult to prepare such as lithium niobate, potassium titanyl phosphate, air clad waveguides, or high stress films [92] that resist traditional facet polishing techniques.

Chapter 5

Experiments

5.1 Experimental Testbed

The construction of three testbeds was concurrent with the fabrication of the aluminum nitride samples. The three testbeds consisted of two nearly identical setups at RIT and AFRL, and one specifically for visible wavelength photonics addressing nitrogen vacancy centers at MIT. The testbeds that were constructed at RIT and AFRL will be further described in this section and were briefly introduced in the last chapter.

The wavelength regions of interest for RIT and AFRL are the ultraviolet (interface with trapped ion quantum memories), and the near infrared (pumping wavelengths of SPDC generated in the telecommunications band). These constraints dictated the required components in each of the testbeds.

The test bed consists of a pump laser to excite the material and test the parameters of the waveguide structures. Tunable continuous wave (CW) and pulsed lasers were incorporated into each testbed, being CW Ti:Sapphire (M2 SolsTis with SHG unit (manually tuned at RIT, electronically tuned at AFRL)) and a pulsed Ti:Sapphire (Coherent Mira/Spectra Physics Mai Tai both with SHG units) respectively. These lasers allowed for the generation of pump wavelengths in the infrared from 700-900 nm and the frequency doubled SHG signals from 350-450 nm. At the AFRL testbed there is the added option to use two optical parametric oscillators as sources of pump light for characterization (Radiantis Inspire HF 390-1700 nm,

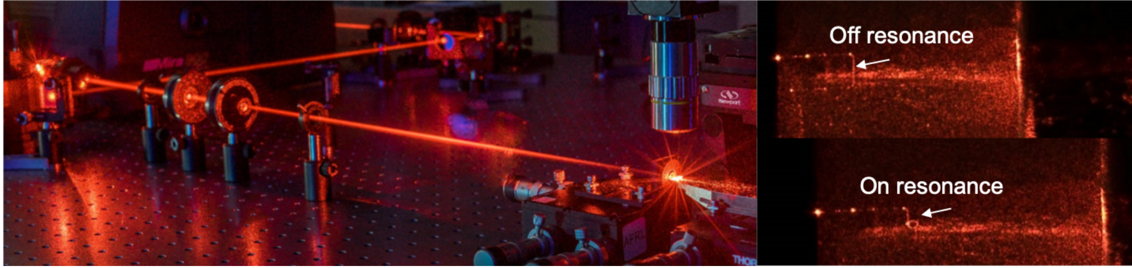

Figure 5.1: ((Left) Experimental for testing the AlN chips in the infrared. The laser beam enters from the right and is sent through beam shaping, polarization rotation, and attenuating optics before an aspheric objective lens and coupling into/out of the chip. (Top right) Wavelength tuned to off resonance for the microring. (Bottom right) Wavelength tuned to resonance of the microring, note the illumination of the microring and the drop in power on the exit waveguide .

and a Chromacity OPO 1000 -1700 nm, and 2400 nm). In both locations there were numerous lasers in the 1400-1700 nm regime for testing waveguides in the telecommunications band. Focusing just on the Ti:Sapphires at the moment, following the laser was a spatial filter to remove residual pump light (532 nm) from the vanadate laser, mirrors to direct the beam to a variable beam expander (Thorlabs BE02-355) for changing the mode field diameter, polarization rotators to change the orientation of the electric field entering the waveguide, and waveplate/polarizing beamsplitter combination to control the optical power level entering the waveguide. Next for the infrared testbed, the beam was directed to a 6 mm focal length aspheric lens for coupling in and out of the waveguide as shown in Fig. 5.1. The output beam was directed via a mirror to an optical power meter (Thorlabs S120VC) where the readings were recorded via a computer as in Fig. 5.2.

The testbed's configuration was altered when working in the ultraviolet to contain the beam path whenever possible for safety reasons. In the free space portion the beam expander needed to be switched to a UV version (Thorlabs BE02-05-B) and a coupling stage was included into the beam path to align and focus the laser light into a fiber optic cable (Nufern SM300). The fiber end that the laser light was being coupled in was left with an FC-APC connector while the other end was cleaved flat to allow for edge coupling to the AlN waveguide. A second fiber was prepared in the same way to couple to the output waveguide and the connectorized end was routed to an optical power meter (Thorlabs S122C) which recorded the values via

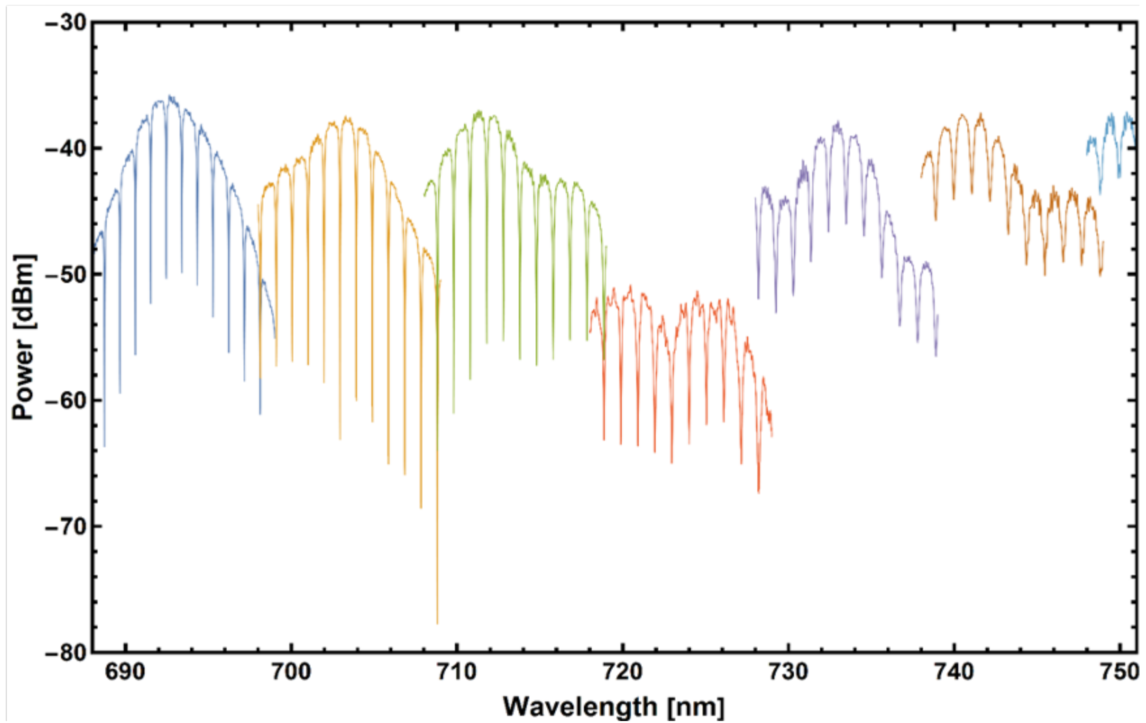

Figure 5.2: Representative plot of the microresonator resonances detected on a power meter as the spectrum from a pulsed Ti:Sapphire laser is tuned from the visible to the infrared.

a computer as in Fig. 5.3. The testbed at MIT was similar to the two described above in construction and operation.

The AlN chip was mounted on a vacuum holder mounted to a 3-axis nano-mechanical stage for fine positioning of the chip to the fibers. Two independent stages with fiber mounts were added to position the cleaved optical fibers to the waveguide ports. The AlN chip on the vacuum mount sat under an optical microscope to aid with coupling alignment into the waveguide and as a visual confirmation of the current resonance conditions separated by the free spectral range during tuning of the pump laser. This condition is met when the input wavelength is an integer multiple of the cavity as in the equation below, thus allowing light to couple into the resonator. Where in the equation below, m is the integer multiple of the cavity, c is the speed of light, n is the index of refraction of the material, and r is the radius of the microring. If this was just a linear cavity the denominator would instead be $2nL$, where L is the length of the cavity. This will be discussed in greater detail in section 4.1.2.

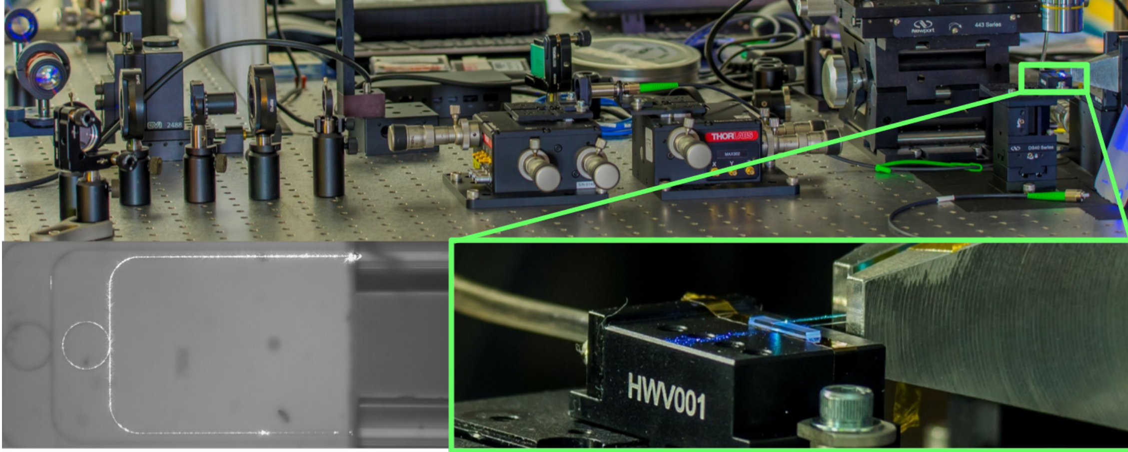

Figure 5.3: ((Top) Experimental for testing the AlN chips in the ultraviolet. The laser beam enters from the right and is sent through beam shaping, polarization rotation, and attenuating optics before entering an optical fiber. (Lower right) The optical fiber (Nufern SM300) is the routed to the chip and butt coupled with the flat cleaved fiber end. (Lower left) Fiber edge coupling to the waveguides at 369.5 nm using Nufern SM300 fiber.

$$FSR = \frac{mc}{2n\pi r} \tag{5.1.1}$$

5.1.1 Coupling Methods to the Photonic Circuits

The devices were designed with two different methods of optical coupling, grating and edge. Grating allows for fast characterization of the devices, no requirement for edge polishing, and full use of the surface of the chip for devices. The drawback with grating couplers is the inherent loss with converting the fiber mode into a waveguide mode, usually resulting in a loss of 3 dB. Edge coupling is extremely efficient at matching the waveguide to fiber mode, thus minimal optical coupling loss. This is at the cost that the edge face of the chip must be polished to an optical grade facet, not always a trivial task. Fig. 5.4 highlights the two coupling methods that were used to couple light into the chip: grating couplers and inverse-tapered edge couplers. Due to the narrow frequency response of grating couplers, two different grating couplers are used for testing components in the visible wavelength from 500 nm to 700 nm wavelength: a green wavelength grating coupler optimized for 500 nm to 600 nm (shown in the top SEM image of Fig. 5.4(a)) and a red wavelength grating coupler optimized for

600 nm to 700 nm (shown in the bottom SEM image of Fig. 5.4(a)). Fig. 5.4(b), (c) show comparisons between the simulated and experimentally measured transmission spectra for the green and red wavelength grating couplers, respectively. The general shape of the experimental grating coupler wavelength response matches well with simulation. The experimental coupling efficiencies are listed in arbitrary units because we do not experimentally mode-match the spatial modes of the grating coupler and collection objective.

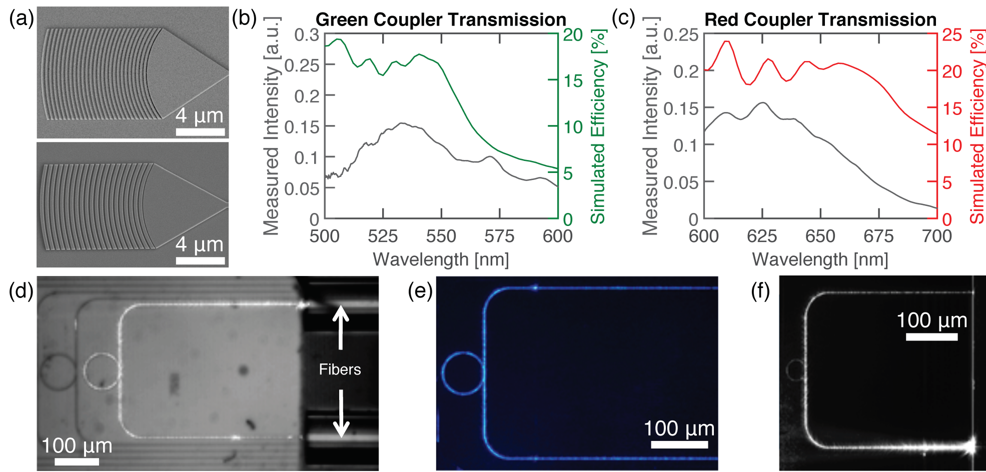

Figure 5.4: (a) SEM images of the grating couplers. First gap of the grating coupler is 60 nm, and the gaps are linearly increasing. Curvatures are set to be matched with mode evolution so that there is no reflection. Top: green spectrum grating coupler. Bottom: red spectrum grating coupler (b) Coupling efficiency vs. wavelength plot of green-spectrum grating coupler optimized for 500 to 600 nm. Black line: measured data. Green line: simulation. (c) Coupling efficiency vs. wavelength plot of red-spectrum grating coupler optimized for 600 to 700 nm. Black line: measured data. Red line: simulation. (d) Fiber edge coupling to the waveguides at 369.5 nm using Nufern SM300 fiber. (e), (f) Single mode operation at 468 and 369.5 nm, respectively.

Both green and red wavelength grating couplers are optimized for transverse electric (TE) polarization, so the simulated coupling efficiencies model the collection of TE polarized light injected into the 450 nm wide by 200 nm tall AlN waveguide on bulk sapphire and scattered by the grating coupler. For the green wavelength grating coupler, the first gap width is 60 nm and the first grating period is 285 nm. Then, the gap width and grating period both linearly increase from 101 nm and 325 nm to 150 nm and 346 nm, respectively (increasing linearly in each period for 17 periods). Finally, the gratings maintain a gap width of 150 nm and grating

period of 346 nm for the remaining 9 periods. In a similar fashion, for the red wavelength grating coupler, the first gap width is 60 nm and the first grating period is 285 nm. Then, the gap width and grating period both linearly increase from 101 nm and 401 nm to 132 nm and 414 nm, respectively (increasing in each period for 10 periods). Finally, the gratings maintain a gap width of 132 nm and grating period of 414 nm for the remaining 10 periods. For both the green and red wavelength grating couplers, the dimensions of each individual grating periods are optimized in order for the spatial mode profile of the diffracted light to be a Gaussian field profile. The grating couplers are also designed to be cladded with PMMA, rather than simple air cladding, in order to increase the out-of-plane coupling efficiency by pulling more of the optical mode away from the underlying sapphire substrate as PMMA has a higher refractive index than air. Both grating couplers are designed for an etch depth of 200 nm in order for ease of fabrication so that the grating couplers and waveguides can be fabricated in the same steps with no additional processing. Therefore, we believe grating couplers with even higher collection efficiency can be achieved with partially etched gratings.

High efficiency optical coupling was achieved with the fiber edge coupling shown in Fig. 5.4(d), with UV fiber (Nufern SM300) and an excitation wavelength of 369.5 nm ($<$ 3 dB/-facet). The second coupling method via free space is shown in Fig. 5.4(e) using aspheric lenses at 468 and 369.5 nm, respectively. In both cases the the inverse-tapered waveguides adiabatically transform and expand the AlN waveguide mode to match the input mode (3 μm) at the chip's edge facet.

5.1.2 Ring Resonators

Ring resonators are extremely versatile devices being used as loss measuring devices, optical filters [29], switches, and as optical cavities for the generation of other frequencies [42]. Starting with the AlN sample platform that we have at hand, one can model the optimized parameters of the device. Shown in Fig. 3.2(c) are the simulated electric field profiles of the AlN waveguide modes for PMMA and SiON cladding for 400 nm and 638 nm wavelengths. The waveguides support a single TE mode for their respective wavelengths. Wrapping these waveguides into

rings produces cavities that meet the FSR requirements described above, and have high quality factors, Qs. The quality factor is a measure of the damping rate of the cavity, dictated by the cavity loss. The higher the Q, the lower the round trip loss in the cavity. Another valuable quantity is the finesse, F, which is the measure of the FSR divided by the cavity full width half maximum bandwidth, $\Delta\nu$. The finesse quantifies the field enhancement in the cavity, an important number for nonlinear processes which require large field strength.

$$Q = \frac{2\pi n_g}{\lambda\alpha} \tag{5.1.2}$$

$$F = \frac{FSR}{\Delta\nu} \tag{5.1.3}$$

The ring resonators were measured for their loss, FSR, and quality factors which are summarized in Fig. 5.6. Shown in Fig. 5.6(b) is the response at 369.5 nm of the 40 μm radius ring resonator around resonance; a Lorentzian fit indicates a Q of $>$24,000, a record for an integrated ring resonator in the UV. In Fig. 5.5 3 adjacent resonances are shown to confirm the FSR of the cavity to be 350 pm. It should be noted that the relative height differences of the peaks is not due to the performance of the resonator but due to the drop in efficiency of the resonant laser doubler as it is operated past its optimal tuning range. Secondly, once the Lorentzian fit was properly optimized the 369.5 nm true peak value was found to be above 24,000. Since the resonance is very under-coupled, the ring resonance cannot be measured directly through an access bus waveguide in this case. Rather, the resonance is measured from light scattering from the ring and into an objective lens above the resonator which is detected using an UV sensitive camera. Hence, the data show a resonance peak rather than the expected dip when measured on the thru port. Fig. 5.6(c) shows the quality factors of 40 μm radius ring resonators measured using an optical spectrum analyzer (OSA) for wavelengths spanning from 380 nm to 480 nm, along with the quality factors at 369.5 nm using both a frequency doubled pulsed Ti:Sapphire laser (Spectra-Physics Mai Tai) and a CW tunable Ti:Sapphire laser (M Squared SolsTiS). If we assume that the propagation loss is dominated by the sidewall scattering loss and linear absorption loss of the material, then we can estimate the propagation

loss using the following equation for calculating the loss rate α given the resonator Q, where n_g is the group index [93–97]:

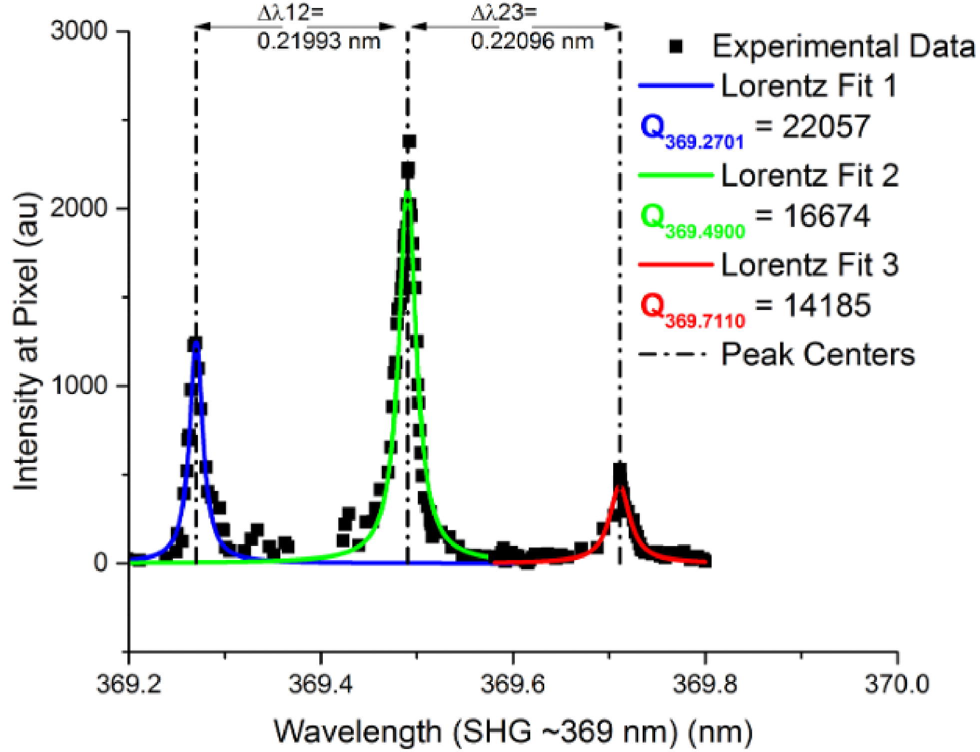

Figure 5.5: Transmission spectrum of the 369 nm resonance showing 3 peaks to confirm the microresonator FSR of 350 pm.

Then, the loss can be calculated by:

$$\text{loss} = 10 \log_{10} \left(e^{-\alpha}\right) \tag{5.1.4}$$

To calculate the loss in units of dB/cm, λ in Eq. 5.1.2 should be in units of cm. Thus, the Q of >24,000 at 369.5 nm wavelength corresponds to a propagation loss of 75 dB/cm, where we measure the n_g to be 2.45 experimentally from the Free-Spectral-Range (FSR) of the ring. This propagation, though large is significantly lower (75 dB/cm vs. 800 dB/cm) than previously reported in the literature [98].

Moving to the visible wavelength regime, Fig. 5.6(d) shows the frequency response of a 50 μm radius ring resonator around resonance in the red. We probe the 50 μm radius ring

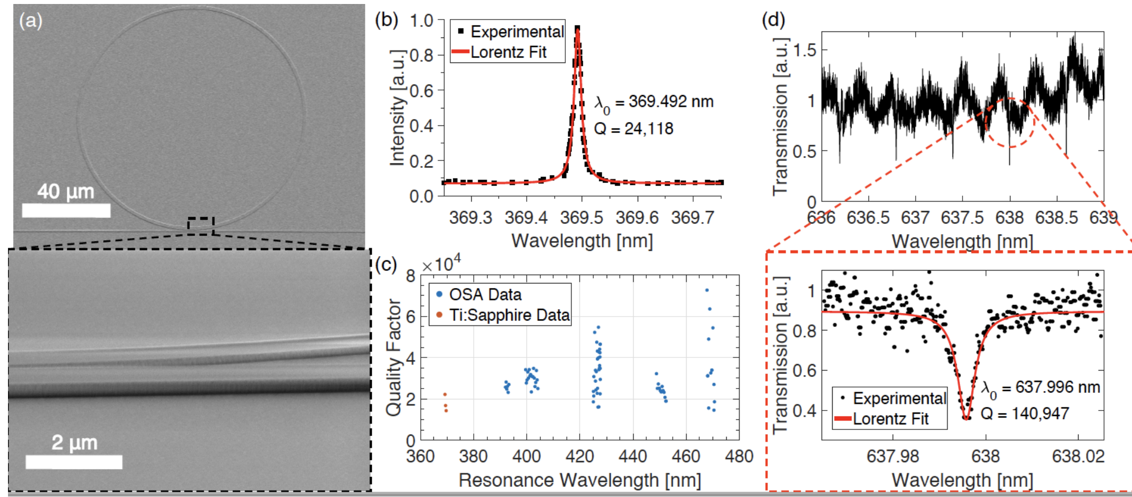

Figure 5.6: (a) SEM of the ring resonator. Inset shows a close up of the ring resonator. The gap between the waveguide and the ring is 300 nm for the undercoupling regime, which was used to verify the unloaded Q. (b) Frequency response at 369.5 nm of the ring resonator around resonance. The Lorentzian fitting shows a Q of >24,000. (c) Quality factors of 40 μm radius ring resonators measured using an optical spectrum analyzer (OSA) for wavelengths spanning from 380 nm to 480 nm, along with the quality factors at 369.5 nm wavelength using both frequency doubled pulsed and continuous-wave (CW) TI:Sapphire lasers. (d) Wavelength response of the ring resonator around resonance. The Lorentzian fitting shows a Q of >140,000. Inset shows a zoom-in of the wavelength response.

with an evanescently coupled access waveguide. The Lorentzian fitting shows a loaded Q of >140,000 at 638 nm. In order to obtain the intrinsic Q of the ring resonator, we can use the following [93–97]:

$$Q_i = \frac{2Q_l}{1 \pm \sqrt{T_0}} \tag{5.1.5}$$

where Q_i is the intrinsic Q, Q_l is the loaded Q, T_0 is the normalized transmitted power at the resonance wavelength, and the + and − signs correspond to under- and over-coupled regimes, respectively. Since the ring resonator is operating in the undercoupled regime, we find the intrinsic Q to be >170,000, which corresponds to a propagation loss of 4.9 dB/cm.

Analyzing these individual results from the devices, the next task was to measure a range of devices over different wavelength regimes to gain knowledge on the material system. These results will be crucial to the next stage of nonlinear photon generation. This began with the

waveguide devices that were designed for the the visible to the infrared using the infrared testbed described previously. The results shown in Fig. 5.7 give valuable information about the devices performance. As the wavelength increases the FSR increases since a given resonator can support less modes of a longer wavelength. Whereas, the Q drops for two reasons, (i) the device is starting to operate away from designed performance (hence increased loss) and (ii) the wavelength is increasing with a given cavity dimension. From the Q, the group index can be extracted and is relatively flat, showing good mode matching across the device. Finally, knowing the group indices, the allowed modal indices of two lower energy photon modes can be plotted that conserve phase matching (energy and momentum). These allowed indices are shaded in pink, and show that the process of SPDC and SFWM can occur in this device over a fairly wide range.

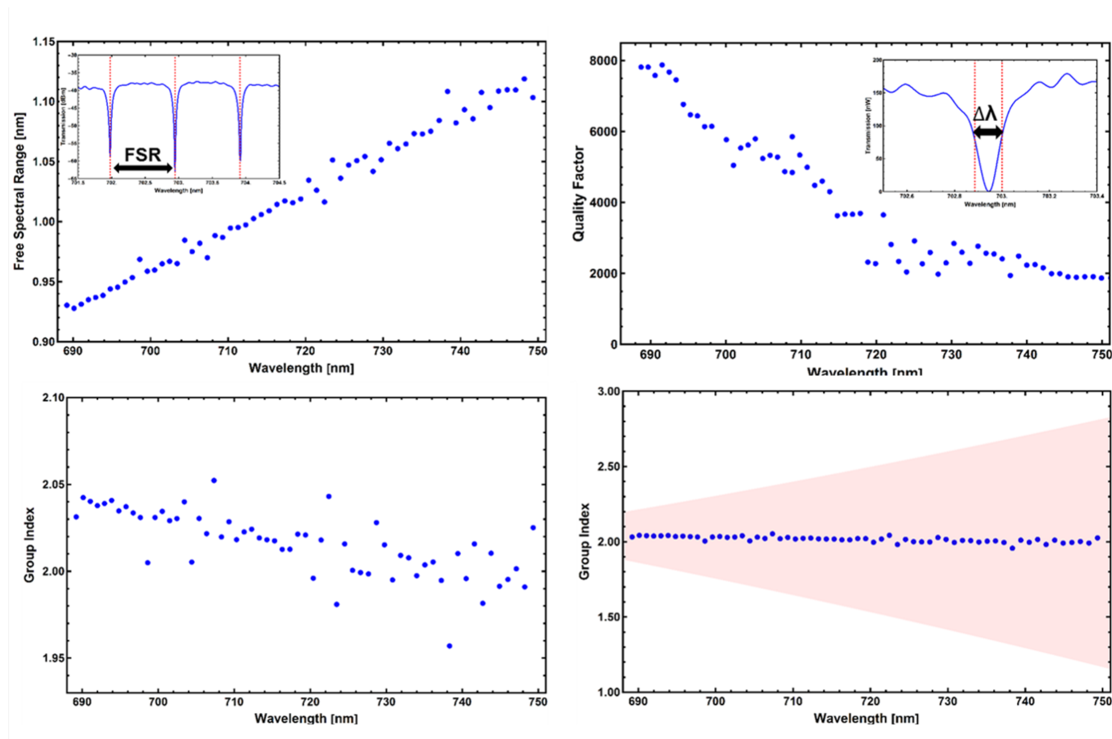

Figure 5.7: Characterization of the microresonators in the visible to infrared. (Top left) Free spectral range, (Top right) Quality factor, (Bottom left) Group index, and (Bottom right) Pink region is the range of index matched group indices that will result in photon generation.

The next task was to reconfigure the testbed and characterize the devices designed for

the UV to visible. Switching to the other side of the spectrum, the loss is expected to be much higher due to scattering from surface roughness (Rayleigh scattering) and material loss (absorption from defects) present in the samples. There were expected trends to be the similar between the two data sets such as the increase of FSR and decrease of the Q with increased wavelength. Interesting with the Q in this particular dataset the peak appears around 425 nm, and this could be due to a number of things. At that wavelength the defects are starting to cause less absorption, the scattering is dropping, and the material may have been slightly thicker when processed for the waveguides leaving the guides multimode on the blue side, and sub-singlemode on the red side. This could account for the dips. Overall though, removing the outliers, the Q is fairly flat meaning a consistent propagation loss in the waveguides. This means though that the group index must increase which is reflected in the data. The result from this expected effect is that the range of group indices which allow for phase matching will be more constrained. This is clearly reflected in the pink overlay in Fig. 5.8. The positive is that the possible phase matching region exists, and therefore the device can function for SPDC and SFWM.

The missing data region was right at 369 nm, where the device would need to function to interface with ytterbium trapped ion quantum memories. The expectation with the previously measured data would be that the devices would follow the same trend 20 to 30 nms lower in wavelength but this hypothesis needed to be confirmed. To accomplish this measurement a number of steps needed to be accomplished. First, the CW Ti:Sapphire needed to be used to obtain the fine step size needed to resolve the resonances with only an FSR of 350 pm. Any of the other lasers at hand, when coupled with a measurement devices, such as an optical spectrum analyzer (OSA) would have only given a few data points per resonance. The resonant doubler needed to be precisely tuned to peak at 369.5 nm since the long SHG crystal gives high doubling power but at a given angle the optical bandwidth is around 2 nm. This configuration gives an optical bandwidth of 1 nm at the SHG wavelength, enough to capture 3 resonances, as shown before in Fig. 5.5. The last piece was added control of the laser tuning and for image processing of the resonance as each FSR was excited. The result from these optimizations to

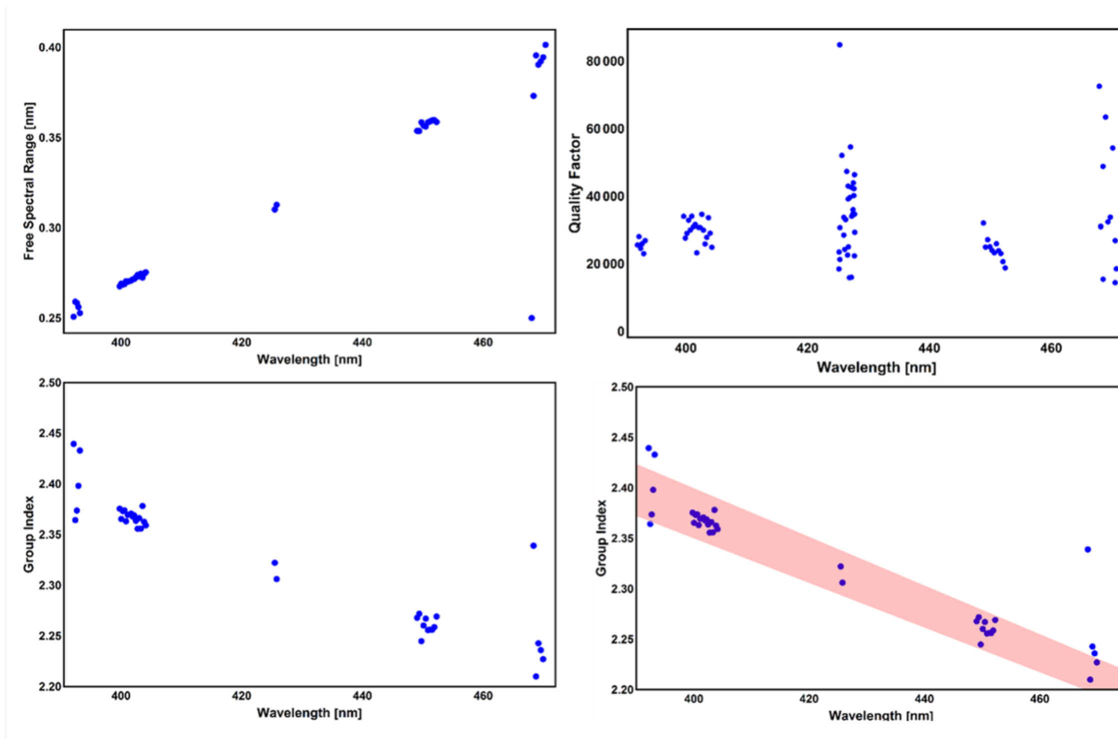

Figure 5.8: Characterization of the microresonators in the ultraviolet to the visible. (Top left) Free spectral range, (Top right) Quality factor, (Bottom left) Group index, and (Bottom right) Pink region is the range of index matched group indices that will result in photon generation.

the system was measurements at 369 nm that matched the prior trends in the collected data shown in 5.9, confirming the device was functioning as designed. After these measurements were completed, the doubler was upgraded to have automatic tuning of 369 $\pm$ 25 nm allowing a quicker turn around on sample measurements.

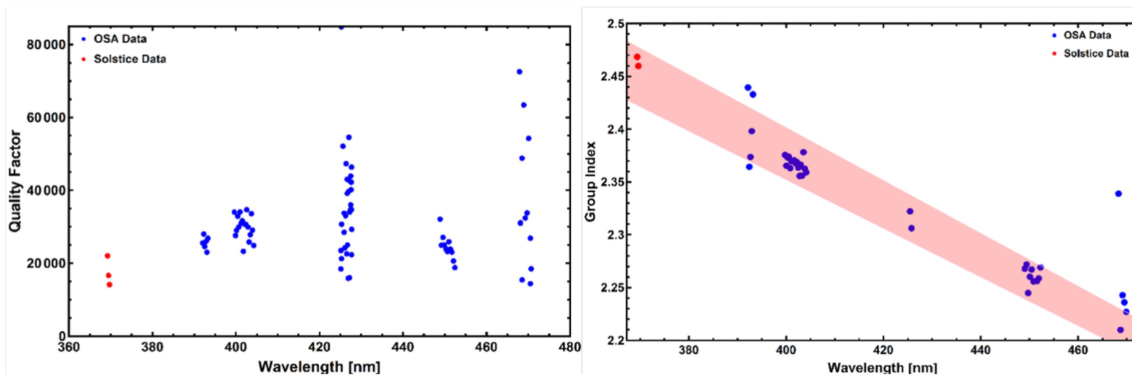

Figure 5.9: Q and Group index plots with the added data at 369 nm. The trend for the device held true down to 369 nm.

The results of the characterization data proved that the devices were capable of obtaining phase matching conditions with a given set of pump wavelengths to create other frequencies. This was extremely important to confirm as this proves the viability of generating bi/entangled photon pairs in these materials. To confirm this was in-fact experimentally possible the devices were tested for their nonlinear response. In this configuration the pulsed Ti:Sapphire laser (Coherent Mira) with a wavelength around 795 nm, a pulse width of 100 fs, a repetition rate of 80 MHz, and an average power attenuated down to 10's of mWs was sent via free space into an aspheric lens for coupling and then to the input port of the AlN waveguides. The AlN waveguides which were tested were designed for singlemode operation at an incident wavelength of 800 nm. The pulsed Ti:Sapphire laser excited the waveguides and generated a visible SHG signal at 397.5 nm, a very pleasant violet color. This waveguide being singlemode for 795 nm was multimode at 397.5 nm, allowing 3 modes of the SHG to exist. Consequently so, the waveguide was extremely lossy for this wavelength with most of the SHG signal scattering out of the waveguide. Even with this added loss at the SHG wavelength there was a measurable signal level that was collected in an optical fiber from the exit waveguide and was sent to a spectrometer (Horriba) with the spectrum plotted against the fundamental in Fig. 5.10. In the figure the resonances are visible in the fundamental signal (red trace) and barely visible in the SHG signal (blue trace). This means that the phase matching was mostly happening in the waveguide and not in the ring. The width of the SHG signal is narrower than the fundamental due to the self limiting nature of these nonlinear processes, where a field that is not strong enough does not contribute to the resulting second harmonic field. Hence, the wings of the fundamental signal are trimmed in the SHG signal.

The observation of the SHG signal was an important milestone as it proves phase matching exists in the device and allows for the generation of other frequencies. Since these nonlinear processes are reversible, sending in a signal at 397.5 nm would produce an entangled pair of photons at 795 nm. In this configuration the waveguide would be multimode for the pump wavelength (which is robust to the loss due to an plethora of photons in the laser beam) and singlemode for the wavelength of interest (the bi/entangled pair) allowing low loss propagation

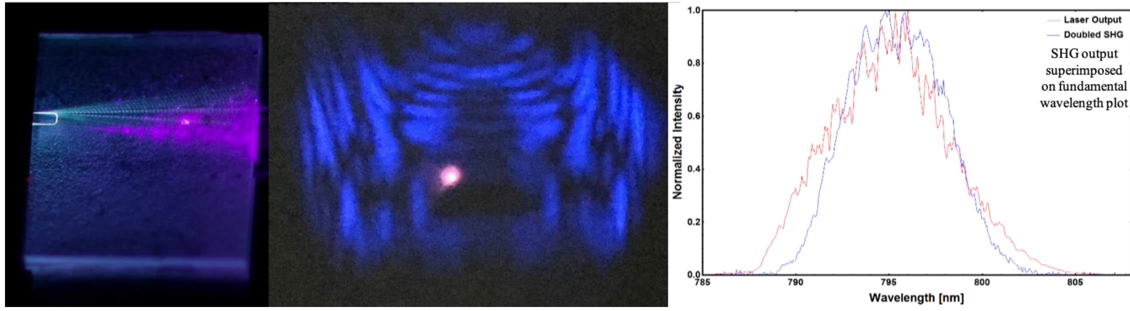

Figure 5.10: ((Left) Image showing the waveguide producing violet light from and input infrared pump laser. (Middle) Far field image of the output mode, showing the center mode which contains the fundamental and the SHG, and the higher order SHG modes that exist in the waveguide. (Right) Spectral plot of the fundamental pulsed pump (Coherent Mira) with the measured SHG output superimposed (Horriba spectrometer).

and strong confinement in the waveguide. These photon pairs would be created by SPDC as would be the case here since SHG was the defining parent process, but this does not rule out that there was also the generation of photon pairs at 795 nm $\pm$ nFSRs (where n is an integer) from the process of SFWM. With the group index so flat, the field overlap of the pump, signal, idler close to identical since they are all roughly the same wavelength, and singlemode in the same waveguide it is very likely that SFWM did occur. Unfortunately at the time, the correct filters to separate the pump wavelength (mW power) from the entangled photon pairs (fW power) only separated by 1 nm were not available to give the required 130 dB of filtering. The components required to perform this filtering have arrived and will be utilized for a future set of experiments.

Chapter 6

Foundry Level Fabrication

6.1 Transitioning from University to Foundry

The quantum field for the last couple decades produced world-class proof-of-concept demonstrations validating theory and pushed hard on the experimental research but were always limited by engineering challenges that came with scaling the systems [99, 100] . These engineering challenges have been a real hurdle, limiting the development of quantum technologies to very specialized, low volume production facilities, whether they be academia, government, or industry. In the last 3 to 5 years the engineering challenges have begun to be solved making a surge of research possible with these newly able to be scaled quantum systems. There has been such momentum that companies or portions of companies have become centered around quantum technologies such as superconducting [101, 102], trapped ions [103], and photon [104] based qubits. This is a groundbreaking advance for the field, though there are still challenges to overcome. Particularly, for many of the technologies, the components are still produced in low volume, and this is where transitioning to a high volume foundry level production facility is crucial to accelerate the fields growth. When one looks at the technology from a fundamental level, the need is for qubits, and lots of identical/nearly identical qubits. This is an impossible request to ask for a university facility, but the everyday output of a commercial foundry.

Looking at the silicon photonics community, foundries have existed across the globe with devices have being fabricated, packaged, and sold as commercial products for years. The fun-

damental difference with the quantum photonics community is the need for extrememly low propagation loss devices as many of the required devices have conventional telecommunication analogues. When one is dealing with low to single photon level signal levels, the typical losses of conventional integrated photonics is an immediate crutch [105]. To overcome this limitation over the last 3 years there has been a two pronged approach with this research which will be discussed. First, team with a commercial foundry, American Institute for Manufacturing Photonics (AIM Photonics), to reduce the propagation loss of silicon and silicon nitride waveguides in a commercial foundry. While concurrently pairing with a research foundry, College of Nanoscale Science and Engineering (CNSE) to introduce ultrawide-bandgap materials into a 300 mm foundry line.

6.2 Wide-bandgap Materials in a Foundry

Capitalizing on the existing CMOS foundry capabilities has allowed a rapid acceleration in the production of complex integrated photonic circuits. This is due to the fact that two excellent photonic materials, silicon (1.14 eV, transparency to 1100 nm), and silicon nitride (3.5 eV, transparency is poor below 400 nm) already exist in the CMOS foundry lines. The foundry can use the same cleanroom, tools, and processes which are used to make conventional CMOS for the fabrication of integrated photonics. This is the stepping point which allowed the field to begin, grow, and now flourish. Though, simply staying with this technology and producing photonic devices from a standard CMOS line will not get you the best devices, but it will produce functioning devices optimize from. The notable factors to optimize are smoother etches and higher crystallinity of the waveguides to reduce scattering loss, removal of defects or dopants from the waveguide to reduce absorption, and careful placement of higher index or absorbing material which can change the field confinement of the waveguide. After carefully considering all these parameters that needed to be altered, we decided to partner with AIM Photonics to push the foundry level fabrication to a point where one could fabricate world class integrated photonics for quantum applications.

The partnership started around three years ago to address the need to create quantum

photonic devices that were not feasible to fabricate with enough repeatability in a university cleanroom. The evolution of devices, specifically a photon source in this case, is shown in Fig. 6.1, show where both an increase in repeatability and circuit complex is apparent. At this point though, the overall functionality of the circuit was more of a concern and the typical optical propagation loss of the waveguides (Si 3-4 dB/cm, SiN 4 dB/cm) was just a limitation on the propagation distance of the photon. Thus, these devices still proved that quantum devices could be created in a commercial foundry [106].

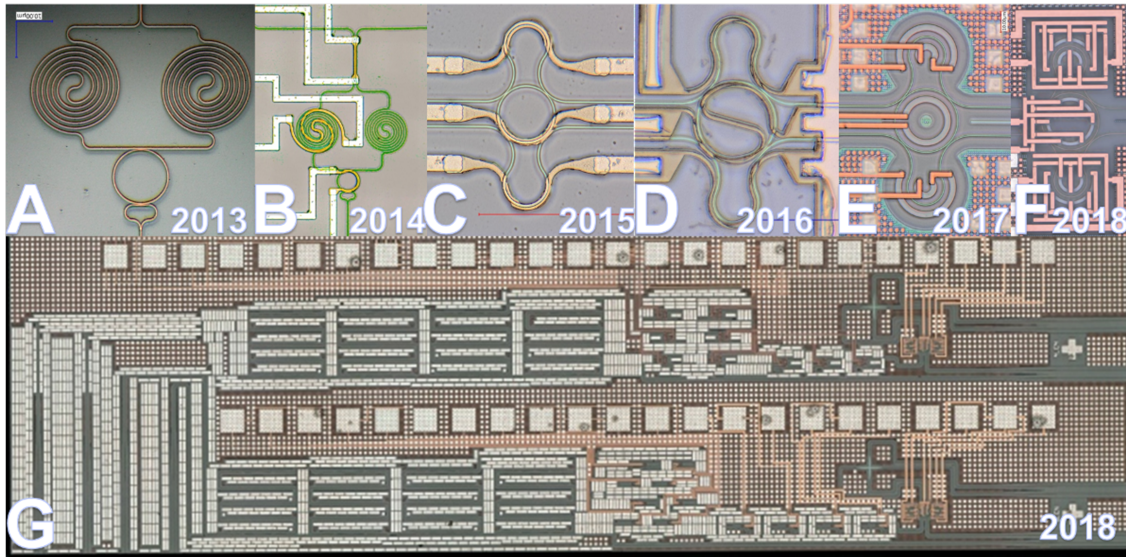

Figure 6.1: (a) and (b) Photons sources fabricated at CNF. (c) and (d) Photon sources fabricated at a small company. (e-g) Photon sources fabricated at the AIM Photonics foundry.

Once this threshold was reached, from then (2 years ago) to present the focus has been with the foundry to iterate on the process for creating the photonics with the goal of reducing the propagation loss of the waveguides to record levels. Since this is a commercial foundry, we are not allowed in for the fabrication and numerous fabrication aspects are proprietary, but our part was to throughly model and simulate the structures, analyze and test the devices, and verify structures as the fabrication process was changed. This meant full characterization of the devices for coupling and propagation loss, feature sizes (designed vs. fabricated), and device uniformity performance across the 300 mm wafer. The individual aspects of the data are not important for this discussion, but the important point is this crucial fast feedback to

the foundry was the key to success. Through these combined efforts the propagation loss of the waveguides has reached record low loss (Si 0.4 dB/cm, SiN 0.2 dB/cm) and continues to be reduced. The second important point is that the silicon nitride is now in a low loss regime where it can be used for quantum photonics in the visible wavelength regime exploiting it to the full potential of its wide bandgap [107]. Lastly, this level of collaboration has allowed the fabrication of one of the most complex 300 mm quantum photonic wafers from a commercial foundry as shown in Fig. 6.2. The devices, spanning both visible and infrared wavelengths, covers the entire necessity of functions, (i) production of the photons, (ii) manipulation and processing of the photons, and (iii) detection and analysis of the photons.

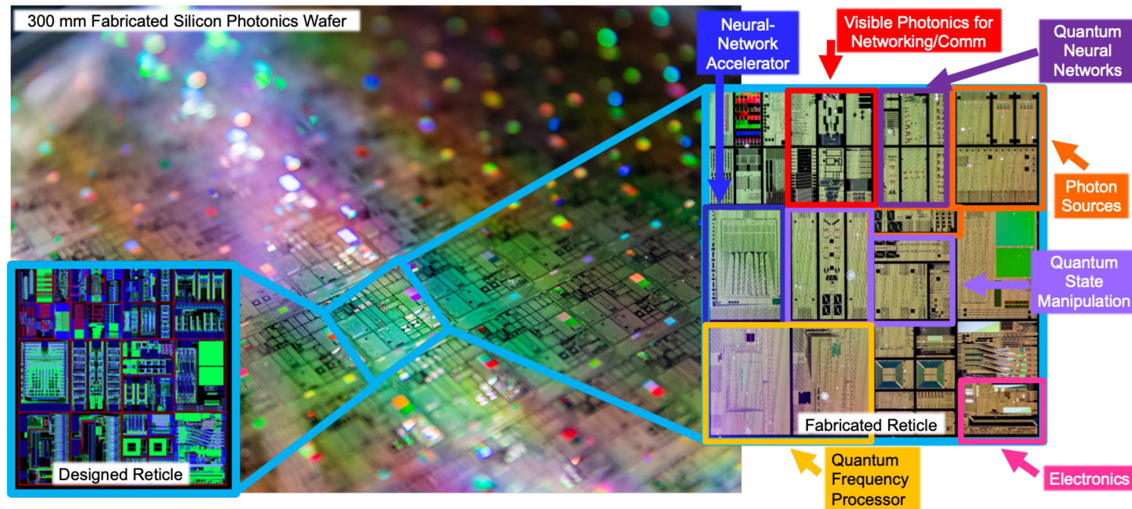

Figure 6.2: Photograph of the 300 mm quantum photonics wafer. (left inset) Designed reticle comprising of 12 chips, and 44 subcells. (righ inset) Photograph of one of the 65 fabricated reticles on the 300 mm wafer.

6.3 Ultrawide-bandgap Materials in a Foundry

The need for a versatile integrated photonics platform is well addressed by silicon and silicon nitride but is still lacking in some key capabilities. These include the electro-optic effect (requires a non-centrosymmetric crystal), operation below 400 nm, and access to a second order nonlinearity, $\chi^{(2)}$. Aluminum nitride satisfies all of these criteria and exists in commercial electronic foundries [108] for high power electronics. The hurdle is that quality of material

does not meet the standards for integrated photonics. The existing material is not of optical quality, but it does mean the material is compatible with a standard CMOS foundry process, a huge hurdle to have overcome. This lead to the relatively new collaboration with CNSE on how to incorporate optical quality AlN into a 300 mm foundry line.

The first step was to design structures and a corresponding layout that the photolithography masks could be produced from as shown in Fig. 6.3. The design rules were that features needed to be greater than 200 nm, and there are only two metal layers. With these rules in mind, this meant that the structures would be for infrared wavelengths, a plus since the loss in AlN is really low and the scattering due to Rayleigh is minimal. The metal layers are a beneficial bonus for creating electrodes and exploiting the electro-optic effect to produce index changes for modulation.

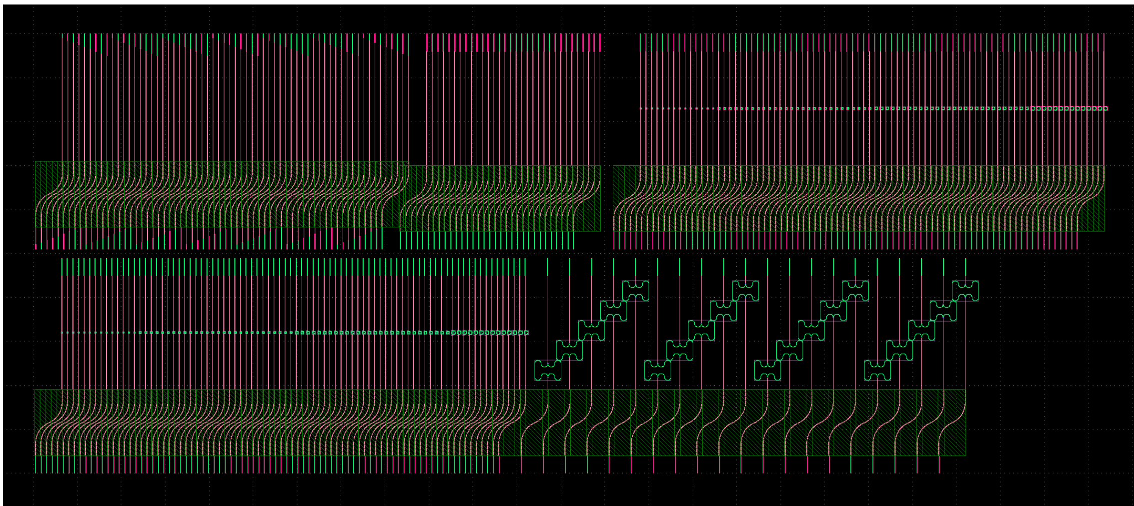

Figure 6.3: Designed AlN structures to be fabricated through both the typical and damascene fabrication methods at CNSE.

The design consists of arrays of ring resonators for optical filtering and the generation of bi/entangled photon states which will directly interface with the telecommunications wavelength fiber networks. The second set of devices on the lower right side are Mach-Zehnder modulators for the modulation of incoming optical signals. These particular electrodes are designed for low speed proof-of-concept devices, with high speed modulation as a goal for future research.

The waveguides will be fabricated at CNSE with two different processes, traditional RIE (as described in chapter 3) and damascene [109]. The damascene process uses pre-existing structures to define where the deposited material will remain after growth and polishing of each subsequent deposited layer. In both cases, the AlN will be deposited by atomic layer deposition on a silicon handle wafer which has 2 μm of thermal oxide grown on it. The traditional process will pattern the ALD AlN and use photolithography and RIE to define the waveguides before an oxide upper cladding is deposited. These waveguides post RIE but before deposition of the upper cladding are shown in Fig. 6.4.

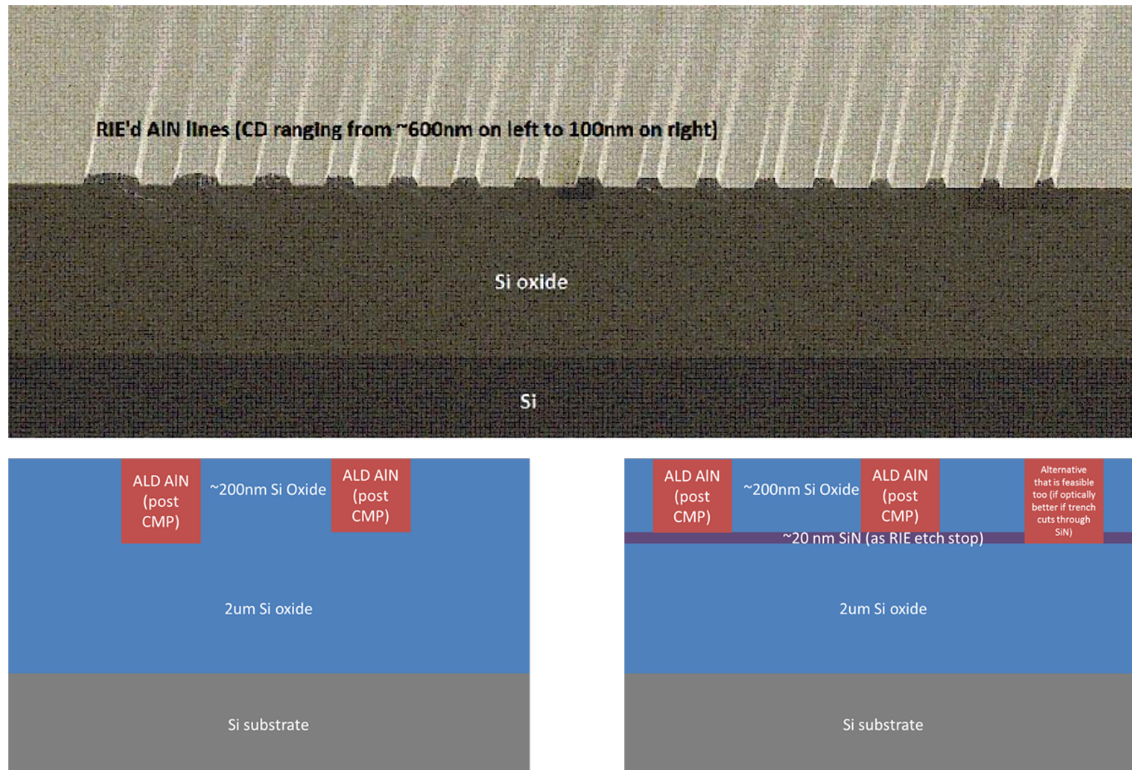

Figure 6.4: (Top) SEM image of atomic layer deposited (ALD) AlN on SiO_2 and then reactive ion etched to create the waveguides. (Bottom left) Damascene created optical waveguides. (Bottom right) Damascene optical waveguide with an etch stop of SiN to aid in trench fabrication.

Turning now to the damascene processing of the AlN, there are two fabrication scenarios. The first is that the thermal oxide is patterned via photolithography, then etched to produce the waveguide trenches, ALD AlN is deposited, the surface is chemical-mechanical polished

(CMP) to flatten to the thermal oxide layer leaving only the AlN in the trenches, and then deposit the oxide upper cladding. The second scenario deposits a layer of SiN as an etch stop on the thermal oxide, then deposits more oxide in which to define the waveguide trenches, with the rest of the process the same as previously described. The damascene process provides a reliable and repeatable method for creating waveguides in tough to etch materials such as AlN. This method also provides a method of inserting photonic quality AlN directly in the CMOS line.

Foundries now have reached the low material loss regime and will quickly expand in the production of quantum and quantum enabled devices. New materials which existed in university or specialized cleanrooms are beginning to be considered necessary in large scale production lines, opening up avenues for unconventional devices to be fabricated on a commercial scale. These unconventional materials will also serve as the intermediary material linking heterogeneous photonic and quantum technologies together, and one day transitioning to combining all the required components into one material system.

Chapter 7

Broadband Photon Source

7.1 Broadband Photon Source

Bright sources of bi/entangled photons pairs are immensely useful for any number of different experiments in any quantum optics laboratory [110–112]. In many cases, it is ideal to have the source of photons as a separate entity from the experiment to be accomplished. Specifically with quantum integrated photonic circuits, the source of photons is not always included on the chip, or an on-chip source may not be bright enough (high enough photon flux) to compensate for the optical loss. These variables included with the general usefulness of a bright photon emitter is the reason this source was constructed.

$$\vec{P}(t) = \varepsilon_0[\chi^{(1)}\vec{E}(t) + \chi^{(2)}\vec{E}^2(t) + \chi^{(3)}\vec{E}^3(t) + \chi^{(4)}\vec{E}^4(t) + ...] \tag{7.1.1}$$

Stepping back to the fundamental concept of pair generation there are a number of variables that need to be considered in the construction of a bright source. First, one would like to select a material with a second order nonlinearity, $\chi^{(2)}$, as it is the lowest order, highest efficiency nonlinear term. This then puts a constraint on the materials since the crystal must be non-centrosymmetric to have the $\chi^{(2)}$ term. Secondly, the second order term relies on the $\vec{E}^2(t)$ of the pump field. Therefore, a higher field strength, the higher the probability of generation. To increase the field strength and material interaction length the most straightforward method is

to confine the light to an optical waveguide. Lastly, picking a material with an accessible high nonlinear coefficient which may require using a material that is periodically poled. Periodic poling is the process where alternating domains are introduced into a crystal to allow for phase matching (energy and momentum conservation) to occur [113–115]. This method is often used when a strong nonlinear axis in a material cannot achieve phase matching via the materials inherent birefringence or any other means [116, 117].

Table 7.1: Here, ϕ is approximately 0.335 and $\Delta n_g = |n_{g1} - n_{g2}|$.

Table of generation rate formulas for different types of SPDC	
Type	Formula
Type-0/I, SM	$\sqrt{\frac{2}{\pi^3}}\frac{2}{3\epsilon_0 c^3}\frac{n_{g1}n_{g2}}{n_1^2 n_2^2 n_p}\frac{(d_{\text{eff}})^2\omega_p^2}{\sqrt{\kappa}}\left\|\frac{\sigma_p^2}{\sigma_1^2+2\sigma_p^2}\right\|^2\frac{P}{\sigma_p^2}L_z^{3/2}$
Type-0/I, MM	$\frac{32\sqrt{2\pi^3}}{27\epsilon_0 c}\left(\frac{n_{g1}n_{g2}}{n_1^2 n_2^2}\right)\frac{d_{\text{eff}}^2}{\lambda_p^3\sqrt{\kappa}}\frac{P\sqrt{L_z}}{\phi}$
Type-II, SM	$\frac{1}{\pi\epsilon_0 c^2}\frac{n_{g1}n_{g2}}{n_1^2 n_2^2 n_p}\frac{(d_{\text{eff}})^2\omega_p^2}{\Delta n_g}\left\|\frac{\sigma_p^2}{\sigma_1^2+2\sigma_p^2}\right\|^2\frac{P}{\sigma_p^2}L_z$

The material system that met these requirements was a periodically poled potassium titanyl phosphate (PPKTP) waveguide from ADVR. The periodic poling gives access to the largest coefficient axis ((d_{33} , 14 pm/V) for type-0 SPDC (pump, signal, idler are all the same polarization) in the KTP crystal. The PPKTP waveguide is 20 mm in length, with a mode field of 7 μm, pump, signal/idler index of refractions of 1.7497 and 1.7282 respectively, and a pump power of 7 mW. Utilizing the equation above for Type-0 singlemode SPDC, a pair generation rate of greater than 58×10^9 pairs/sec can be achieved [118].

7.1.1 Experimental Configuration

The goal of the source was to be roughly turn-key, with fiber-based components utilized wherever possible as shown in 7.1. The source begins with a 775 nm tunable diode laser (New Focus Velocity) which is followed by a polarization controller and a fiber polarizing beamsplitter to control the optical power used to pump the PPKTP crystals (this is our attenuator). The reason for these components is so the pump laser can remain at a constant power level to maintain lasing stability far from cavity threshold.

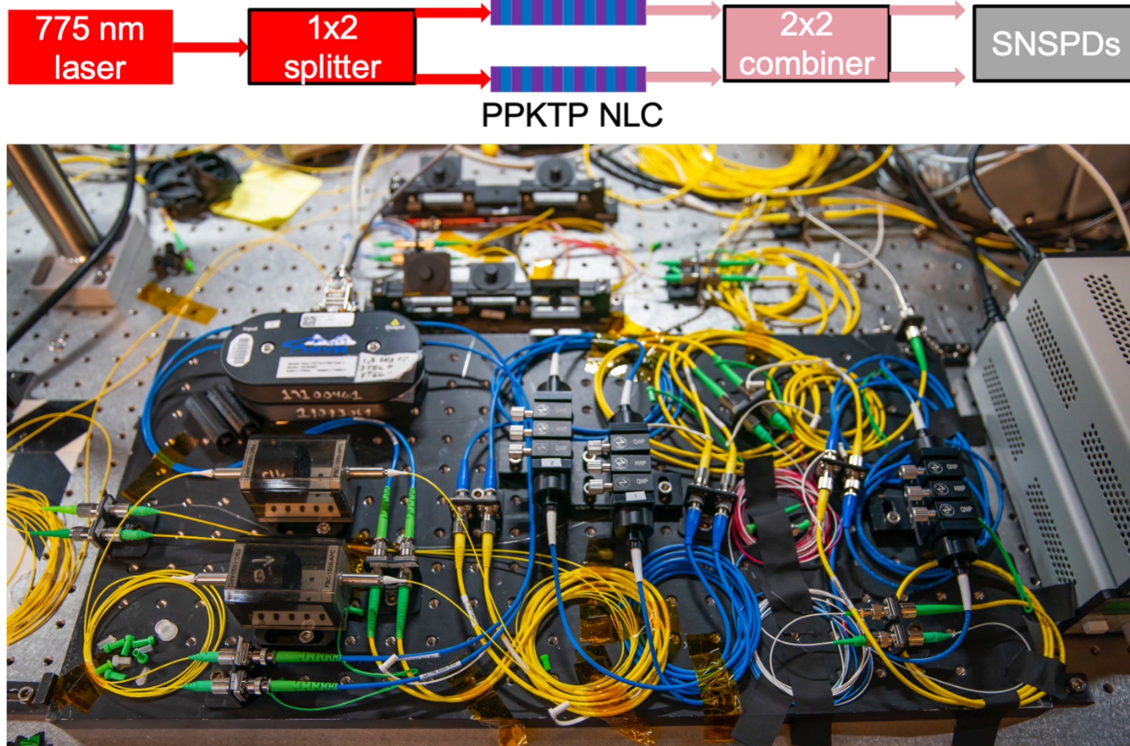

Figure 7.1: (Top) Layout schematic of the entire source from laser to detectors. (Bottom) Photograph of the source with a full component description in the text.

Following the fiber polarizing beamsplitter, the pump light is routed to a 1x2 fiber splitter where each of those legs encounters a polarization controller to optimize the pump polarization before entering the PPKTP waveguide. Next, the pump light passes through the PPKTP waveguide where the pump light generates signal/idler pairs collected in the output fiber and sent to a free space fiber bench. Located in the fiber bench is a stack of 1310 nm long-wave pass semrock filters to remove the rest of the pump light from the optical path before sending the signal/idler pairs to polarization controllers and a 2x2 fiber coupler. This coupler allows a mixture of the pairs resulting in an $N-photon, 0-photon \pm 0-photon, N-photon$ state, called a N00N state, created from two singlemode non-classical (squeezed) states [119–121]. The resulting photons are then sent to measurement equipment for verification.

Once each PPKTP crystal is confirmed to function as expected, it is necessary to spectrally overlap the outputs of the two individual PPKTP crystals while the pump wavelength remains fixed. This is done by tuning the phase matching of each crystal by adjusting the crystal oven

temperature which in turn changes the crystals index of refraction. The photon flux of the PPKTP crystals was large enough that the signal/idler signals could be directly viewed on an optical spectrum analyzer (OSA) as seen in Fig. 7.2. This made it very efficient to spectrally overlap the output of each crystal and verify the spectrums stability. It should also be noted that since these crystals are Type-0 phased matched, the resulting phase matched bandwidth is very broad, over 200 nm. Analyzing the data from these traces, confirms the generation rate of 58×10^9 pairs/sec from each source.

After the two sources were aligned, each was connected to the polarization controllers, then the 2x2 splitter, and each output is then routed to a superconducting nanowire single photon detector (SNSPD) with a timing counter (picoquant Hydraharp). The saturated count rate of the SNSPDs is 10×10^6 with an ideal rate of 3×10^6 which the source immediately surpassed. Adjusting the pump laser attenuator at the beginning of the source reduced the photon generation rate into the detectors range. At the new pump power of 20 μWs, the source produced 3 million singles counts per second, and coincidence in the 100,000 counts per second range. If a reduced spectral bandwidth of the source is required narrowband telecommunication filters will be placed in the fiber benches, and then optimize the coincidence signal by changing the crystal ovens temperature. For the general realm of quantum optics experiments this is a high enough photon flux for reasonable detector integration times and to overcome most optical losses in a system. The system can also be packaged into a rack mountable unit if required to be moved lab-to-lab or into the field.

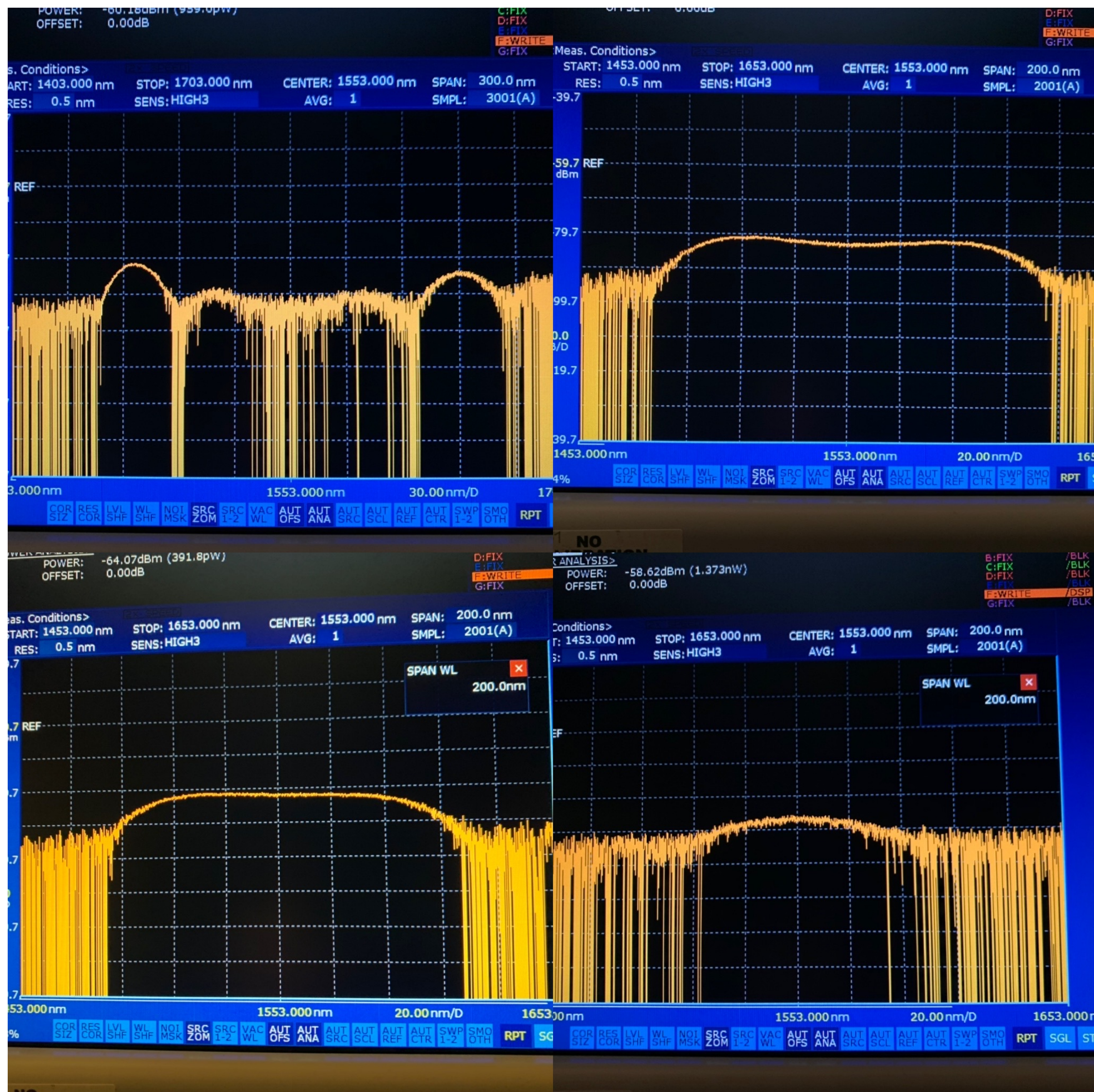

Figure 7.2: (Clockwise from upper left) OSA spectral plot from a single PPKTP show that tuning the crystals oven temperature by 2° Celsius allows the spectral output to go from spectral non-degeneracy to spectral degeneracy.

Chapter 8

Discussion

8.1 Discussion

8.1.1 Conclusions

Quantum systems are an extremely powerful resource for sensing, communications, networking, and information processing/computing. One of the main difficulties in scaling these systems is due to the fragile nature of the entanglement between the qubits. This destruction, called decoherence, can be caused from both internal and external perturbations to the system, such as but not limited, to temperature fluctuations, propagation loss, fabrication errors, and extraneous electro-magnetic fields. Creating a system in a monolithic platform minimizes the variables that would otherwise need to be controlled in a bulk optics-based system (loss, temperature, shielding, etc.), giving scalability to the system. The research results described in this document show that to date significant strides have been made towards accomplishing that goal.

The ultraviolet regime is a challenging area to work since most materials exhibit strong absorption and hence the re-emission is in the form of parasitics (Raman, Brillouin) giving a red shifted photon background adding to the noise floor. In this research we were able to show that propagation loss at 369.5 nm is several tens of orders of magnitude lower than the propagation loss shown by Stegmaier et al. for 400 nm wavelength in an AlN on SiO_2

platform [98]. Furthermore, the crystalline AlN on sapphire material in our platform, just like any other crystalline material, allow for refined Raman and other parasitic processes to be localized and minimized [122]. Although the UV single mode propagation loss presented here is higher than that shown in SiN-on-SiO_2 multimode and planar waveguides for wavelength at the lower end of the visible spectrum [123, 124] and silica-on-silicon waveguides in theory for UV and VIS [125, 126], SiN-on-SiO_2 and silica-on-silicon platforms are limited to passive components and thermo-optic tuners [127]. Furthermore, silica waveguides are low index contrast making them not ideal for compact, high-density, large-scale photonic integration. Hence, this AlN on sapphire platform, to date, has the record-low waveguide propagation loss down to UV wavelength for active optical materials with $\chi^{(2)}$ properties and supports chip-scale, compact, CMOS-compatible integration [98, 128]. Nonetheless, we believe that there are many sources of loss that can be eliminated or improved upon. One of the main causes for the propagation loss is interface scattering from the roughness of the AlN waveguide sidewalls from etching and this will be addressed in the future research. To reduce the propagation loss by a few orders of magnitude, waveguides are designed such that the optical mode overlaps minimally with the sidewalls reducing scattering [93]. Furthermore, the current waveguide fabrication is optimized for vertical sidewalls so that the photonic components experimentally match well with the simulated design. As such, the reactive-ion etching necessitates a fast physical etch that causes the sidewalls to be rougher than could be possible with a more chemical etch. Sidewall roughness of less than 0.1 nm is often the benchmark for achieving interface scattering close to that of the bulk scattering limit of optical materials [129]. It may be possible to further optimize the etching parameters to reduce loss. In addition, there is an inherent roughness of the top surface of the AlN thin film from the unoptimized growth (an active research area). As AlN grown on top of sapphire is still not at the level of silicon on insulator (SOI) wafers made by Smart-Cut® technology used in conventional integrated photonic platforms [130], we expect there to be room for improvements. Finally, the AlN thin film we use is crystalline in the growth direction and polycrystalline in the in-plane direction. Replacing this material with a completely crystalline AlN thin film grown on top of sapphire

should result in a lower dislocation density and defect density, thereby improving the purity of our material so that it would behave closer to what is expected of bulk AlN. Furthermore, the crystallinity of single-crystal AlN grown on top of sapphire has been shown to improve significantly by high temperature annealing [131].

This work shows the highest demonstrated resonator Q factor in the UV, as well as higher VIS resonator Q factor than in previous AlN on SiO_2 work [27]. As the AlN thin film shown in this work is crystalline with fewer absorptive defects and dislocation density than the polycrystalline AlN in previous work, AlN on sapphire can in principle support wavelength into the deep UV; SiN has been shown to have significant optical absorption in wavelengths less than 470 nm and down into the UV range due to silicon incorporation into the layers inherent in the SiN growth [132]. Due to this, even though state-of-the-art SiN on SiO_2 has lower single mode waveguide loss compared to AlN single mode waveguides in the visible wavelength, AlN photonics perform well into the UV regime. Furthermore, AlN has a high piezoelectric coefficient and moderately high electro-optic coefficient for phase and amplitude modulation, allowing for low power consumption active optical components. Finally, AlN's high thermal conductivity κ and small thermo-optic coefficient $\mathrm{d}n/\mathrm{dT}$ allows devices to be less sensitive to temperature fluctuations, which is important for many quantum applications.

This work describes the strides that have been made to push the envelope of commercials foundries to create quantum photonic devices on a manufacturable scale. Through partnerships with AIM Photonics and CNSE, the optical loss has been reduced to record breaking levels where high quality quantum devices are being produced. Through the partnership with CNSE, the introduction of novel materials into the foundry line will allow a rapid increase in not only the quality but also the type of quantum devices that can even be fabricated. Thus, making the linkage of heterogeneous qubit technologies, and coherent quantum transduction between them a reality.

In conclusion, we have demonstrated a PIC platform based on the crystalline, wurtzite AlN on top of a sapphire substrate. Both AlN and sapphire are ultra-wide bandgap (6.2 eV [133] and 8.8 eV [134], respectively) and transparent from the UV to the mid-infrared [30, 135, 136]. We

observe record-high quality factors exceeding 20,000 down to 369.5 nm, which corresponds to record-low propagation loss at 369.5 nm for active optical materials that have $\chi^{(2)}$ properties. The nonlinear, electro-optic, and piezo-electric properties of AlN make it a promising active material for controlling and connecting atomic and atom-like quantum memories, coherent quantum transduction, entangled photon generation, and frequency conversion.

8.1.2 Future Research

Aluminum nitride is proving to be a very promising optical material and gaining a foothold in the integrated photonics community. This is a huge benefit for integrated photonics because most $\chi^{(2)}$ materials such as lithium niobate do not appear in the CMOS fabrication line, whereas aluminum nitride already does. The aluminum nitride that exists in the CMOS line right now is not optical quality but meant as an insulator for high voltage electronic circuitry. That being said, the material does exist in the foundry line, which brings up the question can it be utilized for photonic waveguides [137, 138]. This is exactly why a partnership was created with CNSE, where CNSE utillizes our designs and fabricates 300 mm wafer of aluminum nitride devices. The devices will be fabricated through two processes, (i) standard photolithography and a reactive ion etch to create the waveguides, and (ii) a damascene process where the silicon dioxide is patterned through photolithography, etched, the aluminum nitride is grown into patterned trenches, and then the wafer is chemical mechanical polished to remove the excess material. In either case the aluminum nitride is expected to be polycrystalline which will add scattering loss in the ultraviolet but this is precisely why the designs are weighted towards the far visible and near infrared, which is also a region of low absorption for aluminum nitride.

The first important set of devices on these wafers consist of electro-optic devices for modulation and tunable direction couplers and are expected to be delivered early summer of 2020. These are fundamental structures for building quantum information processors since these control the phase applied to the state, and the amplitude weighting in a specific waveguide allowing for entangling operations to occur. When these two components are combined the

resulting device is a Mach-Zehnder modulator, a key component to information processing (the same device can model a neuron in a neural network, or a $N \times N$ switch in a telecommunications system). These devices will be evaluated for their effective tuning range and phase shifting capability. If successful, this will allow access to an electro-optic material in a CMOS foundry, a critical milestone for high speed, low power photonic devices.

The second set of devices on these wafers are arrays of single bus microring resonators to be used as filters and bi/entangled photon generators. The microring resonators on this particular fabrication run will be passive devices to reduce the fabrication complexity and to aid in measuring the device loss and dispersion without any absorbing material nearby, such as metal. The confinement of the microring resonators allows for a high field intensity in the cavity, increasing the likelihood that pump photons will be converted into bi-photon pairs through SPDC or SFWM. Generation and validation of bi-photon pair production in the CMOS foundry fabricated aluminum nitride waveguides is the second experiment to be performed.

Incorporation of a quantum memory is a needed task for quantum repeaters. There are any instantiations quantum memories, with a few examples being defect sites in materials such as diamond, silicon carbide, quantum dots, or trapped ions. This experiment would involve a number of different tasks. First is to incorporate the quantum memory into the platform. This is relatively easy with defect sites as the device can be fabricated on a different platform and transferred to the aluminum nitride platform. With trapped ions or any charged particle it is more difficult as the particle will interact with objects near it, degrading the qubit performance. Therefore, care must be taken to isolate those qubits while creating an on chip aluminum nitride surface ion trap. Lastly, dispersion engineering of the photon device (microring resonator, photonic crystal cavity, etc.) must occur so the wavelength of the memory and the wavelength of the network are phase matched for efficient coherent frequency conversion. This experiment will be performed at AFRL with the quantum information processing group, the quantum networking group, RIT, SUNY Poly, and MIT.

The second experiment is to combine superconducting quantum circuits fabricated in nio-

bium nitride with aluminum nitride opto-mechanical/optical circuits [139, 140]. Superconducting quantum circuits serve as a very stable, and scalable platform for both quantum information processing, and quantum memories. Most of the largest quantum information processors to date are created with superconducting qubits (Google IBM, Rigetti). The superconducting qubits are great for local operations (near neighbor interactions) with the final qubit readout occurring in the microwave region. Due to the fact that the read out is in the microwave regime, a low energy interaction is required to coherently transfer the quantum information to a different qubit. In this experiment we will utilize the piezo-electric properties of an aluminum nitride opto-mechanical resonator and couple that vibrational mode with a superconducting circuit to coherently transduce a microwave photon to the telecommunications regime. This experiment will be performed at AFRL with the quantum information processing group, the hybrid superconducting group, RIT, SUNY Poly, and Syracuse University.

The future of aluminum nitride is extremely promising for the photonics industry. The appealing properties such as an ultrawide-bandgap, a second order nonlinearity, electro-optic effect, piezo-electric effect, acousto-optic effect, CMOS compatibility etc. poise aluminum nitride as the next breakthrough material, and as an ideal material candidate for a universal integrated photonics platform.

Bibliography

[1] Chris Monroe. Quantum information processing with atoms and photons. *Nature*, 416 (6877):238, 2002. 1.1

[2] Fulvio Flamini, Nicolò Spagnolo, and Fabio Sciarrino. Photonic quantum information processing: a review. *Reports on Progress in Physics*, 82(1):016001, 2018. 1.1

[3] H Jeff Kimble. The quantum internet. *Nature*, 453(7198):1023, 2008. 1.1

[4] TE Northup and R Blatt. Quantum information transfer using photons. *Nature photonics*, 8(5):356, 2014.

[5] Matthias Bock, Pascal Eich, Stephan Kucera, Matthias Kreis, Andreas Lenhard, Christoph Becher, and Jürgen Eschner. High-fidelity entanglement between a trapped ion and a telecom photon via quantum frequency conversion. *Nature communications*, 9(1):1998, 2018. 1.1

[6] Sheng-Kai Liao, Wen-Qi Cai, Johannes Handsteiner, Bo Liu, Juan Yin, Liang Zhang, Dominik Rauch, Matthias Fink, Ji-Gang Ren, Wei-Yue Liu, et al. Satellite-relayed intercontinental quantum network. *Physical review letters*, 120(3):030501, 2018. 1.1

[7] Nicolas Gisin and Rob Thew. Quantum communication. *Nature photonics*, 1(3):165, 2007. 1.1

[8] Anaïs Dréau, Anna Tchebotareva, Aboubakr El Mahdaoui, Cristian Bonato, and Ronald Hanson. Quantum frequency conversion of single photons from a nitrogen-vacancy center

in diamond to telecommunication wavelengths. *Physical Review Applied*, 9(6):064031, 2018. 1.1

[9] Daniel Riedel, Immo Söllner, Brendan J Shields, Sebastian Starosielec, Patrick Appel, Elke Neu, Patrick Maletinsky, and Richard J Warburton. Deterministic enhancement of coherent photon generation from a nitrogen-vacancy center in ultrapure diamond. *Physical Review X*, 7(3):031040, 2017. 1.1

[10] Atature Kiraz, M Atatüre, and A Imamoğlu. Quantum-dot single-photon sources: Prospects for applications in linear optics quantum-information processing. *Physical Review A*, 69(3):032305, 2004. 1.1

[11] Xiyuan Lu, Qing Li, Daron A Westly, Gregory Moille, Anshuman Singh, Vikas Anant, and Kartik Srinivasan. Chip-integrated visible–telecom entangled photon pair source for quantum communication. *Nature Physics*, 15(4):373, 2019. 1.1

[12] Robert W Boyd. *Nonlinear optics*. Elsevier, 2003. 1.2

[13] Govind P Agrawal. Nonlinear fiber optics. In *Nonlinear Science at the Dawn of the 21st Century*, pages 195–211. Springer, 2000. 1.2

[14] Joshua W Silverstone, Damien Bonneau, Jeremy L O'Brien, and Mark G Thompson. Silicon quantum photonics. *IEEE Journal of Selected Topics in Quantum Electronics*, 22(6):390–402, 2016. 1.4, 1.4

[15] Xiang Zhang, Bryn A Bell, Andri Mahendra, Chunle Xiong, Philip HW Leong, and Benjamin J Eggleton. Integrated silicon nitride time-bin entanglement circuits. *Optics letters*, 43(15):3469–3472, 2018. 1.4

[16] Myoung-Gyun Suh and Kerry J Vahala. Soliton microcomb range measurement. *Science*, 359(6378):884–887, 2018. 1.4

[17] Enzo Di Fabrizio, Sebastian Schlücker, Jérôme Wenger, Raju Regmi, Hervé Rigneault, Giuseppe Calafiore, Melanie West, Stefano Cabrini, Monika Fleischer, Niek F Van Hulst,

et al. Roadmap on biosensing and photonics with advanced nano-optical methods. *Journal of Optics*, 18(6):063003, 2016. 1.4

[18] Gavin N West, William Loh, Dave Kharas, Cheryl Sorace-Agaskar, Karan K Mehta, Jeremy Sage, John Chiaverini, and Rajeev J Ram. Low-loss integrated photonics for the blue and ultraviolet regime. *APL Photonics*, 4(2):026101, 2019. 1.4

[19] Olivier Alibart, Virginia D'Auria, Marc De Micheli, Florent Doutre, Florian Kaiser, Laurent Labonté, Tommaso Lunghi, Eric Picholle, and Sébastien Tanzilli. Quantum photonics at telecom wavelengths based on lithium niobate waveguides. *Journal of Optics*, 18(10):104001, 2016. 1.4

[20] Roland Krischek, Witlef Wieczorek, Akira Ozawa, Nikolai Kiesel, Patrick Michelberger, Thomas Udem, and Harald Weinfurter. Ultraviolet enhancement cavity for ultrafast nonlinear optics and high-rate multiphoton entanglement experiments. *Nature Photonics*, 4 (3):170, 2010. 1.4

[21] Mohammad Soltani, Richard Soref, Tomas Palacios, and Dirk Englund. Algan/aln integrated photonics platform for the ultraviolet and visible spectral range. *Optics express*, 24(22):25415–25423, 2016. 1.4

[22] Kae Nemoto, Michael Trupke, Simon J Devitt, Ashley M Stephens, Burkhard Scharfenberger, Kathrin Buczak, Tobias Nöbauer, Mark S Everitt, Jörg Schmiedmayer, and William J Munro. Photonic architecture for scalable quantum information processing in diamond. *Physical Review X*, 4(3):031022, 2014. 1.4

[23] Mihir Pant, Hyeongrak Choi, Saikat Guha, and Dirk Englund. Percolation based architecture for cluster state creation using photon-mediated entanglement between atomic memories. *arXiv preprint arXiv:1704.07292*, 2017.

[24] L-M Duan and Christopher Monroe. Colloquium: Quantum networks with trapped ions. *Reviews of Modern Physics*, 82(2):1209, 2010.

[25] Emre Togan, Yiwen Chu, AS Trifonov, Liang Jiang, Jeronimo Maze, Lilian Childress, MV Gurudev Dutt, Anders Søndberg Sørensen, PR Hemmer, Alexander S Zibrov, et al. Quantum entanglement between an optical photon and a solid-state spin qubit. *Nature*, 466(7307):730, 2010.

[26] Lilian Childress, Ronald Walsworth, and Mikhail Lukin. Atom-like crystal defects. *Physics Today*, 67(10):38, 2014. 1.4

[27] Chi Xiong, Wolfram HP Pernice, Xiankai Sun, Carsten Schuck, King Y Fong, and Hong X Tang. Aluminum nitride as a new material for chip-scale optomechanics and nonlinear optics. *New Journal of Physics*, 14(9):095014, 2012. 1.4, 8.1.1

[28] Karan K Mehta, Colin D Bruzewicz, Robert McConnell, Rajeev J Ram, Jeremy M Sage, and John Chiaverini. Integrated optical addressing of an ion qubit. *Nature nanotechnology*, 11(12):1066, 2016. 1.4

[29] Sara L Mouradian, Tim Schröder, Carl B Poitras, Luozhou Li, Jordan Goldstein, Edward H Chen, Michael Walsh, Jaime Cardenas, Matthew L Markham, Daniel J Twitchen, et al. Scalable integration of long-lived quantum memories into a photonic circuit. *Physical Review X*, 5(3):031009, 2015. 1.4, 3.1, 5.1.2

[30] Chi Xiong, Wolfram HP Pernice, and Hong X Tang. Low-loss, silicon integrated, aluminum nitride photonic circuits and their use for electro-optic signal processing. *Nano letters*, 12(7):3562–3568, 2012. 1.4, 8.1.1

[31] Chi Xiong, Wolfram HP Pernice, Xiankai Sun, Carsten Schuck, King Y Fong, and Hong X Tang. Aluminum nitride as a new material for chip-scale optomechanics and nonlinear optics. *New Journal of Physics*, 14(9):095014, 2012. 1.4

[32] Chi Xiong, Xiankai Sun, King Y Fong, and Hong X Tang. Integrated high frequency aluminum nitride optomechanical resonators. *Applied Physics Letters*, 100(17):171111, 2012. 1.4

[33] SP Fang and Henry F Taylor. High-performance single-mode fiber-optic switch. *Optics letters*, 19(16):1204–1206, 1994. 1.4

[34] WHP Pernice, C Xiong, C Schuck, and HX Tang. Second harmonic generation in phase matched aluminum nitride waveguides and micro-ring resonators. *Applied Physics Letters*, 100(22):223501, 2012. 1.4

[35] Y Fujii, S Yoshida, S Misawa, S Maekawa, and T Sakudo. Nonlinear optical susceptibilities of aln film. *Applied Physics Letters*, 31(12):815–816, 1977. 1.4

[36] Hojoong Jung, Chi Xiong, King Y Fong, Xufeng Zhang, and Hong X Tang. Optical frequency comb generation from aluminum nitride microring resonator. *Optics letters*, 38(15):2810–2813, 2013. 1.4

[37] Hojoong Jung, Rebecca Stoll, Xiang Guo, Debra Fischer, and Hong X Tang. Green, red, and ir frequency comb line generation from single ir pump in aln microring resonator. *Optica*, 1(6):396–399, 2014. 1.4

[38] Xiang Guo, Chang-Ling Zou, Hojoong Jung, and Hong X Tang. On-chip strong coupling and efficient frequency conversion between telecom and visible optical modes. *Physical review letters*, 117(12):123902, 2016.

[39] Xianwen Liu, Changzheng Sun, Bing Xiong, Lai Wang, Jian Wang, Yanjun Han, Zhibiao Hao, Hongtao Li, Yi Luo, Jianchang Yan, et al. Integrated continuous-wave aluminum nitride raman laser. *Optica*, 4(8):893–896, 2017. 1.4

[40] T Troha, M Rigler, D Alden, I Bryan, W Guo, R Kirste, S Mita, MD Gerhold, R Collazo, Z Sitar, et al. Uv second harmonic generation in aln waveguides with modal phase matching. *Optical Materials Express*, 6(6):2014–2023, 2016. (document), 1.4, 2.16, 2.2

[41] Hojoong Jung and Hong X Tang. Aluminum nitride as nonlinear optical material for on-chip frequency comb generation and frequency conversion. *Nanophotonics*, 5(2):263–271, 2016. 1.4

[42] Xiang Guo, Chang-ling Zou, Carsten Schuck, Hojoong Jung, Risheng Cheng, and Hong X Tang. Parametric down-conversion photon-pair source on a nanophotonic chip. *Light: Science & Applications*, 6(5):e16249, 2017. 1.4, 5.1.2

[43] Xianwen Liu, Changzheng Sun, Bing Xiong, Lai Wang, Jian Wang, Yanjun Han, Zhibiao Hao, Hongtao Li, Yi Luo, Jianchang Yan, et al. Broadband frequency comb generation in aluminum nitride-on-sapphire microresonators. *arXiv preprint arXiv:1611.01994*, 2016. 1.4

[44] P Motamedi and K Cadien. Structural and optical characterization of low-temperature ald crystalline aln. *Journal of Crystal Growth*, 421:45–52, 2015. (document), 2.1, 2.6, 2.13

[45] Han-Yong Joo, Hyeong Joon Kim, Sang June Kim, and Sang Youl Kim. Spectrophotometric analysis of aluminum nitride thin films. *Journal of Vacuum Science & Technology A: Vacuum, Surfaces, and Films*, 17(3):862–870, 1999. 2.1

[46] Glen A Slack, Leo J Schowalter, Donald Morelli, and Jaime A Freitas Jr. Some effects of oxygen impurities on aln and gan. *Journal of Crystal Growth*, 246(3-4):287–298, 2002. 2.1

[47] M Bickermann, BM Epelbaum, and A Winnacker. Characterization of bulk aln with low oxygen content. *Journal of Crystal Growth*, 269(2-4):432–442, 2004. 2.1

[48] Matthias Bickermann, Boris M Epelbaum, Octavian Filip, Paul Heimann, Shunro Nagata, and Albrecht Winnacker. Uv transparent single-crystalline bulk aln substrates. *physica status solidi c*, 7(1):21–24, 2010. (document), 2.1, 2.2

[49] A Uedono, S Ishibashi, S Keller, C Moe, P Cantu, TM Katona, DS Kamber, Y Wu, E Letts, SA Newman, et al. Vacancy-oxygen complexes and their optical properties in aln epitaxial films studied by positron annihilation. *Journal of Applied Physics*, 105(5): 054501, 2009. (document), 2.3

[50] Alistair D Westwood, Robert A Youngman, Martha R McCartney, Alastair N Cormack, and Michael R Notis. Oxygen incorporation in aluminum nitride via extended defects: Part i. refinement of the structural model for the planar inversion domain boundary. *Journal of materials research*, 10(5):1270–1286, 1995. 2.1

[51] Alistair D Westwood, Robert A Youngman, Martha R McCartney, Alastair N Cormack, and Michael R Notis. Oxygen incorporation in aluminum nitride via extended defects: Part ii. structure of curved inversion domain boundaries and defect formation. *Journal of materials research*, 10(5):1287–1300, 1995.

[52] Alistair D Westwoord, Robert A Youngman, Martha R McCartney, Alasiair N Cormack, and Michael R Notis. Oxygen incorporation in aluminum nitride via extended defects: Part iii. reevaluation of the polytypoid structure in the aluminum nitride-aluminum oxide binary system. *Journal of materials research*, 10(10):2573–2585, 1995. (document), 2.1, 2.11, 2.12

[53] Issei Satoh, Satoshi Arakawa, Keisuke Tanizaki, Michimasa Miyanaga, Takashi Sakurada, Yoshiyuki Yamamoto, and Hideaki Nakahata. Development of aluminum nitride single-crystal substrates. *SEI Technical Review*, 1(71):79, 2010. (document), 2.1, 2.5

[54] TJA Mori, RD Della Pace, AMH de Andrade, MA Corrêa, P Stamenov, LF Schelp, and LS Dorneles. Growth of c-axis-oriented aluminum nitride thin films onto different substrates and buffer layers. *Surface and Interface Analysis*, 47(4):447–453, 2015. 2.1

[55] Markus Bosund, Timo Sajavaara, Mikko Laitinen, Teppo Huhtio, Matti Putkonen, Veli-Matti Airaksinen, and Harri Lipsanen. Properties of aln grown by plasma enhanced atomic layer deposition. *Applied Surface Science*, 257(17):7827–7830, 2011.

[56] Z Chen, S Newman, D Brown, R Chung, S Keller, UK Mishra, SP Denbaars, and S Nakamura. High quality aln grown on sic by metal organic chemical vapor deposition. *Applied Physics Letters*, 93(19):191906, 2008.

[57] MT Hardy, DF Storm, N Nepal, DS Katzer, BP Downey, and DJ Meyer. Indium

incorporation dynamics in n-polar inaln thin films grown by plasma-assisted molecular beam epitaxy on freestanding gan substrates. *Journal of Crystal Growth*, 425:119–124, 2015.

[58] Jaime Andrés Pérez Taborda, Henry Riascos Landázuri, and Liliana Patricia Vera Londoño. Correlation between optical, morphological, and compositional properties of aluminum nitride thin films by pulsed laser deposition. *IEEE Sensors Journal*, 16(2): 359–364, 2015.

[59] Shakil Khan, Muhammad Shahid, A Mahmood, A Shah, Ishaq Ahmed, Mazhar Mehmood, U Aziz, Q Raza, and M Alam. Texture of the nano-crystalline aln thin films and the growth conditions in dc magnetron sputtering. *Progress in Natural Science: Materials International*, 25(4):282–290, 2015. (document), 2.1, 2.7, 2.8

[60] Hojoong Jung and Hong X Tang. Aluminum nitride as nonlinear optical material for on-chip frequency comb generation and frequency conversion. *Nanophotonics*, 5(2):263–271, 2016. (document), 2.9, 2.2

[61] Satoru Tanaka, R Scott Kern, James Bentley, and Robert F Davis. Defect formation during hetero-epitaxial growth of aluminum nitride thin films on 6h-silicon carbide by gas-source molecular beam epitaxy. *Japanese journal of applied physics*, 35(3R):1641, 1996. (document), 2.10

[62] Pouyan Motamedi and Ken Cadien. Xps analysis of aln thin films deposited by plasma enhanced atomic layer deposition. *Applied surface science*, 315:104–109, 2014. (document), 2.13

[63] Leland Rosenberger, Ronald Baird, Erik McCullen, Gregory Auner, and Gina Shreve. Xps analysis of aluminum nitride films deposited by plasma source molecular beam epitaxy. *Surface and Interface Analysis: An International Journal devoted to the development and application of techniques for the analysis of surfaces, interfaces and thin films*, 40(9):1254–1261, 2008. (document), 2.14

[64] M Stegmaier, J Ebert, JM Meckbach, K Ilin, M Siegel, and WHP Pernice. Aluminum nitride nanophotonic circuits operating at ultraviolet wavelengths. *Applied Physics Letters*, 104(9):091108, 2014. (document), 2.15

[65] John Morgan, John Notte, Raymond Hill, and Bill Ward. An introduction to the helium ion microscope. *Microscopy today*, 14(4):24–31, 2006. 2.1.4

[66] Tsung-Ju Lu, Michael Fanto, Hyeongrak Choi, Paul Thomas, Jeffrey Steidle, Sara Mouradian, Wei Kong, Di Zhu, Hyowon Moon, Karl Berggren, et al. Aluminum nitride integrated photonics platform for the ultraviolet to visible spectrum. *Optics express*, 26 (9):11147–11160, 2018. (document), 2.17, 2.2, 4.2

[67] Xianwen Liu, Alexander W Bruch, Zheng Gong, Juanjuan Lu, Joshua B Surya, Liang Zhang, Junxi Wang, Jianchang Yan, and Hong X Tang. Ultra-high-q uv microring resonators based on a single-crystalline aln platform. *Optica*, 5(10):1279–1282, 2018. 2.2

[68] WHP Pernice, C Xiong, C Schuck, and HX Tang. Second harmonic generation in phase matched aluminum nitride waveguides and micro-ring resonators. *Applied Physics Letters*, 100(22):223501, 2012. (document), 2.18, 2.2

[69] Xianwen Liu, Alexander W Bruch, Juanjuan Lu, Zheng Gong, Joshua B Surya, Liang Zhang, Junxi Wang, Jianchang Yan, and Hong X Tang. Beyond 100 thz-spanning ultraviolet frequency combs in a non-centrosymmetric crystalline waveguide. *arXiv preprint arXiv:1906.00323*, 2019. (document), 2.2, 2.19, 2.2

[70] Xiang Guo, Chang-ling Zou, Carsten Schuck, Hojoong Jung, Risheng Cheng, and Hong X Tang. Parametric down-conversion photon-pair source on a nanophotonic chip. *Light: Science & Applications*, 6(5):e16249, 2017. 2.2

[71] Dorian Alden, Tinkara Troha, Ronny Kirste, Seiji Mita, Qiang Guo, Axel Hoffmann, Marko Zgonik, Ramón Collazo, and Zlatko Sitar. Quasi-phase-matched second harmonic generation of uv light using aln waveguides. *Applied Physics Letters*, 114(10):103504, 2019. 2.2

[72] Xiang Guo, Chang-Ling Zou, and Hong X Tang. Second-harmonic generation in aluminum nitride microrings with 2500%/w conversion efficiency. *Optica*, 3(10):1126–1131, 2016. 2.2

[73] Hojoong Jung, Chi Xiong, King Y Fong, Xufeng Zhang, and Hong X Tang. Optical frequency comb generation from aluminum nitride microring resonator. *Optics letters*, 38(15):2810–2813, 2013. 2.2

[74] Shiyang Zhu, Qize Zhong, Ting Hu, Yu Li, Zhengji Xu, Yuan Dong, and Navab Singh. Aluminum nitride ultralow loss waveguides and push-pull electro-optic modulators for near infrared and visible integrated photonics. In *2019 Optical Fiber Communications Conference and Exhibition (OFC)*, pages 1–3. IEEE, 2019. 2.2

[75] Pao Tai Lin, Hojoong Jung, Lionel C Kimerling, Anu Agarwal, and Hong X Tang. Low-loss aluminium nitride thin film for mid-infrared microphotonics. *Laser & Photonics Reviews*, 8(2):L23–L28, 2014. 3.1

[76] David J Moss, Roberto Morandotti, Alexander L Gaeta, and Michal Lipson. New cmos-compatible platforms based on silicon nitride and hydex for nonlinear optics. *Nature photonics*, 7(8):597, 2013. 3.1

[77] Tristan Koppe, Hans Hofsäss, and Ulrich Vetter. Overview of band-edge and defect related luminescence in aluminum nitride. *Journal of Luminescence*, 178:267–281, 2016. 3.1

[78] Christopher Monroe and Jungsang Kim. Scaling the ion trap quantum processor. *Science*, 339(6124):1164–1169, 2013. 3.1

[79] A Goban, C-L Hung, S-P Yu, JD Hood, JA Muniz, JH Lee, MJ Martin, AC McClung, KS Choi, Darrick E Chang, et al. Atom–light interactions in photonic crystals. *Nature communications*, 5:3808, 2014. 3.1

[80] Joel KW Yang and Karl K Berggren. Using high-contrast salty development of hydrogen silsesquioxane for sub-10-nm half-pitch lithography. *Journal of Vacuum Science*

& Technology B: Microelectronics and Nanometer Structures Processing, Measurement, and Phenomena, 25(6):2025–2029, 2007. 3.2

[81] Bahaa EA Saleh and Malvin Carl Teich. *Fundamentals of photonics*. john Wiley and sons, 2019. 4.1

[82] Arthur R Nelson. Coupling optical waveguides by tapers. *Applied Optics*, 14(12):3012–3015, 1975. 4.1

[83] Martin Papes, Pavel Cheben, Daniel Benedikovic, Jens H Schmid, James Pond, Robert Halir, Alejandro Ortega-Moñux, Gonzalo Wangüemert-Pérez, N Ye Winnie, Dan-Xia Xu, et al. Fiber-chip edge coupler with large mode size for silicon photonic wire waveguides. *Optics express*, 24(5):5026–5038, 2016.

[84] Jaime Cardenas, Carl B Poitras, Kevin Luke, Lian-Wee Luo, Paul Adrian Morton, and Michal Lipson. High coupling efficiency etched facet tapers in silicon waveguides. *IEEE Photonics Technology Letters*, 26(23):2380–2382, 2014. 4.1

[85] Pao Tai Lin, Vivek Singh, Hao-Yu Greg Lin, Tom Tiwald, Lionel C Kimerling, and Anuradha Murthy Agarwal. Low-stress silicon nitride platform for mid-infrared broadband and monolithically integrated microphotonics. *Advanced Optical Materials*, 1(10): 732–739, 2013. 4.1

[86] S Campbell, RR Thomson, DP Hand, AK Kar, DT Reid, Carlota Canalias, Valdas Pasiskevicius, and Fredrik Laurell. Frequency-doubling in femtosecond laser inscribed periodically-poled potassium titanyl phosphate waveguides. *Optics express*, 15(25): 17146–17150, 2007. 4.1

[87] Shawn Yohanes Siew, Eric Jun Hao Cheung, Haidong Liang, Andrew Bettiol, Noriaki Toyoda, Bandar Alshehri, Elhadj Dogheche, and Aaron J Danner. Ultra-low loss ridge waveguides on lithium niobate via argon ion milling and gas clustered ion beam smoothening. *Optics express*, 26(4):4421–4430, 2018. 4.1

[88] LAM Barea, F Vallini, AR Vaz, JR Mialichi, and NC Frateschi. Low-roughness active microdisk resonators fabricated by focused ion beam. *Journal of Vacuum Science and Technology B: Microelectronics and Nanometer Structures Processing, Measurement, and Phenomena*, 27(6):2979–2981, 2009.

[89] ACG Nutt, JPG Bristow, A McDonach, and PJR Laybourn. Fiber-to-waveguide coupling using ion-milled grooves in lithium niobate at 1.3-μm wavelength. *Optics letters*, 9(10):463–465, 1984. 4.1

[90] Jeffrey A Steidle, Michael L Fanto, Christopher C Tison, Zihao Wang, Paul M Alsing, and Stefan F Preble. Efficiently heralded silicon ring resonator photon-pair source. In *Quantum Information and Computation IX*, volume 9873, page 987304. International Society for Optics and Photonics, 2016. 4.2

[91] Paul M Thomas, Michael Fanto, John Serafini, Jeffrey Steidle, Stefan Preble, Tsung-Ju Lu, and Dirk Englund. Ion milled facet for direct coupling to optical waveguides. In *Micro-and Nanotechnology Sensors, Systems, and Applications XI*, volume 10982, page 109823H. International Society for Optics and Photonics, 2019. 4.3

[92] Vinita Mittal, Neil P Sessions, James S Wilkinson, and Ganapathy Senthil Murugan. Optical quality znse films and low loss waveguides on si substrates for mid-infrared applications. *Optical Materials Express*, 7(3):712–725, 2017. 4.3

[93] Steven A Miller, Mengjie Yu, Xingchen Ji, Austin G Griffith, Jaime Cardenas, Alexander L Gaeta, and Michal Lipson. Low-loss silicon platform for broadband mid-infrared photonics. *Optica*, 4(7):707–712, 2017. 5.1.2, 5.1.2, 8.1.1

[94] Amnon Yariv. Critical coupling and its control in optical waveguide-ring resonator systems. *IEEE Photonics Technology Letters*, 14(4):483–485, 2002.

[95] Amnon Yariv. Universal relations for coupling of optical power between microresonators and dielectric waveguides. *Electronics letters*, 36(4):321–322, 2000.

[96] Jacob Levy. Integrated nonlinear optics in silicon nitride waveguides and resonators. *Thesis, Cornell*, 2011.

[97] Avik Dutt. On-chip quantum and nonlinear optics: from squeezing to spectroscopy. *Thesis, Cornell*, 2017. 5.1.2, 5.1.2

[98] M Stegmaier, J Ebert, JM Meckbach, K Ilin, M Siegel, and WHP Pernice. Aluminum nitride nanophotonic circuits operating at ultraviolet wavelengths. *Applied Physics Letters*, 104(9):091108, 2014. 5.1.2, 8.1.1

[99] Carmen G Almudever, Lingling Lao, Xiang Fu, Nader Khammassi, Imran Ashraf, Dan Iorga, Savvas Varsamopoulos, Christopher Eichler, Andreas Wallraff, Lotte Geck, et al. The engineering challenges in quantum computing. In *Design, Automation & Test in Europe Conference & Exhibition (DATE), 2017*, pages 836–845. IEEE, 2017. 6.1

[100] Antonio D Córcoles, Abhinav Kandala, Ali Javadi-Abhari, Douglas T McClure, Andrew W Cross, Kristan Temme, Paul D Nation, Matthias Steffen, and JM Gambetta. Challenges and opportunities of near-term quantum computing systems. *arXiv preprint arXiv:1910.02894*, 2019. 6.1

[101] Sergio Boixo, Sergei V Isakov, Vadim N Smelyanskiy, Ryan Babbush, Nan Ding, Zhang Jiang, Michael J Bremner, John M Martinis, and Hartmut Neven. Characterizing quantum supremacy in near-term devices. *Nature Physics*, 14(6):595–600, 2018. 6.1

[102] Frank Arute, Kunal Arya, Ryan Babbush, Dave Bacon, Joseph C Bardin, Rami Barends, Rupak Biswas, Sergio Boixo, Fernando GSL Brandao, David A Buell, et al. Quantum supremacy using a programmable superconducting processor. *Nature*, 574(7779):505–510, 2019. 6.1

[103] Colin D Bruzewicz, John Chiaverini, Robert McConnell, and Jeremy M Sage. Trapped-ion quantum computing: Progress and challenges. *Applied Physics Reviews*, 6(2):021314, 2019. 6.1

[104] Daniel Llewellyn, Yunhong Ding, Imad I Faruque, Stefano Paesani, Davide Bacco, Raffaele Santagati, Yan-Jun Qian, Yan Li, Yun-Feng Xiao, Marcus Huber, et al. Chip-to-chip quantum teleportation and multi-photon entanglement in silicon. *Nature Physics*, 16(2):148–153, 2020. 6.1

[105] Damien Bonneau, Joshua W Silverstone, and Mark G Thompson. Silicon quantum photonics. In *Silicon Photonics III*, pages 41–82. Springer, 2016. 6.1

[106] CC Tison, JA Steidle, ML Fanto, Z Wang, NA Mogent, A Rizzo, SF Preble, and PM Alsing. Path to increasing the coincidence efficiency of integrated resonant photon sources. *Optics Express*, 25(26):33088–33096, 2017. 6.2

[107] Pascual Munoz, Paulus WL van Dijk, Douwe Geuzebroek, Michael Geiselmann, Carlos Dominguez, Andim Stassen, José David Doménech, Michael Zervas, Arne Leinse, Chris GH Roeloffzen, et al. Foundry developments toward silicon nitride photonics from visible to the mid-infrared. *IEEE Journal of Selected Topics in Quantum Electronics*, 25(5):1–13, 2019. 6.2

[108] Jonathan H Harris. Sintered aluminum nitride ceramics for high-power electronic applications. *JOM*, 50(6):56–60, 1998. 6.3

[109] Martin Hubert Peter Pfeiffer, Clemens Herkommer, Junqiu Liu, Tiago Morais, Michael Zervas, Michael Geiselmann, and Tobias J Kippenberg. Photonic damascene process for low-loss, high-confinement silicon nitride waveguides. *IEEE Journal of Selected Topics in Quantum Electronics*, 24(4):1–11, 2018. 6.3

[110] Joseph B Altepeter, Evan R Jeffrey, and Paul G Kwiat. Phase-compensated ultra-bright source of entangled photons. *Optics Express*, 13(22):8951–8959, 2005. 7.1

[111] Philip G Evans, Ryan S Bennink, Warren P Grice, Travis S Humble, and Jason Schaake. Bright source of spectrally uncorrelated polarization-entangled photons with nearly single-mode emission. *Physical review letters*, 105(25):253601, 2010.

[112] Paul G Kwiat, Phillippe H Eberhard, and Andrew G White. Ultra-bright source of polarization-entangled photons, July 23 2002. US Patent 6,424,665. 7.1

[113] Charlotte Liljestrand, Fredrik Laurell, and Carlota Canalias. Periodic poling of rb-doped ktiopo 4 by coercive field engineering. *Optics express*, 24(13):14682–14689, 2016. 7.1

[114] Jonathan Tyler Nagy and Ronald M Reano. Periodic poling of ion-sliced x-cut magnesium oxide doped lithium niobate thin films. In *2018 Conference on Lasers and Electro-Optics (CLEO)*, pages 1–2. IEEE, 2018.

[115] Kristina Meier, Fumihiro Kaneda, and Paul Kwiat. Development of highly nondegenerate polarization entanglement on a waveguide spdc source. *Bulletin of the American Physical Society*, 64, 2019. 7.1

[116] Vineet Kumar Shukla and Joyee Ghosh. Generation of two different polarization-entangled biphoton states in a potassium titanyl phosphate waveguide device with multiple periodic poling. *Physical Review A*, 101(2):023832, 2020. 7.1

[117] M Borghi, C Castellan, S Signorini, A Trenti, and L Pavesi. Nonlinear silicon photonics. *Journal of Optics*, 19(9):093002, 2017. 7.1

[118] James Schneeloch, Samuel H Knarr, Daniela F Bogorin, Mackenzie L Levangie, Christopher C Tison, Rebecca Frank, Gregory A Howland, Michael L Fanto, and Paul M Alsing. Introduction to the absolute brightness and number statistics in spontaneous parametric down-conversion. *Journal of Optics*, 21(4):043501, 2019. 7.1

[119] Stefan F Preble, Michael L Fanto, Jeffrey A Steidle, Christopher C Tison, Gregory A Howland, Zihao Wang, and Paul M Alsing. On-chip quantum interference from a single silicon ring-resonator source. *Physical Review Applied*, 4(2):021001, 2015. 7.1.1

[120] Roman Schnabel. Squeezed states of light and their applications in laser interferometers. *Physics Reports*, 684:1–51, 2017.

[121] Jianwei Wang, Fabio Sciarrino, Anthony Laing, and Mark G Thompson. Integrated photonic quantum technologies. *Nature Photonics*, pages 1–12, 2019. 7.1.1

[122] Xianwen Liu, Changzheng Sun, Bing Xiong, Lai Wang, Jian Wang, Yanjun Han, Zhibiao Hao, Hongtao Li, Yi Luo, Jianchang Yan, et al. Aluminum nitride-on-sapphire platform for integrated high-q microresonators. *Optics express*, 25(2):587–594, 2017. 8.1.1

[123] A Gorin, A Jaouad, E Grondin, V Aimez, and P Charette. Fabrication of silicon nitride waveguides for visible-light using pecvd: a study of the effect of plasma frequency on optical properties. *Optics Express*, 16(18):13509–13516, 2008. 8.1.1

[124] Luis Hoffman, Ananth Subramanian, Philippe Helin, Bert Du Bois, Roel Baets, Pol Van Dorpe, Georges Gielen, Robert Puers, and Dries Braeken. Low loss cmos-compatible pecvd silicon nitride waveguides and grating couplers for blue light optogenetic applications. *IEEE Photonics Journal*, 8(5):1–11, 2016. 8.1.1

[125] Dong Yoon Oh, Ki Youl Yang, Connor Fredrick, Gabriel Ycas, Scott A Diddams, and Kerry J Vahala. Coherent ultra-violet to near-infrared generation in silica ridge waveguides. *Nature communications*, 8:13922, 2017. 8.1.1

[126] Hansuek Lee, Tong Chen, Jiang Li, Oskar Painter, and Kerry J Vahala. Ultra-low-loss optical delay line on a silicon chip. *Nature communications*, 3:867, 2012. 8.1.1

[127] Martijn JR Heck, Jared F Bauters, Michael L Davenport, Daryl T Spencer, and John E Bowers. Ultra-low loss waveguide platform and its integration with silicon photonics. *Laser & Photonics Reviews*, 8(5):667–686, 2014. 8.1.1

[128] Gorazd Poberaj, Riccardo Degl'Innocenti, Carolina Medrano, and Peter Günter. Uv integrated optics devices based on beta-barium borate. *Optical Materials*, 31(7):1049–1053, 2009. 8.1.1

[129] J Schroeder, R Mohr, CJ Montrose, and PB Macedo. Light scattering in a number of optical grade glasses. *Journal of Non-Crystalline Solids*, 13(2):313–320, 1974. 8.1.1

[130] B Aspar, H Moriceau, E Jalaguier, C Lagahe, A Soubie, B Biasse, AM Papon, A Claverie, J Grisolia, G Benassayag, et al. The generic nature of the smart-cut® process for thin film transfer. *Journal of Electronic Materials*, 30(7):834–840, 2001. 8.1.1

[131] Hideto Miyake, Chia-Hung Lin, Kenta Tokoro, and Kazumasa Hiramatsu. Preparation of high-quality aln on sapphire by high-temperature face-to-face annealing. *Journal of Crystal Growth*, 456:155–159, 2016. 8.1.1

[132] B Karunagaran, SJ Chung, S Velumani, and E-K Suh. Effect of rapid thermal annealing on the properties of pecvd sinx thin films. *Materials Chemistry and Physics*, 106(1): 130–133, 2007. 8.1.1

[133] Martin Feneberg, Robert AR Leute, Benjamin Neuschl, Klaus Thonke, and Matthias Bickermann. High-excitation and high-resolution photoluminescence spectra of bulk aln. *Physical Review B*, 82(7):075208, 2010. 8.1.1

[134] Roger H French. Electronic band structure of al2o3, with comparison to alon and ain. *Journal of the American Ceramic Society*, 73(3):477–489, 1990. 8.1.1

[135] Aleksej Majkić, Uroš Puc, Alexander Franke, Ronny Kirste, Ramón Collazo, Zlatko Sitar, and Marko Zgonik. Optical properties of aluminum nitride single crystals in the thz region. *Optical Materials Express*, 5(10):2106–2111, 2015. 8.1.1

[136] Aleksej Majkić, Alexander Franke, Ronny Kirste, Raoul Schlesser, Ramón Collazo, Zlatko Sitar, and Marko Zgonik. Optical nonlinear and electro-optical coefficients in bulk aluminium nitride single crystals. *physica status solidi (b)*, 254(9):1700077, 2017. 8.1.1

[137] Aleem M Siddiqui, Daniel Dominguez, Christopher P Michael, Ryan Sims, Paul Stanfield, Lisa P Hackett, Andrew J Leenheer, and Matt Eichenfield. Optimization of si-photonics compatible aln waveguides for integrated nonlinear optics applications. In *CLEO: Applications and Technology*, pages JTu2A–96. Optical Society of America, 2019. 8.1.2

[138] Chi Xiong, Wolfram HP Pernice, and Hong X Tang. Low-loss, silicon integrated, aluminum nitride photonic circuits and their use for electro-optic signal processing. *Nano letters*, 12(7):3562–3568, 2012. 8.1.2

[139] Yiwen Chu, Prashanta Kharel, William H Renninger, Luke D Burkhart, Luigi Frunzio, Peter T Rakich, and Robert J Schoelkopf. Quantum acoustics with superconducting qubits. *Science*, 358(6360):199–202, 2017. 8.1.2

[140] Xu Han, Wei Fu, Changchun Zhong, Chang-Ling Zou, Yuntao Xu, Ayed Al Sayem, Mingrui Xu, Sihao Wang, Risheng Cheng, Liang Jiang, et al. 10-ghz superconducting cavity piezo-optomechanics for microwave-optical photon conversion. *arXiv preprint arXiv:2001.09483*, 2020. 8.1.2